UNIVERSITY OF CALIFORNIA,
IRVINE

Investigating the Structure and Function of Ion Conducting Voltage Sensing Domains

DISSERTATION

submitted in partial satisfaction of the requirements
for the degree of

DOCTOR OF PHILOSOPHY

in Chemistry

by

Mona Lim Wood

Dissertation Committee:
Professor Douglas J. Tobias, Chair
Professor Ioan Andricioaei
Professor Francesco Tombola

2016

DEDICATION

To my parents, Jim and Laura Wood

TABLE OF CONTENTS

LIST OF FIGURES

LIST OF TABLES

ACKNOWLEDGMENTS

Over the course of eight years and in the pursuit of two advanced degrees, I have accumulated countless personal and professional debts to friends, family and advisors. I attempt to describe them in detail here.

My scientific mentor and committee chair, Professor Douglas Tobias, has provided an exciting and challenging academic environment in which to learn and grow. Group meetings over the years exposed me to a diverse and exciting breadth of research and computational techniques, while inciting both fear and admiration for Dr. Tobias's knowledge and expectations. I am grateful to him for the freedom I have been given during graduate school to pursue a variety of projects, sampling from scientific methods covering a wide range of both time and spatial scales. Whether I was studying proton transport or cell migration, I had support and enthusiasm from his corner, and I know that there are few places in the world where I could have had the same learning experience. It has been a true privilege to be a part of his lab and to learn from former group members including Dr. Eric Schow, Dr. Matthias Heyden and Dr. Karen Callahan.

I thank Dr. Tobias for giving me access to our roster of collaborators, which over the past eight years has been constantly growing and always exciting. I have had the opportunity to impose my curiosity on several research groups including Dr. Alex MacKerell's group at the University of Maryland and Dr. Michael Cahalan's group at UC Irvine. I am grateful to Dr. Kenno Vanommeslaeghe in Dr. MacKerell's group for teaching me the slow and painful art of force field parameterization. I thank Dr. I-Feng Will Kuo for hosting me during the summer I spent at Lawrence Livermore National Lab as a Computational Chemistry and Materials Science Fellow. Through our collaboration

with Dr. Francesco Tombola, I learned more than I thought possible about voltage gated ion channels and re-ignited my anxiety of Western blots, which I acknowledge, originated in the Center for Gene Therapy at the University of Michigan in 2005. I thank both Dr. Tombola and Dr. Medha Pathak in the Tombola lab for teaching me the ways of the bench and constantly producing invaluable insight into simulations. I thank Professor Ioan Andricioaei for serving on my committee and members of the 'A' lab for providing friendship and support.

From the first article on voltage-sensing domains I read as an undergraduate student at the University of Michigan to the countless rounds of grant and manuscript revisions during graduate school, Dr. J. Alfredo Freites has been a constant source of scientific inspiration. His fund of knowledge, commitment to detail and straightforward honest scientific opinion are of unparalleled quality and highest among the many teachers and advisors I have met during my studies. The endless hours of scripting, editing and discussion that I spent with Dr. Freites have been pivotal to any of the success I may claim during my years in the Tobias group. I cannot overstate his contributions to my growth as a scientist and a scholar. The work presented within this thesis has benefited greatly from the contributions of other ion channel devotees as well, including Dr. Iris Kim, Dr. Anna Amcheslavsky, Andrew Geragotelis, Hendrik Goeddeke and Eric Wong.

My funding from the National Institutes of Health has come in two forms. During the first portion of my training, the training grant from the UCI Medical Scientist Training Program supported me (NIH Grant Number T32GM008620). During the second portion, I was awarded an F30 National Ruth Kirschstein Service Award from the National

Cancer Institute of the National Institutes of Health (F30CA171717). The successfully funded F30 would not have been possible without mentorship from Dr. Parima Daroui, Dr. Phang-Lang Chen and Dr. Heike Wulff. I also thank the ARCS foundation for their generous award and for providing a community of inspiring women.

Beyond the financial support for medical and graduate school, the UC Irvine Medical Scientific Training Program has provided excellent mentorship and exceptional friendships. Dr. Alan Goldin, UCI MSTP program director, has been an everlasting champion of the program. His guidance has been invaluable through the decade-long challenging path to becoming a physician scientist. The friends I have gained through the MSTP have been my life support through the hardest times of graduate school and clinical training. Dr. Sharine Wittkopp showed me how to be a true friend. During my times of personal and professional turmoil, she gave me the best pieces of advice, which became useful in countless individual encounters after the storm and have guided me to be a better friend. Often throughout this journey, I have wondered whether Marcella Evans was not my twin separated at birth. She and I have an unbroken bond of experiences and empathy, and I am inspired by the kindness and warmth she shows to everybody around her. I thank Dr. William Winter for much encouragement and entertainment and Dr. Haik Mkhikian for teaching me when it's useful to raise my energy and lower my expectations. Dr. Courtney Reynolds is an exemplary model for how to be strong in the face of adversity, and I count myself lucky to be one of her friends. I am grateful to Dr. Greg Starek, who provided a listening ear, sage advice and much needed laughter, despite (or because of) all the antics we encountered during our years of shared office space. He continues to be a wonderful friend of quite remarkable height.

Graduate school combined with medical school has been more challenging, more rewarding and more exhausting than I could have ever imagined. My views on life, happiness and science have changed drastically because of the experiences I have had and the people I have met. Throughout this journey, my parents, Jim and Laura Wood, have been the one unchanged variable. They are and always will be the very best people I know. Their unconditional love, support and encouragement have sustained me through many tumultuous moments and lifted me towards the brightest skies.

CURRICULUM VITAE

Mona L. Wood
M.D. / Ph.D. Student
School of Medicine / School of Physical Sciences
University of California, Irvine
8613 Palo Verde Road
Irvine, CA 92617

Education

University of California, Irvine **2008 - 2016**

- Medical Scientist Training Program (M.D. /Ph.D. dual degree program)
- M.D. Candidate, School of Medicine
    - Scored in the 91st percentile (252/99) on United States Medical Licensing Exam Step 1
- Ph.D. Candidate, School of Physical Sciences, Department of Chemistry (GPA 4.00/4.00)
    - Research topic: Investigating the structure and function of the Hv1 proton channel
    - Advisor: Douglas J. Tobias, Ph.D.

University of Michigan, Ann Arbor **2004 – 2008**

- B.S. Chemistry with High Distinction (top 10% of graduating class. GPA 3.83/4.00)
- Concentrations:
    - French Language and Literature
    - Chemistry with Highest Honors
        - Thesis: Towards Single Molecule Investigations of pre-mRNA Splicing
        - Advisor: Nils Walter, Ph.D.
    - Biochemistry with Honors
        - Thesis: HIV-1 Tat Protein Downregulates Purine Nucleoside Phosphorylase Transcription
        - Advisor: Blake Roessler, M.D.

Work Experience

- Graduate Student, University of California, Irvine, Chemistry Department, 2008-Present
    - Project: Investigating the structure and function of the Hv1 human voltage gated proton channel using molecular dynamics simulations.
    - Advisor: Douglas J. Tobias, Ph.D.
    - Visiting researcher in the lab of Professor Alex MacKerrell, Grollman-Glick Professor of Pharmaceutical Sciences at the University of Maryland, October 2011
        - Developed chemical parameters to computationally model novel small molecule drug interactions with proteins.
- Clinical Research Literature Consultant, Biomerix Corporation, 2008

    - Project: Development of Biomerix NeuroString for ventral and incisional hernial repair
    - Duties: Collect and summarize current clinical research literature pertaining to ventral and incisional repair methods and outcomes to minimize development cycles for the NeuroString product.
- Undergraduate Researcher, University of Michigan, Ann Arbor, Chemistry Department, 2007-2008
    - Project: Using single molecule fluorescence resonance energy transfer to study pre-mRNA dynamics and splicing
    - Advisor: Nils Walter, Ph.D.
- Amgen Research Scholar, University of California, San Francisco, Biophysics Department, 2007
    - Projects: Dynamics of pre-mRNA splicing (in collaboration with UM Walter Lab) and the role of SR-like protein NPL3 in splicing regulation
    - Advisors: Christine Guthrie, Ph.D. and John Abelson, Ph.D.
- Undergraduate Researcher, University of Michigan, Ann Arbor, Center for Gene Therapy, 2005-2007
    - Project: Examining the role of HIV-1 Tat protein in regulating purine nucleoside phosphorylase transcription
    - Advisor: Blake Roessler, M.D.
- Undergraduate Researcher, University of Michigan, Ann Arbor, Radiation Oncology Dept, 2004-2005
    - Project: Radiosensitizing effects of gemcitabine on prostate cancer
    - Advisor: Michael Ray, M.D, Ph.D.

Grants and Fellowships

- NIH National Cancer Institute F30 NRSA Fellow, 2013-2016
    - Awarded to MD/PhD candidates to offset costs of tuition and stipend. (Award total $164,986 NIH Grant Number 1F30CA171717-01A1)
- NIH TL-1 Pre-doctoral Scholar from Institute for Clinical and Translational Sciences, 2013 (*declined*)
    - An NIH funded fellowship awarded annually to a UC Irvine graduate student pursuing either an M.D. or Ph.D. (Award total $25,972. National Center for Advancing Translational Sciences, National Institutes of Health, Grant UL1 TR000153. *Declined for NIH NCI F30*)
- Lawrence Livermore National Lab Computational Chemistry and Materials Science Summer Fellowship, 2012
    - Paid 10 week fellowship to work with leading LLNL researcher on development and application of quantum computing software to model proton transport in biological systems.
    - 10 to 15 fellowships offered from an open pool of applicants.
- UCI Medical Scientist Training Grant, 2008-2016
    - Full tuition, fees and stipend provided for all years of medical and graduate school (NIH Grant Number 2T32GM008620-11)
- University of California, San Francisco Summer Undergraduate Research Fellowship, 2007
    - Paid 8 week summer internship to participate in research at UCSF
- Amgen Scholars Program for Undergraduates, 2007

    - Provided partial funding for UCSF summer fellowship and continued mentoring support.
- U of M Undergraduate Research Opportunity Program, 2004-2005
    - Accepted to program as high school senior, received academic credit for performing scientific research in the radiation oncology lab of Dr. Michael Ray, M.D., Ph.D.

Academic and Professional Honors

- Molecular Pathology Scholarship from the Association for Molecular Pathology, 2015
    - Stipend to offset registration costs for the 24th Annual Symposium on Molecular Pathology
- National Achievement Reward for College Scientists (ARCS®), 2013
    - $20,000 awarded to two graduate students in the School of Physical Sciences.
    - Eligible graduate students nominated from Mathematics, Chemistry, Physics or Earth Systems Science Departments.
- UCI Medical Scientist Training Program Representative to National MD/PhD Conference, 2011
    - One student from UCI MSTP program (40 students) selected annually to present his/her graduate research.
- Phi Beta Kappa, inducted March 2008
- Chemistry Thesis-Highest Honors, 2008
    - Awarded to students demonstrating high academic achievement and capacity for independent research in a departmental Honors concentration program.
- Merck Index Award to Outstanding Seniors, UM Chemistry, 2008
    - Awarded annually to four senior chemistry majors for outstanding achievements.
- ACS Analytical Chemistry/Alumni Award, American Chemical Society, 2008
    - Awarded annually to two chemistry students with highest performance in Instrumental Analysis course.
- U of M Romance Languages and Literatures Student Achievement Award in French, 2008
    - Awarded annually to several (4-5) graduating seniors who majored in French for outstanding academic achievement in French Language and Literatures coursework.
- Biochemistry Thesis-Honors, 2007
    - Awarded to students demonstrating high academic achievement and capacity for independent research in a departmental Honors concentration program.
- Angell Scholar (for 2 or more consecutive terms of 4.0/4.0 GPA), U of M, 2006-2007
- Sophomore Honors Award, University of Michigan, 2006
    - For completing on average of two Honors courses per term with a minimum GPA 3.7 and no grade below a "C."
- University Honors (for a 3.5 GPA or higher during a term), University of Michigan, 2004-2008
- Michigan Merit Award, 2004
- National Merit Scholarship, 2004
- National Honor Society, Inducted 2004
- National Junior Honor Society, Inducted 2003

Extracurricular Projects and Experiences

- Co-founder of Advanced Degree Consulting Club, UC Irvine, 2015
    - Prepare and practice solving business cases using structured approaches with non-MBA graduate students and post-doctoral associates
- Co-chair of UCI Medical Scientist Training Program Clinical Return Committee, 2014-2015
    - Coordinate and implement novel curriculum of clinical experiences to facilitate the transition from graduate school to clinical years of medical school.
- McKinsey & Company MD Contact Participant, 2013
    - Selected to attend workshop for advanced doctoral degree candidates to gain in-depth perspective of management consulting
    - Worked in a mock case team to analyze hospital operations, conduct interviews to gather qualitative data, and develop and present recommendations to high level management.
- Co-chair of UCI Medical Scientist Distinguished Scientist Lecture Series, 2012-2014
    - Organize, invite and host monthly seminars given by internationally renowned scientists, including members of the National Academy of Sciences and Nobel Prize winners.
- Kaplan Test Prep MCAT teacher, 2011-2012
- Tutor for UCI Medical School, 2009-present
    - Subjects: Clinical foundations, Pharmacology, Pathology, Neuroscience, Anatomy
- Private tutor for various students, 2002-present
    - Subjects: AP Biology, AP Chemistry, Pre-calculus, French
- Co-founded Medical Scientist Training Program (MSTP) Translational Medicine Journal Club, 2009
- Volunteer at UCI School of Medicine Outreach Clinic, 2009-present
- MSTP New Faculty Lectures Series Committee, 2009-2010
- MSTP Annual Retreat Committee, 2009-2010
    - Planned weekend retreat for over 40 students and their guests, invited internationally renowned speakers and organized student poster sessions, student talks and career development/mentoring sessions.
- Unite for Sight International Volunteer, May 2008
    - Provided eye exams and cataract screening for underserved populations in Chennai, India
- U of M Science Learning Center Study Group Leader for Introductory Electromagnetism, 2007-08
- U of M Hospital Volunteer in Emergency Room and Intensive Care Unit, 2004-07
- Research assistant, University of Michigan Center for Gene Therapy, 2005-07

Publications

Wood, M.L., Lee, T.K., Armstrong, W.B., and Wang, B.Y. "Cervical spine synovial chondromatosis: A case report and literature review." *Submitted*

Amcheslavsky, A., **Wood, M.L.,** Yeromin, A., Parker, I. J. Freites, J.A., Tobias D.J., and Cahalan M.D. Molecular Biophysics of Orai Store-Operated Ca2+ Channels. Biophys

J.108(2):237-246. 2015.

Florescu, C., **Wood M.L.**, and Bota, R. From research to practice in child and adolescent mental health. Mental Illness. 5707(2), 272, 2015.

Wood, M.L., Schow, E.V., Freites, J.A., White, S.H., Tombola, F. and Tobias, D.J. Water wires in atomistic models of the Hv1 proton channel. Biochim. Biophys. Acta, 1818(2), 286-93, 2012.

Abelson, J., Blanco, M., Ditzler, M.A., Fuller, F., Aravamudhan, P., **Wood, M.**, Villa, T., Ryan, D.E., Pleiss, J.A., Maeder, C., Guthrie, C. and Walter, N.G. Conformational dynamics of single pre-mRNA molecules in spliceosome assembly. Nat. Struct. Mol. Biol. 4, 504-512. [Highlighted as UM News Release March 21, 2010]

Presentations

Andrew Geragotelis, **Mona Wood**, Hendrik Goeddeke, Liang Hong, Saleh Riahi, Eric K. Wong, J. Alfredo Freites, Francesco Tombola, Douglas J. Tobias. Multi-Microsecond Molecular Dynamics Simulations of the Hv1 Proton Channel. Biophysical Society Annual Meeting, Los Angeles, CA 2016.

Ruth Hsu, **Mona Wood**, Pejman Solaimani, Ankush Sharma, Matthew Butteri. Atypical manifestation of Granulomatosis with Polyangiitis. Clinical Vignette. American College of Physicians Annual Meeting, Anaheim, CA 2014.

Mona Wood, Anna Amcheslavsky, Eric Wong, J. Alfredo Freites, Michael D. Cahalan and Douglas J. Tobias. Atomistic molecular dynamics simulations of drosophila Orai in a hydrated lipid bilayer. Biophysical Society Annual Meeting, San Francisco, CA, 2014.

Mona Wood, J. Alfredo Freites, Stephen H. White, Francesco Tombola and Douglas J. Tobias. Atomistic modeling of ion conduction through voltage sensing domains. Biophysical Society Annual Meeting, San Francisco, CA, 2014.

Mona Wood. Investigating the anti-neoplastic activity of Hv1 channel blockers using insights from MD simulations and experiment. 17th Annual MSTP Retreat, UC Irvine, 2013.

Mona Wood, Greg Starek, J. Alfredo Freites, Stephen H. White, Francesco Tombola and Douglas J. Tobias. Molecular Dynamics Simulations of the Hv1 Proton Channel. Biophysical Society Annual Meeting, Philadelphia, PA, 2013.

Mona Wood. Investigating the anti-neoplastic activity of Hv1 channel blockers. 2nd Annual MSTP Symposium, UC Irvine, 2012.

Mona Wood, Eric Schow, J. Alfredo Freites, Francesco Tombola, I-Feng William Kuo and Douglas J. Tobias. QMMM Studies of Proton Conduction in the Hv1 Proton Channel. Summer Student Research Symposium, Lawrence Livermore National Lab, 2012.
Mona Wood. Structure and Function of the Hv1 Proton Channel. Summer Student Research Seminar Series, Lawrence Livermore National Lab, 2012.

Mona Wood, Eric Schow, J. Alfredo Freites, Stephen White, Francesco Tombola and Douglas J. Tobias. Voltage-gating in the Hv1 Proton Channel: Clues from Atomistic Molecular Dynamics Simulations. Biophysical Society Annual Meeting, San Diego, CA, 2012.

Mona Wood. Structure and Function of Hv1 Proton Channel. 1st annual MSTP Symposium, UC Irvine, 2011.

Mona Wood, Eric Schow, J. Alfredo Freites, Stephen White, Francesco Tombola and Douglas J. Tobias. Proton Conduction via Water Wire in the Hv1 Proton Channel. National MD/PhD Conference, Keystone, CO, 2011.

Mona Wood, Eric Schow, J. Alfredo Freites, Stephen White, Francesco Tombola and Douglas J. Tobias. Proton Conduction via Water Wire in the Hv1 Proton Channel. Biophysical Society Annual Meeting, Baltimore, MD, 2011.

Mona Wood, Eric Schow and Douglas J. Tobias. Energetics of Ion Permeation Through the Hv1 Proton Channel. 13th Annual MSTP Retreat, UC Irvine, 2009.

Mona Wood, Mario Blanco, Mark Ditzler, John Abelson and Nils Walter. Single Molecule Analysis of Pre-mRNA Splicing. 12th Annual MSTP Retreat, UC Irvine, 2008.

Mario R. Blanco, Mark Ditzler, Frank Fuller, **Mona Wood**, John Abelson, and Nils Walter. Single Molecule Observations of pre-mRNA Dynamics During Splicing. Rustbelt RNA Meeting, Dayton, OH 2008.

Mario Blanco, Mark Ditzler, Jesse Sianan, **Mona Wood**, John Abelson and Nils Walter. Monitoring pre-mRNA and Spliceosome Dynamics Using Single Molecule Fluorescence Resonance Energy Transfer. Presented at Rustbelt RNA Meeting, Dayton, OH, 2007.

Mona Wood, Tracy Kress, John Abelson and Christine Guthrie, The Role of SR-like Protein NPL3 in Splicing Regulation. Summer Undergraduate Research Symposium, UC San Francisco, 2007.

Mona Wood, Sonja Markwart and Michael Ray. Radio-sensitizing Effects of Gemcitabine on Human Tumor Cells. Undergraduate Research Symposium, University of Michigan, 2005.

Academic Society Memberships

Biophysical Society
American Society for Clinical Pathology

ABSTRACT OF THE DISSERTATION

Investigating the Structure and Function of Ion Conducting Voltage Sensing Domains

By

Mona Lim Wood

Doctor of Philosophy in Chemistry

University of California, Irvine, 2016

Professor Douglas J. Tobias, Chair

Voltage-gated ion channels (VGICs) open and close in response to changes in electric potential across the cell membrane to control the flow of ions into and out of the cell. Typical VGICs contain four subunits, each subunit contains 6 helices (termed S1-S6). Helices S1, S2, S3 and S4 compose a voltage sensing domain, while helices S5 and S6 from each subunit contribute to a single pore domain. The pore domain conducts ions selectively, however mutations in the VSD can lead to aberrant ionic currents through the voltage-sensor. These currents, termed omega currents, are studied in atomistic detail using molecular dynamics simulations. Additionally, I performed simulations of the Hv1 voltage gated proton channel, which is homologous to the VSD of typical VGICs but lacks the typical pore domain. The structural similarities between Hv1 and typical VGIC VSDs were exploited to construct a homology model of the channel, which was used as a starting point for probing the mechanism of proton conduction prior to the discovery of a crystal structure for the channel. I found

spontaneous formation of hydrogen bonded water wires in the homology model of Hv1 which do not form in simulations of the non-conducting VSDs, supporting a Grotthuss style hopping mechanism for proton conduction through Hv1. The crystal structure for a mouse voltage-gated proton channel chimera was solved in 2014. The improved template provided inspiration for a new model of the human proton channel, which proved stable on the microsecond timescale. A depolarizing, or opening, applied transmembrane voltage revealed motions of the S4 helix consistent with experimental measurements of gating charge transfer during voltage-activation. The final configuration from these microsecond simulations is presented as a likely open-state model of the channel.

Chapter 1

Introduction

The basic building block of life is the single cell, which is enclosed by a semi-permeable membrane that serves as a protective barrier between the exterior environment and the inside of the cell. Sitting in the membrane are vital proteins that function as receptors for cellular communication and gatekeepers for the transport of substances into and out of the cell. A specific class of these membrane-bound proteins is the ion channel, which regulates the movement of ions and other small molecules across the cell membrane. Ion channels play a key role in many physiological processes, such as nerve impulse propagation, vision, bacterial resistance and insulin regulation, yet many questions still remain about channel structure and the underlying molecular mechanisms of ion conduction, signaling and gating(1).

Over 13% of all FDA approved drugs target ion channel function directly and are used to treat a wide array of conditions, including cancer, epilepsy, high blood pressure and pain(2-4). Because of their gatekeeper status and widespread importance in human

physiology, ion channels remain prime drug targets for many ailments beyond the current applications. The knowledge gained about the detailed function of ion channels contributes to our understanding of basic physiological processes and allows us to imagine new treatments for human disease. In this dissertation, I present results from computational and experimental studies, which address questions related to the structure and function of ion channels. In terms of methodology, I focused primarily on using molecular dynamics (MD) simulations to understand the structure and function of two particular ion channel proteins (i.e. Hv1; the human voltage-gated proton channel and Kv-VSD; the voltage-sensing domain of Kv channels). MD simulations solve Newton's equations of motion for a molecular system, such as Hv1 in a membrane environment, to generate trajectories that describe how the atoms in the system move over time. These simulations allow us to view motions of key structural features of the protein that are too small and too fast to be captured by experiment alone. I also employed an assortment of experimental approaches to explore the effects of pharmacologic ion channel inhibitors on metastatic activities of cell lines expressing Hv1, described in Chapter 5.

Both Hv1 and Kv-VSD are members of the voltage-gated ion channel (VGIC) superfamily. VGICs sense fluctuations in the transmembrane electric field and undergo conformational changes to allow ions to move across the cell membrane. Typical VGICs are made up of four subunits, with each subunit composed of six transmembrane segments, termed S1-S6. The S1 to S4 segments from each subunit form a separate voltage-sensing domain (VSD), which confers sensitivity to changes in the electric field. The S5 and S6 segments from each subunit contribute to one fourth of a single pore domain. The pore

domain undergoes conformational changes mediated by the VSD and opens and closes to conduct ions across the membrane.

The human voltage-gated proton channel, Hv1, conducts protons across the membrane and is homologous to the VSD of typical VGICs but uniquely lacks a pore domain(5). In its physiological state, Hv1 assembles as a dimer of VSDs through a coiled-coil interaction in its C-terminus. Truncations in the C-terminus yield functional monomeric channels that conduct protons, with each monomeric VSD serving as a voltage sensor and pore domain(6, 7). Though aberrant ion conduction through VSDs had been reported in mutant potassium and sodium VGICs, wild type Hv1 channels display outward proton currents in both a variety of human tissues(8-12). These currents serve in a variety of important physiologic roles, including pathogen elimination in neutrophils and alkalization of spermatozoa during fertilization. Prior to the publication of a high resolution structure for Hv1, little was known about mechanism or pathway for proton conduction and the architecture of the VSD was inferred from the VSD structures available at the time.

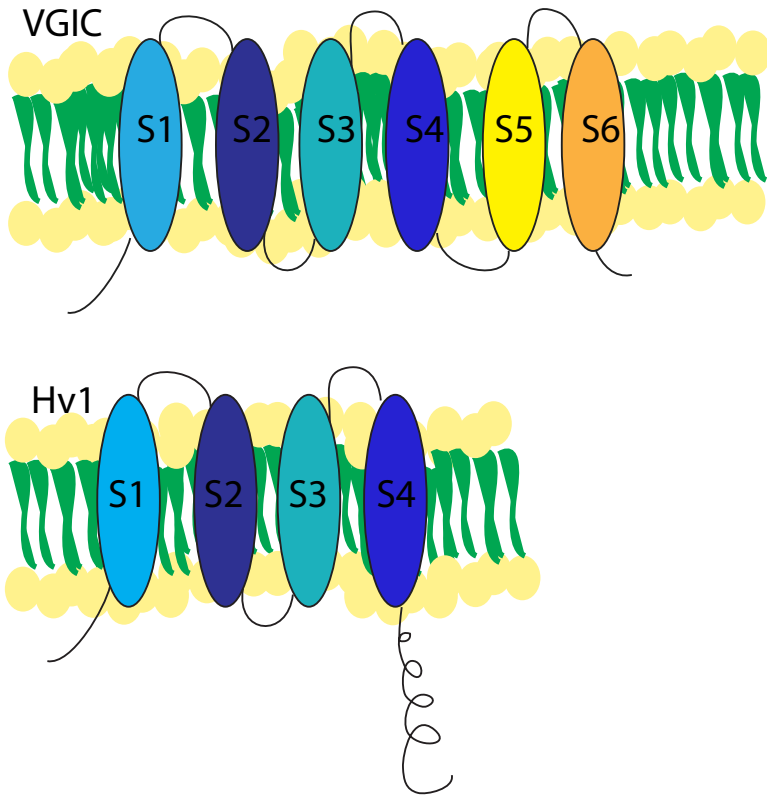

Figure 1.1 Schematic of ion channel subunit composition. Typical voltage-gated ion channels (VGIC) are tetramers, with each monomer composed of 6 transmembrane segments (S1 to S6). S1 to S4 compose a voltage-sensing domain while S5 and S6 contribute to one fourth of the pore domain. Hv1 is a voltage-gated proton channel that uniquely lacks a pore domain.

In Chapter 2, I describe the construction of a homology model of the Hv1 channel using the crystal structure of the VSD from the voltage-gated Kv1.2-2.1 paddle chimera channel(13) as a template. Two Hv1 models using alternate alignments between the template and the Hv1 in the S4 segment were constructed and simulated(14). Transmembrane hydrogen bonded water wires formed spontaneously in both models, which supported the notion that proton transport in Hv1 may occur in part through a Grotthuss transport mechanism where protons hop across of a chain of waters (Figure 1.2). Evidence for Grotthuss-type H^+ transfer has been presented for several proton transporting proteins, including gramicidin(15) bacteriorhodopsins(16) and H^+/ATPases.(17, 18). In chapter 2, we

also characterized the hydration patterns and intra-VSD salt-bridge formations, which were unique in each separate model but similar to intra-VSD interactions found in typical VGIC VSDs.

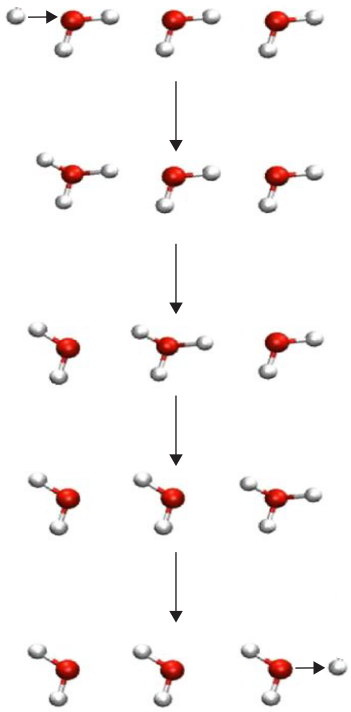

Figure 1.2 Grotthuss hopping mechanism. The excess proton hops between adjacent water molecules in the hydrogen bonded water wire through covalent bond formation and breaking events. Hydrogen and oxygen are represented as white and red Van der Waals spheres, respectively.

The publication of a high resolution structure of mouse voltage gated proton channel in a trimeric assembly in 2014 offered insights into closed-state channel structure while still leaving questions about the open or activated state and dimer interface unanswered(19). In Chapter 3, I describe microsecond timescale simulations of the high resolution trimeric and monomeric structure with and without an applied opening potential. Both the trimer and monomeric structures are stable on the microsecond timescale. In the monomer, an applied

opening potential resulted in salt-bridge exchange between a set of highly conserved basic residues in the S4 segment and acidic residues in S1 to S3, resulting in an overall movement of the S4 segment 8Å outward along the transmembrane direction of the bilayer. The motions of the S4 helix are responsible for gating the opening of the pore domain in typical VGICs, and various models for the mechanistic model of voltage-sensing have been proposed over the years, as discussed in Chapter 3. The simulation results support a sliding-helix style model of voltage-activation and recapitulates experimental measurements of gating charge movement in the channel. The final configuration of Hv1 in an activated state offers the first insights into an open state structure. Additionally, the discovery of a series of chemically permutated open-channel blockers with varying levels of binding affinity allowed us to identify with confidence putative blocker binding sites in the model(20-22). Though experimental observables help validate our model as a likely representative of the physiological open state, we have yet to model proton transport through the channel. Ultimately, we expect the open state configuration of Hv1 to be able to support proton transport, aided in part by hydrogen bonded water wires. A proposed method towards the confirmation of this hypothesis is explored in further detail in Chapter 5.

Specific mutations in the amino acid sequence of the voltage-gated potassium channel (Kv) VSD yield cationic currents through the VSD separate from the pore domain(23). These non-canonical cationic currents are termed omega-currents, which travel through the mutated VSD, termed an omega pore. Omega currents have been reported in mutants of the voltage-gated sodium channels as well, and their activity has been linked to the pathophysiology of several diseases including epilepsy and skeletal muscle periodic pa(24, 25)ralysis. The permeation pathway taken by the ion in the VSD has

been studied both experimentally and computationally(26, 27). The chemical interactions between the ion in the omega current and certain mutable residues in the Kv VSD were classified through mutant analysis experiments as either steric, electrostatic, null or indirect. Molecular dynamics simulations by other groups have provided atomic-level insights into an omega current flowing through a similar but non-identical Kv VSD protein sequence (27, 28). In Chapter 4, I describe multi-microsecond simulations of the same Kv VSD mutant used in experiments, which were produced on Anton, a special purpose supercomputer. In my simulations I observed omega current carried by either potassium or guanidinium ions. I describe the mechanism of permeation as well as the interactions between ions in the omega current and residues lining the VSD in atomistic detail.

The discovery of small molecule Hv1 channel inhibitors coincided with the finding that silencing of Hv1 expression in metastatic breast cancer cell lines decreases metastatic activity and proliferation(29, 30). In Chapter 5, I describe a multi-disciplinary and translational approach to study small molecule channel blockers as potential anti-neoplastic therapeutics. I worked with our collaborators in Professor Francesco Tombola's lab to apply insights from atomistic structural observations towards *in silico* small molecule development and *in vitro* testing of the antineoplastic activities of ion channel blockers targeting Hv1. We found that the Hv1 channel blockers were able to decrease would healing ability in the highly metastatic breast cancer cell lines, suggesting that pharmaceutical blockade of the channel may have promising applications for the development of antineoplastics targeting the channel. The results in this dissertation pave the way for structure-based drug design targeting membrane proteins involved in cancer and other pathologies.

References

1. Hille B (2001) *Ion Channels of Excitable Membranes* (Sinauer Associates, Inc., Sunderland) 3rd Ed pp 1-814.
2. Fiske JL, Fomin VP, Brown ML, Duncan RL, & Sikes RA (2006) Voltage-sensitive ion channels and cancer. *Cancer Metastasis Rev* 25(3):493-500.
3. Ahern CA, Eastwood AL, Dougherty DA, & Horn R (2008) New insights into the therapeutic inhibition of voltage-gated sodium channels. *Channels (Austin)* 2(1):1-3.
4. Li M & Xiong ZG (2011) Ion channels as targets for cancer therapy. *Int J Physiol Pathophysiol Pharmacol* 3(2):156-166.
5. Ramsey IS, Moran MM, Chong JA, & Clapham DE (2006) A voltage-gated proton-selective channel lacking the pore domain. *Nature* 440:1213-1216.
6. Tombola F, Ulbrich MH, & Isacoff EY (2009) Architecture and gating of Hv1 proton channels. *J Physiol* 587(Pt 22):5325-5329.
7. Tombola F, Ulbrich MH, Kohout SC, & E.Y. I (2010) The opening of the two pores of the Hv1 voltage-gated proton channel is tuned by cooperativity. *Nature Struct. Mol. Biol.* 17:44-50.
8. Kim IH*, et al.* (2014) Evidence for functional diversity between the voltage-gated proton channel Hv1 and its closest related protein HVRP1. *PLoS One* 9(8):e105926.

9. Zhao Q*, et al.* (2015) The voltage-gated proton channel Hv1 is expressed in pancreatic islet beta-cells and regulates insulin secretion. *Biochem Biophys Res Commun* 468(4):746-751.
10. Zeng WZ*, et al.* (2015) Activation of acid-sensing ion channels by localized proton transient reveals their role in proton signaling. *Scientific reports* 5:14125.
11. DeCoursey TE (2015) The Voltage-Gated Proton Channel: A Riddle, Wrapped in a Mystery, inside an Enigma. *Biochemistry* 54(21):3250-3268.
12. O'Connor PM, Guha A, Stilphen CA, Sun J, & Jin C (2016) Proton channels and renal hypertensive injury: a key piece of the Dahl salt-sensitive rat puzzle? *American journal of physiology. Regulatory, integrative and comparative physiology* 310(8):R679-690.
13. Long SB, Campbell EB, & MacKinnon R (2005) Crystal structure of a mammalian voltage-dependent Shaker-family K^+ channel. *Science* 309:897-903.
14. Wood ML*, et al.* (Water wires in atomistic models of the Hv1 proton channel. *Biochim Biophys Acta* 1818(2):286-293.
15. Pomes R & Roux B (2002) Molecular mechanism of H+ conduction in the single-file water chain of the gramicidin channel. *Biophys J* 82(5):2304-2316.
16. Freier E, Wolf S, & Gerwert K (Proton transfer via a transient linear water-molecule chain in a membrane protein. *Proc Natl Acad Sci U S A* 108(28):11435-11439.
17. Cukierman S (2003) The transfer of protons in water wires inside proteins. *Front Biosci* 8:s1118-1139.

18. Cukierman S (2006) Et tu, Grotthuss! and other unfinished stories. *Biochim Biophys Acta* 1757(8):876-885.

19. Takeshita K*, et al.* (2014) X-ray crystal structure of voltage-gated proton channel. *Nat Struct Mol Biol* 21(4):352-357.

20. Hong L, Pathak MM, Kim IH, Ta D, & Tombola F (2013) Voltage-sensing domain of voltage-gated proton channel Hv1 shares mechanism of block with pore domains. *Neuron* 77(2):274-287.

21. Hong L, Kim IH, & Tombola F (2014) Molecular determinants of Hv1 proton channel inhibition by guanidine derivatives. *Proc Natl Acad Sci U S A* 111(27):9971-9976.

22. Hong L, Singh V, Wulff H, & Tombola F (2015) Interrogation of the intersubunit interface of the open Hv1 proton channel with a probe of allosteric coupling. *Scientific reports* 5:14077.

23. Tombola F, Pathak MM, Gorostiza P, & Isacoff EY (2007) The twisted ion-permeation pathway of a resting voltage-sensing domain. *Nature* 445:546-549.

24. Sokolov S, Scheuer T, & Catterall WA (2007) Gating pore current in an inherited ion channelopathy. *Nature* 446(7131):76-78.

25. Catterall WA, Dib-Hajj S, Meisler MH, & Pietrobon D (2008) Inherited neuronal ion channelopathies: new windows on complex neurological diseases. *J Neurosci* 28(46):11768-11777.

26. Gamal El-Din TM, Heldstab H, Lehmann C, & Greeff NG (2010) Double gaps along Shaker S4 demonstrate omega currents at three different closed states. *Channels (Austin)* 4(2):93-100.

27. Khalili-Araghi F, Tajkhorshid E, Roux B, & Schulten K (2012) Molecular dynamics investigation of the omega-current in the Kv1.2 voltage sensor domains. *Biophys J* 102(2):258-267.

28. Delemotte L, Treptow W, Klein ML, & Tarek M (2010) Effect of sensor domain mutations on the properties of voltage-gated ion channels: molecular dynamics studies of the potassium channel Kv1.2. *Biophys. J.* 99:L72-L74.

29. Wang Y*, et al.* (2011) Specific expression of the human voltage-gated proton channel Hv1 in highly metastatic breast cancer cells, promotes tumor progression and metastasis. *Biochem Biophys Res Commun* 412(2):353-359.

30. Wang Y, Li SJ, Wu X, Che Y, & Li Q (2012) Clinicopathological and Biological Significance of Human Voltage-gated Proton Channel Hv1 Protein Overexpression in Breast Cancer. *J Biol Chem* 287(17):13877-13888.

Chapter 2

Water wires in atomistic models of the Hv1 proton channel

2.1 Introduction

The Hv1 channel (1, 2) is found in a wide range of tissues and has been shown to serve a variety of important physiological functions. In neutrophils Hv1 activity is required for optimal ROS production by the NADPH oxidase during the oxidative burst (3-5). In B lymphocytes, the activation of the Hv1 channel enhances the BCR-mediated intracellular signaling cascade that leads to B-cell proliferation and differentiation (6). In basophils, Hv1 has been proposed to play an important role in the stimulation of histamine release (7). In mature human spermatozoa, Hv1 acts as a flagellar regulator of intracellular pH, promoting sperm capacitation (8). In the respiratory system, Hv1 is

involved in the pH homeostasis of the airway surface liquid, by contributing to acid extrusion from the airway epithelium (9).

In the plasma membrane, Hv1 is found as a homodimer that is stabilized by intracellular coiled-coil interactions in the C terminus (10). Truncations in the C-terminus results in the formation of functional monomeric channels that have their own permeation pathway and voltage sensor (11, 12). The Hv1 channel is made of four transmembrane helices (S1-S4), which are homologous to the voltage-sensing domain (VSD) of voltage-gated potassium (Kv) channels. Voltage sensitivity in the VSD is conferred by a series of highly conserved positions for charged residues. In particular, the S4 segment contains several triplet repeats composed of a basic side chain (mostly arginine) followed by two hydrophobic residues. In the case of *Shaker*, it has been shown that the first four arginines in S4 (termed R1 through R4) contribute most of the gaiting charge during activation (13-15). Hv1 exhibits three of these repeats, and mutations of the S4 arginines have been shown to alter its activation kinetics (1, 2). In addition, voltage-clamp fluorometry and state-dependent accessibility measurements in Hv1 channels report motion of S4 during activation (16, 17), as previously observed in Kv channels (18-21). A helical hairpin made of portions of the S3 and S4 helices, called the paddle motif, can be transplanted from a variety of proteins, including Hv1, into a Kv channel without loss of function (22). These findings establish a structural connection between Hv1 and nonconducting VSDs. However, the molecular mechanisms behind the specific functional features of Hv1, namely, proton permeation and selectivity, and regulation by pH, remain unknown. In addition, functional predictions at the molecular level are hindered by the lack of a high-resolution structure.

The ability to conduct ions through the VSD is not a unique feature of the Hv1 channel, since mutated VSDs of Kv channels (23-27) and voltage-gated sodium (Nav) channels (28-30) can also support ion permeation. The current view of cation permeation through these VSDs is that specific mutations of side chains lining the VSD interior remove an occlusion between the hydrated intracellular and extracellular crevices of the VSD structure (31), allowing ion flux. Most conducting Kv and Nav VSD variants involve the mutation of at least one of the basic side chains in S4 (23-26, 28), but proton conduction has also been reported in mutants of residues in S1 and S2 (27).

Only one Kv VSD mutant, *Shaker* R371H, has been reported to generate proton currents under a depolarizing potential, as in Hv1 (23). R371 in *Shaker* corresponds to the fourth S4 arginine, which suggests a possible alignment of R1 through R3 in Hv1 to R1 through R3 in *Shaker*, leaving N214 in Hv1 at the R4 position in Kv channels. The N214R mutation has been reported to abolish the outward proton current in the human Hv1 (11, 32), while the similar mutation in the mouse channel (N210R) yields very low density currents and slow activation kinetics (33). In addition, Hv1 proton currents have been shown to be reversibly blocked by intracellular guanidinium ions, while trimethylaminoethyl-methanethiosulfonate (MTSET) has been shown to block the current carried by the N214C mutant of the human Hv1 (11) or by the equivalent mutant of the *Ciona intestinalis* ortholog (16). These results suggest that permeation through Hv1 may occur in a similar manner as in coducting VSD mutants of Kv and Nav channels.

An alternative view of the structural relationship between Kv VSDs and Hv1 could be derived from considerations of sequence conservation. Although most Kv channel

families exhibit the same R1 through R4 charge distribution in the sequence of the S4 segment as in *Shaker*, conservation of the R1 position for a basic side chain is somewhat lower than for R2-R4 (34). Therefore, as first reported by Sasaki et al (1), multiple sequence alignment of Hv channels to the VSDs in the superfamily of voltage-gated ion channels could lead to an alignment of the three S4 arginines in Hv1 to positions R2-R4 in Kv channels.

Here, we use atomistic molecular dynamics (MD) simulations of two different homology models of Hv1 in a lipid bilayer in excess water to probe the structural and dynamical features of a putative proton permeation pathway. Both homology models were generated using the Kv1.2 paddle-chimera structure (35) as a template, but they were aligned differently in the region of the S4 segment. The simulations reveal a water wire connecting the intracellular and extracellular sides, suggesting proton conduction via a Grotthuss hopping mechanism. The kinetic stability of the water wire is dependent upon the interactions with a set of highly conserved side chains lining the permeation pathway. We find that persistent interactions with two of the S4 arginines, as part of a larger cluster of polar residues, as well as the formation of a well defined hydrophobic gap in the center of the protein are key to the formation of a robust water wire. In addition, a measurement of water transport kinetics indicates that the present model of Hv1 cannot be characterized as a water channel.

2.2 Methods

2.2.2 Molecular Dynamics Simulations

Using the crystal structure the Kv1.2 paddle-chimera VSD (35) as a template, we constructed two different atomistic models for Hv1. In the first model, R1-Hv1, the three arginines in the S4 segment of Hv1 were aligned to positions R1 through R3 in the S4 segment of the paddle chimera (see Fig. 2. 1). In the R2-Hv1 model, the Hv1 arginines were shifted three residues over to align with positions R2, R3 and R4 of the paddle chimera. These two sequence alignments (see Fig. 2. 1A) were then used as input for MODELLER 9.8 (36) to build the initial three-dimensional configurations (shown in Figs. 1B and 1C).

Each of the resulting configurations were embedded in a POPC bilayer in excess water. Each system included one Hv1 monomer (residues 91 to 223), 282 lipids, 10,652 water molecules, and sufficient Cl^- counterions to make the system charge neutral, for a total of 72,055 atoms. The initial bilayer configuration for each system was such that the water wires that are reported in this work were not present. We also performed a simulation of an N214R Hv1 mutant based on the R1-Hv1 configuration in an otherwise identical system. The initial configuration for the N214R simulation was taken from a snapshot of R1-Hv1 after 130 ns of simulation. Finally, we performed a simulation of the Kv1.2 paddle chimera VSD (residues 145 to 320) under similar conditions (282 lipids, 13,993 water molecules, 82,610 total atoms). The initial configuration of that simulation was taken from an equilibrated snapshot of the full Kv1.2 paddle chimera tetramer, such that the S4 arginines were already hydrated. To initialize each of the simulations, we first ran 2000 steps of conjugate-gradient energy minimization followed by 100 ps of simulation with the protein backbone atoms fixed at constant temperature (300 K) and volume. We then switched to constant pressure (1 atm) and gradually released the

backbone in 100-ps steps, using 50, 20, 10, 5, 2, and 1 kcal mol^{-1} $Å^{-2}$ restraints. The total unrestrained simulation lengths were roughly 200 ns for the R1- and R2-Hv1 simulations, 135 ns for the N214R R1-Hv1 simulation, and 275 ns for the Kv paddle chimera VSD simulation.

All simulations were performed with the NAMD 2.7b2 software package (37). The CHARMM22 and CHARMM32 force fields (38, 39) were used for protein and lipids, respectively, and the TIP3P model was used for water (40). The smooth particle mesh Ewald method (41, 42) was used to calculate electrostatic interactions. Short-range real-space interactions were cut off at 11 Å, employing a switching function. A reversible multiple time-step algorithm (43) was employed to integrate the equations of motion with a time step of 4 fs for electrostatic forces, 2 fs for short-range non-bonded forces, and 1 fs for bonded forces. All bond lengths involving hydrogen atoms were held fixed using the SHAKE (44) and SETTLE (45) algorithms. A Langevin dynamics scheme was used for temperature control and a Nosé-Hoover-Langevin piston was used for pressure control (46, 47). Molecular graphics and trajectory analyses were performed using VMD 1.8.7 (48) over the last 120 ns of each trajectory.

2.2.2 Water dynamics analyses.

We define a transmembrane water wire as any configuration of H bonded waters in the channel connecting the extracellular side to the intracellular side. A H bond was defined using conventional geometric criteria (donor-acceptor distance < 3.5 Å and donor-hydrogen-acceptor angle > 140 Å). Water wire formation along each simulation

trajectory was modeled as a binary process wire/no-wire, irrespective of the actual number of H bonded configurations or the identity of the water molecules. The reported correlation times correspond to single-exponential fits to the binary process autocorrelation function and to the continuous time correlation function computed only over the configurations showing a wire. The latter is defined as

$$C(t) = \frac{\langle H(t)H(0)\rangle}{\langle H^2\rangle}$$

where *H(t) = 1* if a water wire has been present continuously from *t = 0* to time *t*, and *H(t) = 0* otherwise.

The residence time for water molecules in the solvation shell of a given amino acid residue lining the pore of the R1-Hv1 channel were calculated as the time corresponding to the *1/e* value of the water survival function in the solvation shell defined as

$$S(t) = \frac{\langle h(t)h(0)\rangle}{\langle h^2\rangle}$$

where *h(t) = 1* if a given water molecule present in the residue coordination shell at t = 0 is also present at time *t*, and the average is over all waters.

The osmotic permeability coefficient for waters in the R1-Hv1 pathway was calculated using the method of Zhu et al. (49). A collective coordinate for waters in the interior of the channel was calculated as the integral of

$$dn(t) = \frac{1}{L(t)}\sum_i z_i(t) - z_i(t+\delta t)$$

where the z_i are the positions of the i^{th} water along the transmembrane direction over two consecutive configurations and *L(t)* is the instantaneous length of the stretch between D174 on the intracellular side and R208 on the extracellular side. The osmotic permeability coefficient (p_f) is given by

$$p_f = v_w D_n$$

where v_w is the molecular volume of water and D_n is given by

$$\left\langle n^2(t) \right\rangle = 2D_n t$$

2.3. Results

We performed two 120 ns all-atom MD simulations of two different structural models of the transmembrane region of Hv1 from *Homo sapiens* embedded in a POPC lipid bilayer in excess water. Both models where generated using the crystal structure of the Kv1.2 paddle-chimera VSD as a template (35). In the first model (hereinafter termed R1-Hv1), the three arginines in the S4 segment of Hv1 were aligned to positions of the first three arginines (R1, R2, R3) in the S4 segment of the Kv1.2 VSD. In the second model (hereinafter termed R2-Hv1), the Hv1 S4 arginines were shifted three residues over to align with R2, R3 and R4 of the Kv1.2 VSD. The remaining three transmembrane segments (S1 through S3) were aligned by matching all the highly-conserved positions that have been implicated in Kv VSD function to the Hv1 sequence (see Fig. 2.1).

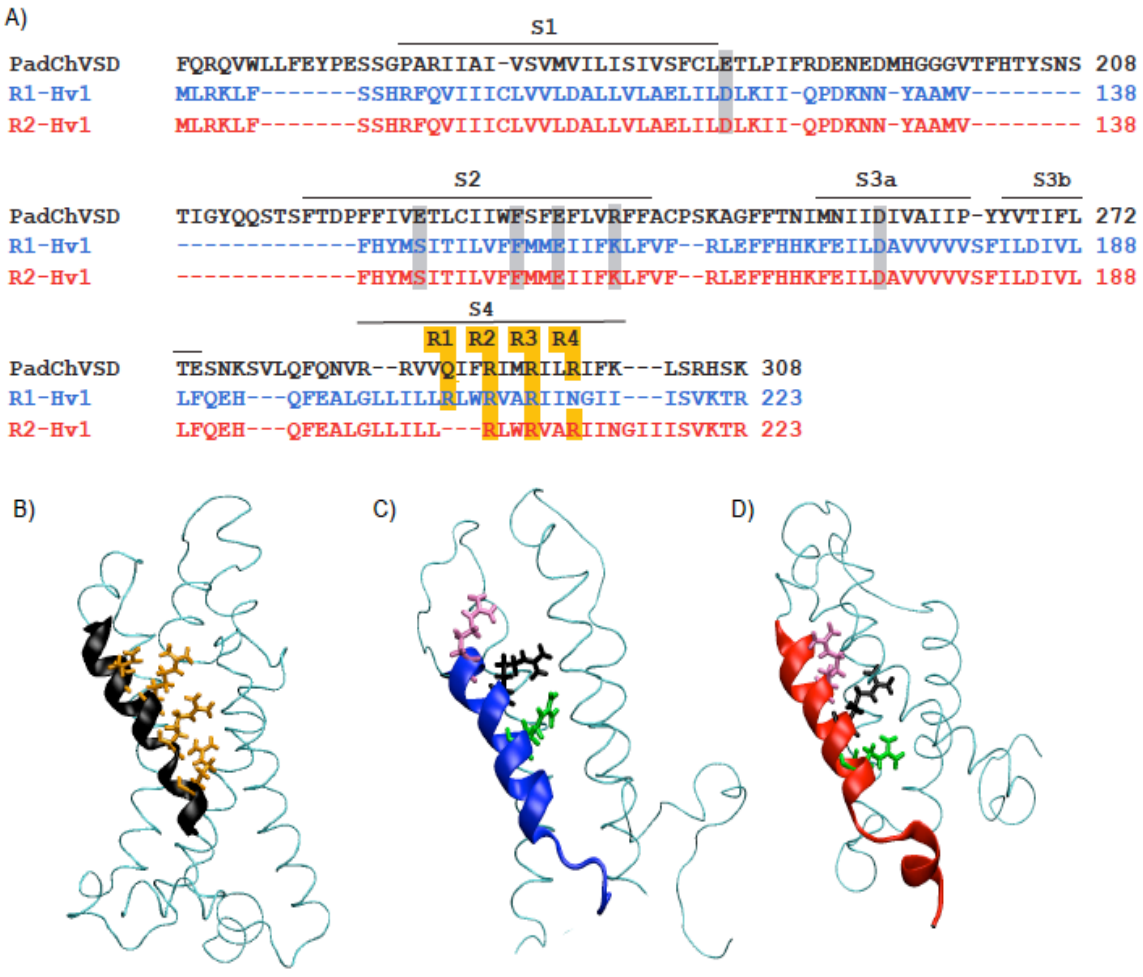

Figure 2.1. Hv1 homology modeling. A) Two sequence alignments of the human Hv1 transmembrane region to the rat Kv1.2 paddle-chimera VSD (PadChVSD). In the Kv1.2 paddle-chimera VSD structure (shown in B) the S3b-S4 paddle motif has been replaced by the one from the rat Kv2.1 channel (35). The R1-Hv1 model (shown in C) was generated by matching all the highly-conserved positions in the four transmembrane segments that have been implicated in Kv VSD function (highlighted in grey and orange in A). The R2-Hv2 model (shown in D) differs from R1-Hv1 only in the alignment of the S4 segment. In R1-Hv1, the three Hv1 arginines were aligned to positions R1, R2, and R3 in the Kv1.2 paddle-chimera, while in R2-Hv1 they were aligned to positions R2, R3, and R4. Notice that positions R1 through R4 (highlighted in orange in A) correspond to arginines in most Kv channel families, including Kv1. The transmembrane segments in the Kv1.2 paddle-chimera VSD are indicated by the horizontal lines above the sequence. The S4 segment is shown in secondary structure representation in panels B, C and D (black, blue and red, respectively). Residues R1 through R4 in the paddle-chimera structure, as well as the three S4 arginines in Hv1, are shown in licorice representation in panels B, C and D.

2.3.1 Kinetic stability of water wires through Hv1.

Both R1-Hv1 and R2-Hv2 develop an open pathway through the center of the channel that is readily occupied by water molecules (see Fig. 2.2). To characterize the kinetics of water wire formation along the permeation pathway, we consider the occurrence of a H-bonded water chain connecting the water-filled extracellular and intracellular crevices in the VSD structure, along the simulation trajectory, as a binary process (i.e. irrespective of identity of the water molecules involved). Block-averaged versions of the corresponding time series are shown in Fig. 2.2, and the corresponding correlation times for the binary process, as well as those of the water wire continuous survival function (see methods for details), are shown in Table 1. This time series analysis reveals that only R1-Hv1 is able to maintain a robust H-bonded water wire throughout the membrane. The differences in kinetic stability between Hv1-R1 and Hv1-R2 can be traced back to the configurations assumed by the water molecules occupying the permeation pathway (see Fig. 2.2).

Table 2.1. Water wire correlation times.

	Binary process[a] (ns)	Continuous survival function[b] (ns)
R1-Hv1	6.5	67.8
R2-Hv1	3.6	53.5

[a]Correlation time from the autocovariance function binary time series (wire/no-wire).

[b]Correlation time from the continuous survival function of configurations showing a wire.

To verify that the water H bond connectivity through the VSD is a unique feature of the Hv1 channel sequence and not an artifact of the homology modeling, we performed a simulation of the R1-Hv1 N214R mutant from an end configuration of the R1-Hv1 trajectory. Consistent with the available experimental evidence (11, 32, 33), we find that formation of a water wire in N214R, after a period of initial equilibration, is sporadic in the time scale of the simulation trajectory (Fig. 2.2C). In addition, the configuration of the water molecules in the interior of the VSD resembles that of nonconducting VSDs (50-54) (Fig. 2.2C).

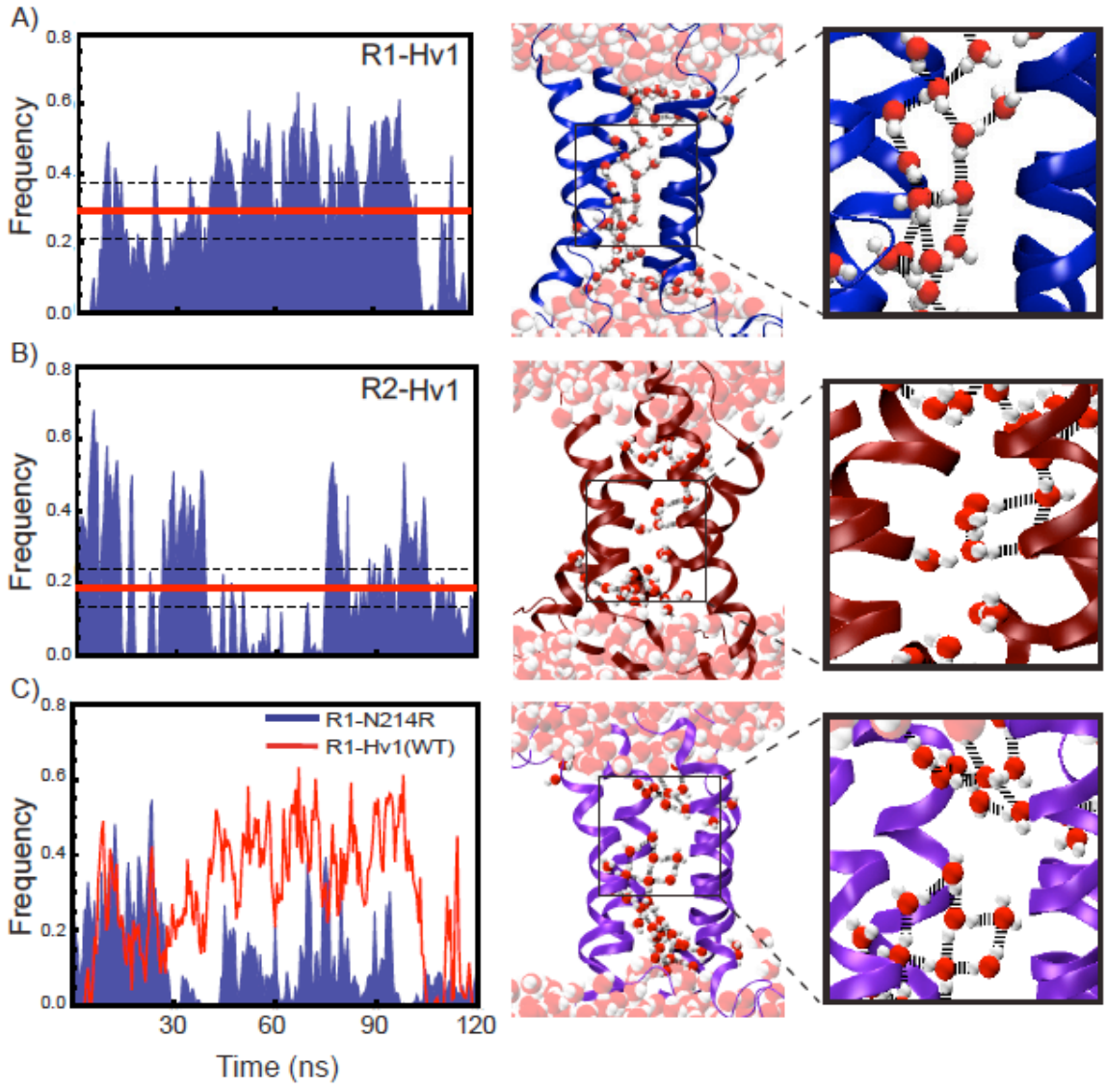

Figure 2.2. Transmembrane water wires in Hv1. A water wire is defined as any instantaneous configuration of H-bonded water molecules connecting the VSD intracellular and extracellular crevices. The frequency of water wire formation in 500-ps trajectory blocks as a function of time is shown in the left panels for R1-Hv1 (A), R2-Hv1 (B), and the N214R variant of R1-Hv1 (C). The red lines in the R1-Hv1 and R2-Hv1 frequency plots corresponds to the frequency of finding a water wire in uncorrelated blocks of 8 ns for R1-Hv1 and 4 ns for R2-Hv1, dashed lines are 95% confidence intervals. The central and right panels show configuration snapshots for the water molecules inside the VSD. The R1-Hv1 model (A) supports a robust water wire through a persistent cluster of water molecules located at the center of the permeation pathway. In the R2-Hv1 model (B), the frequency of water wire formation often goes to zero along the trajectory. The water wire typically breaks at the end of the intracellular crevice. TheR1-Hv1 N214R variant (C) exhibits very little connectivity along the simulation trajectory, after a period of equilibration from the native configuration (first ~30 ns). The

VSD internal waters assume a configuration similar to those observed in simulations of Kv VSDs (50-54). Water molecules are colored by atom (red, oxygen; white, hydrogen). In the central panel, water molecules inside the VSD are shown in ball-and-stick representation, and those outside the VSD are shown as filled-spheres.

2.3.2 Water distribution and protein-water interactions along the permeation pathway.

The water distribution along the transmembrane direction for the paddle-chimera VSD embedded in a lipid bilayer shows limited water penetration into the protein extracellular and intracellular crevices, and a dip to zero in the center of the membrane at the location of a network of internal salt-bridges between highly conserved acidic and basic side chains that is a hallmark of the VSD structure in nonconducting voltage-gated channels (Fig. 2.3) (15, 35, 55-57). In contrast the presence of a permeation pathway in the Hv1 models is immediately evident in their water number density profiles (Fig. 2.3). Both models of Hv1 show a nonzero water density profile throughout the membrane, but they also reveal unique features around the protein core that, as suggested before, are presumably related to the differences on water wire kinetic stability between the models.

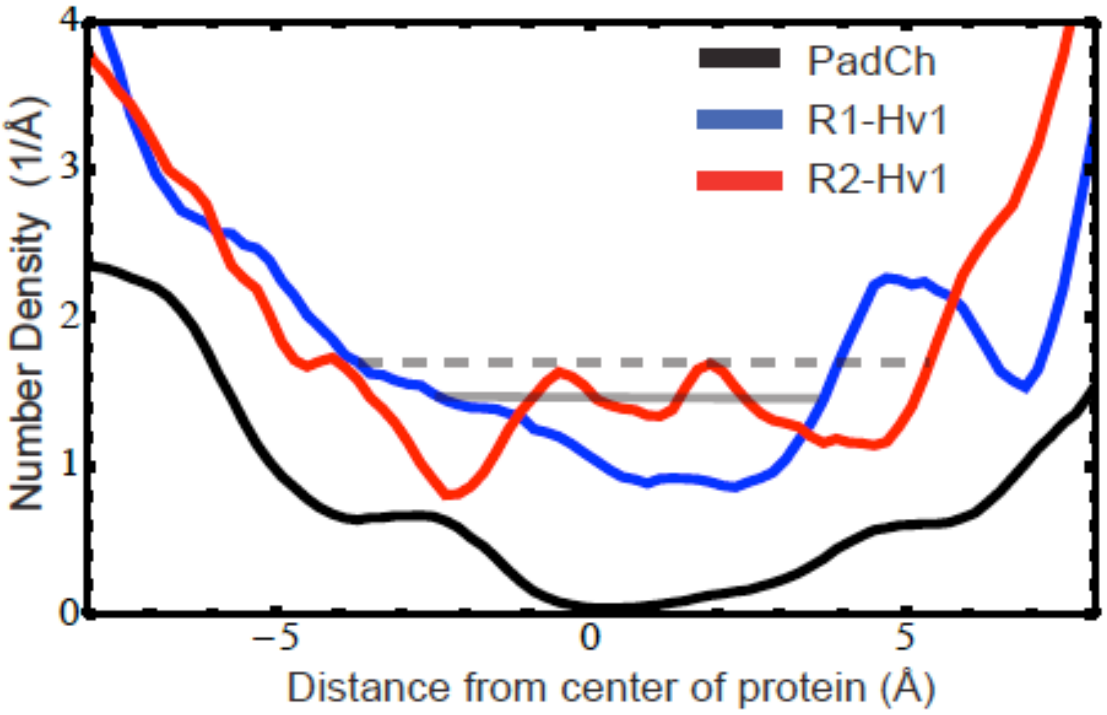

Figure 2.3. Number density profiles for water in the Kv1.2 paddle-chimera VSD (black), R1- Hv1 (blue) and R2-Hv1 (red). Both Hv1 models exhibit a fully hydrated permeation pathway. In contrast, in the Kv1.2 paddle-chimera VSD, a central dry region separates the hydrated intracellular and extracellular crevices. R1-Hv1 exhibits a constriction region that starts roughly at the protein center and extends about 5 Å toward the extracellular side (solid line). R2-Hv1 shows a non-uniform stretch of about 10 Å that extends from the protein intracellular crevice to the extracellular crevice (broken line).

R1-Hv1 exhibits a constriction region that starts roughly at the protein center; it is bounded by F150 on the intracellular side, and extends about 5 Å along the transmembrane direction toward the extracellular side (Figs. 2.3 and 2.4). The constriction is formed by a cluster of hydrophobic side chains (V116, I146 and L147), at the center of protein close to the intracellular side, and by R211 (R3 in S4), which occupies the extracellular side of the constriction (Fig. 2. 4). This particular distribution

of side chains may account for the kinetic stability of the water wire in R1-Hv1. The cluster of hydrophobic side chains, together with F150 on the intracellular crevice, reduces the water H bond connectivity to one or two single files, thereby limiting the water exchange between the intracellular and extracellular crevices. On the other side of the constriction, R211 forms part of a dynamic H-bonded network of polar side chains that occupies the extracellular crevice. This polar network features a salt-bridge chain between R211, E119, R208, and D123 that is coordinated by S181 and S143. Hydration of the network results in water molecules with residence times in the time scale of 100-1000 ps (see Fig. 2. 4).

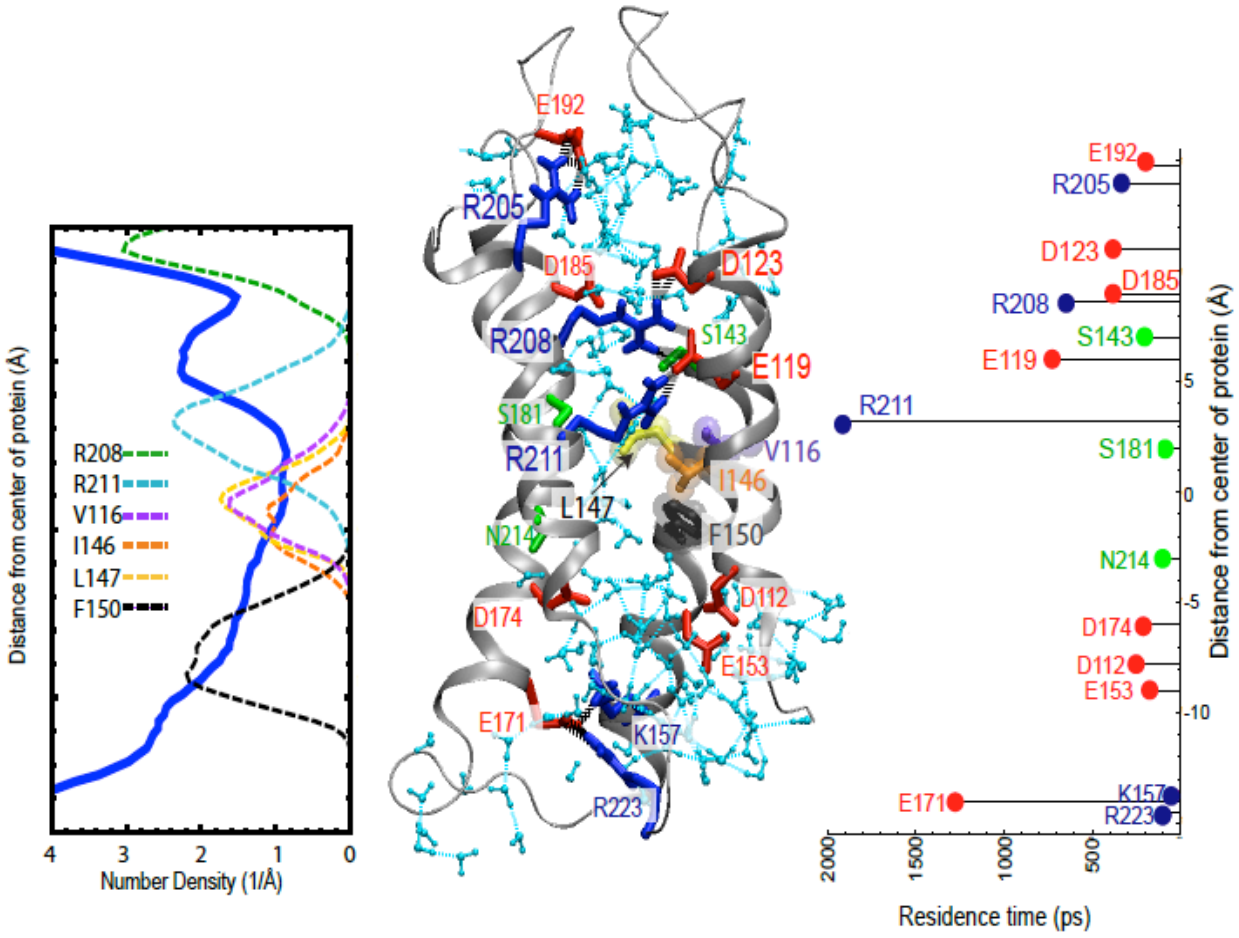

Figure 2.4. R1-Hv1 permeation pathway structure and dynamics. The density profiles on the left panel show that the constriction region in the R1-Hv1 permeation pathway is formed by a cluster of hydrophobic residues (V116, I146 and L147) located, roughly, at the center of the protein, and by R211 in the extracellular cavity. F150 is the closest side chain to the constriction on the intracellular side. N214 is located approximately at the same position as F150 along the transmembrane direction but is away from the constriction. H-bonded networks of waters and polar side chains including S181, S143, and salt-bridge chains between R211, E119, R208 and D123 occupy the extracellular cavity. The residence times of water in this H-bonded network are in the ~1 ns time scale (right panel). Waters in the interior of the channel are colored light blue. Amino acid residues are shown in licorice representation. Basic residues are colored blue, acidic residues are in red, and polar residues are colored green. V116, I146, L147, and F150 are shown in purple, orange, yellow and dark grey, respectively.

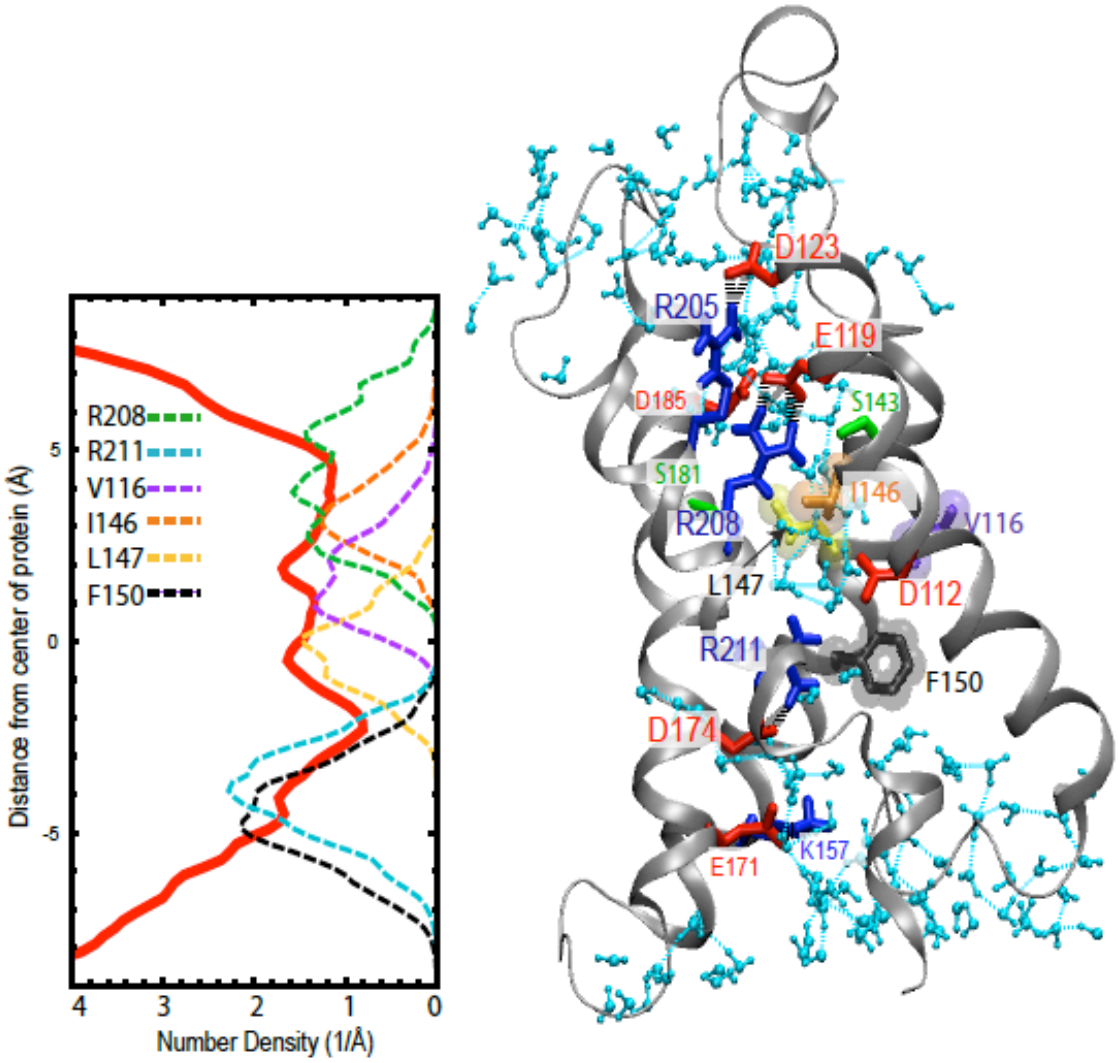

Figure 2.5. R2-Hv1 permeation pathway structure. R2-Hv1 exhibits an extended region of low water density between R211 on the intracellular side and R208 on the extracellular side, and there is not a central cluster of hydrophobic residues as in R1-Hv1. The typical breaking point of the water wire is located at the most constricted site along the permeation pathway formed by the R211-D112 salt-bridge and F150. R208 forms a persistent salt-bridge with E119 and, for most of the trajectory, is separated from the double salt-bridge formed between D174, R211 and D112 by one or two waters. Coloring scheme is as in Figure 4.

In R2-Hv1, the region of low water density along the transmembrane direction is not a single constriction as in R1-Hv1, but a non-uniform stretch of about 10 Å that extends from the protein intracellular crevice to the extracelluar crevice (Figs. 3 and 4). The region of lowest density is located on the intracellular crevice and corresponds to a localized constriction formed by the R211-D112 salt-bridge and by F150. The three side chains are roughly at the same position along the transmembrane direction and reduce the H bond water connectivity to a single file. This crowded arrangement frequently breaks the water wire. R211 is only partially solvated by waters since it also forms a salt-bridge with D174, which is away from the constriction. In contrast to R1-Hv1, there is no evidence of a central hydrophobic cluster or an extracellular polar cluster in R2-Hv1. The V116, I146 and L147 side chains are spread along the pathway constriction. Similar to R211 on the intracellular side, R208 occupies the water density minimum on the extracellular side where interacts with E119. However, a salt-bridge chain involving R211 and R208 with D112 and D174 is broken for most of the trajectory, with R208 separated from D112 by one or two waters. This arrangement may not be conducive to the longer water residence times in the extracellular crevice observed in R1-Hv1.

2.3.3 Water transport through R1-Hv1.

We have shown that R1-Hv1 exhibits persistent H bonded water connectivity between the intracellular and extracellular sides. The stability of these water wires can be accounted for by their interaction with the protein side chains lining the permeation pathway. However, it is plausible that long-lived water wires through the channel can occur concurrently with water permeation, so we calculated the osmotic permeability

coefficient through the R1-Hv1 channel using the method of Zhu et al. (49). We obtained a value of 3.4 x 10^{-28} cm^3/s, while the values reported in the literature for simulations of aquaporin channels are between 10^{-13} and 10^{-15} cm^3/s (58-61). Therefore, despite having a fully permeated interior, the R1-Hv1 model cannot be considered a water channel. A relatively static wire is in good agreement with Hv1's high proton selectivity, because a fairly immobile single file wire would hinder water flux and disfavor permeation of heavy ions.

2.4. Discussion

We have modeled the open state of the Hv1 channel using the crystallographic structure of the Kv1.2 paddle-chimera VSD as a template, relying on the assumption that the crystal structure of its "up-state" conformation is a good approximation for a VSD under depolarizing potentials. Despite the low sequence similarity between Hv1 and the VSD of the Kv1.2-paddle chimera, helices S1 through S3 could be aligned based on the positions of conserved residues known to play important roles in Kv VSD function (e.g., D183 in S1, F233 in S2 and D259 in S3). Even though S4 is the most conserved helix of the VSD, the alignment of different VSDs in the S4 region is not straightforward due to the periodicity of the arginine triplet repeats. Here we probed the two most likely alignments, one in which the first three arginine positions (R1-R3) of the Hv1 S4 correspond to the first three arginine positions of the Kv S4 (Hv1-R1 model), and one in which the R1-R3 positions of the Hv1 S4 correspond to the second, third and forth arginine positions (R2-R4) of the Kv S4 (Hv1-R2 model).Our results suggest that

the Hv1-R1 model can support proton conduction via Grotthus hopping along a robust water wire.

State-dependent internal salt-bridge networks between the basic residues in S4 and highly conserved positions for acidic residues in S1-S3 are a hallmark of the VSD structure, and have shown to be key in folding, stability and function (15, 55-57). Hv1 not only lacks one of the R1-R4 arginines in S4, but the number and distribution of conserved positions for acidic side chains in S1-S3 differ from the ones in nonconducting VSDs. The most constricted region in the up-state conformation of the Kv1.2 paddle-chimera VSD is formed by R4 (R299), and three S2 side chains (E226, I230, and F233). These hydrophobic side chains, which are also highly conserved, have been shown to play a crucial role in the molecular mechanism of voltage-dependent activation in Kv VSDs (27, 62). Our R1-HV1 model preserves the hydrophobic component of this arrangement, while the two small polar side chains replacing the salt-bridge (N214 and S148, respectively) are away from the center of the channel, thereby eliminating the steric hindrance imposed by the salt-bridge pair. Despite the loss of the innermost pair, the extracellular salt-bridge network in Hv1, involving R2 and R3, remains in place due to an additional conserved acidic position in S1 (E119).

In contrast, in the R2-Hv2 model, the most constricted region of the channel is formed by F150 and the R3-D112 salt-bridge pair, which leads to a partially open pathway. In addition, the extracellular salt-bridge network is broken. Similarly, the introduction of an arginine side chain at the same location of F150 along the transmembrane direction, leads to a mostly closed pathway in the R1-Hv1 N214R variant.

Previously, Ramsey et al. reported homology models of the Hv1 channel using the Kv1.2 paddle-chimera structure as a template and a similar alignment to our R2-Hv1 model (32). Consistent with our results, their models show a fully hydrated pathway connecting the intracellular and extracellular sides in 20-ns long atomistic simulations. In the first 20 ns of our equilibrated trajectories, the VSDs of the R1-Hv1 and R2-Hv1 models displayed significant differences in core hydration compared to the VSD of the Kv1.2 paddle chimera. But, only with longer simulations it became apparent that the R1-Hv1 model could support a water wire more effectively than the R2-Hv1 model. This is consistent with the idea that in order to compare the overall stability of two water wires, the trajectories need to be long enough to capture a significant number of breaks in at least one wire.

The experimental evidence available to date on the biophysics of Hv channels (1, 2, 11, 16, 17, 32, 33) seems to align with the classical view that proton conduction through membranes occurs over H-bonded water chains (63, 64). Furthermore, despite the abundance of titratable side chains lining the putative permeation pathway, no single residue has been identified that could account for proton selectivity (32, 33). The existence of a fully-hydrated permeation pathway in Hv1 could be extrapolated from the available structural evidence on Kv channels VSDs both crystallographic (35) and in membrane environments (50, 65). Our molecular models for Hv1 in lipid membrane provide two additional insights. First, the formation of a robust water wire connecting both sides of the membrane is dependent on the same structural features that are associated with the VSD gating function. This is consistent with the notion that both gating and permeation occur through the same structural pathway. Second, the water

wire through Hv1 is not accompanied by water transport. Since the energetic cost of dehydrating an ion is prohibitively large (66), no water transport implies that there is also no heavy ion transport, suggesting that proton selectivity in Hv1 may also be a consequence of the VSD architecture.

2.5 References

1. Sasaki M, Takagi M, & Okamura Y (2006) A voltage-sensor domain protein is a voltage-gated proton channel. *Science* 312:589-592.
2. Ramsey IS, Moran MM, Chong JA, & Clapham DE (2006) A voltage-gated proton-selective channel lacking the pore domain. *Nature* 440:1213-1216.
3. Ramsey SI, Ruchti E, Kaczmarek JS, & Clapham DE (2009) Hv1 proton channels are required for high-level NADPH oxidase-dependent superoxide production during the phagocyte respiratory burst. *Proc. Natl. Acad. Sci. U.S.A.* 106:7642-7647.
4. Okochi Y, Sasaki M, Iwasaki H, & Okamura Y (2009) Voltage-gated proton channel is expressed on phagosomes. *Biochem. Biophys. Res. Commun.* 382:274-279.
5. El Chemaly A*, et al.* (2010) VSOP/Hv1 proton channels sustain calcium entry, neutrophil migration, and superoxide production by limiting cell depolarization and acidification. *The Journal of Experimental Medicine* 207:129-139.
6. Capasso M*, et al.* (HVCN1 modulates BCR signal strength via regulation of BCR-dependent generation of reactive oxygen species. *Nat Immunol* 11(3):265-272.
7. Musset B*, et al.* (2008) A pH-stabilizing role of voltage-gated proton channels in IgE-mediated activation of human basophils. *Proc Natl Acad Sci U S A* 105(31):11020-11025.
8. Lishko PV, Botchkina IL, Fedorenko A, & Kirichok Y (2010) Acid extrusion from human spermatozoa is mediated by flagellar voltage-gated proton channel. *Cell* 140:327-337.
9. Iovannisci D, Illek B, & Fischer H (Function of the HVCN1 proton channel in airway epithelia and a naturally occurring mutation, M91T. *J Gen Physiol* 136(1):35-46.
10. Lee S-Y, Letts JA, & MacKinnon R (2008) Dimeric subunit stoichiometry of the human voltage-dependent proton channel of Hv1. *Proc. Natl. Acad. Sci. U.S.A.* 105:7692-7695.

11. Tombola F, Ulbrich MH, & Isacoff EY (2008) The voltage-gated proton channel Hv1 has two pores, each controlled by one voltage sensor. *Neuron* 58:546-556.

12. Koch HP*, et al.* (2008) Multimeric nature of voltage-gated proton channels. *Proc. Natl. Acad. Sci. U.S.A.* 105:9111-9116.

13. Aggarwal SK & MacKinnon R (1996) Contribution of the S4 segment to gating charge in the *Shaker* K^+ channel. *Neuron* 16:1169-1177.

14. Schoppa NE, McCormack K, Tanouye MA, & Sigworth FJ (1992) The size of gating charge in wild-type and mutant *Shaker* potassium channels. *Science* 255:1712-1715.

15. Seoh SA, Sigg D, Papazian DM, & Bezanilla F (1996) Voltage-sensing residues in the S2 and S4 segments of the Shaker K^+ channel. *Neuron* 16(6):1159-1167.

16. Gonzalez C, Koch HP, Drum BM, & Larsson HP (2010) Strong cooperativity between subunits in voltage-gated proton channels. *Nature Struct. Mol. Biol.* 17:51-56.

17. Tombola F, Ulbrich MH, Kohout SC, & E.Y. I (2010) The opening of the two pores of the Hv1 voltage-gated proton channel is tuned by cooperativity. *Nature Struct. Mol. Biol.* 17:44-50.

18. Larsson B, Baker OS, Dhillon DS, & Isacoff EY (1996) Transmembrane movement of the *Shaker* K+ channel S4. *Neuron* 16:387-397.

19. Mannuzzu LM, Moronne MM, & Isacoff EY (1996) Direct physical measure of conformational rearrangement underlying potassium channel gating. *Science* 271(5246):213-216.

20. Ruta V, Chen J, & MacKinnon R (2005) Calibrated measurement of gating-charge arginine. *Cell* 123:463-475.

21. Pathak MM*, et al.* (2007) Closing in on the resting state of the Shaker K^+ channel. *Neuron* 56:124-140.

22. Alabi AR, Bahamonde MI, Jung HJ, Kin JI, & Swartz KJ (2007) Portability of paddle motif function and pharmacology in voltage sensors. *Nature* 450:370-376.

23. Starace DM & Bezanilla F (2001) Histidine scanning mutagenesis of basic residues of the S4 segment of the Shaker K^+ channel. *J. Gen. Physiol.* 117(5):469-490.

24. Starace DM & Bezanilla F (2004) A proton pore in a potassium channel voltage sensor reveals a focused electric field. *Nature* 427:548-553.

25. Tombola F, Pathak MM, Gorostiza P, & Isacoff EY (2007) The twisted ion-permeation pathway of a resting voltage-sensing domain. *Nature* 445:546-549.

26. Tombola F, Pathak MM, & Isacoff EY (2005) Voltage-sensing arginines in a potassium channel permeate and occlude cation-selective pores. *Neuron* 45:379-388.

27. Campos FV, Chanda B, Roux B, & Bezanilla F (2007) Two atomic constraints unabiguously position the S4 segment relative to S1 and S2 segments in the closed state of Shaker K Channel. *Proc. Natl. Acad. Sci. U.S.A.* 104:7904-7909.

28. Sokolov S, Scheuer T, & Catterall WA (2005) Ion premeation through a voltage-sensitive gating pore in brain sodium channels having voltage sensor mutations. *Neuron* 47:183-189.

29. Sokolov S, Scheuer T, & Caterall WA (2007) Gating pore current in an inherited ion channelopathy. *Nature* 446:76-78.

30. Struyk AF & Cannon SC (2007) A Na+ channel mutation linked to hypokalemic periodic paralysis exposes a proton-selective gating pore. *J Gen Physiol* 130(1):11-20.

31. Chanda B & Bezanilla F (2008) A common pathway for charge transport through voltage-sensing domains. *Neuron* 57:345-351.

32. Ramsey IS*, et al.* (2010) An aqueous H^+ permeation pathway in the voltage-gated proton channel Hv1. *Nature Struct. Mol. Biol.*:1-7.

33. Sakata S*, et al.* (2010) Functionality of the voltage-gated proton channel truncated in S4. *Proc. Natl. Acad. Sci. U.S.A.* 107:2313-2318.

34. Lee S-Y, Banerjee A, & MacKinnon R (2009) Two separate interfaces between the voltage sensor and pore are required for the function of voltage-dependent K^+ channels. *PLoS Biol.* 7:0676-0686.

35. Long SB, Tao X, Campbell EB, & Mackinnon R (2007) Atomic structure of a voltage-dependent K^+ channel in a lipid membrane-like environment. *Nature* 450:376-382.

36. Sali A & Blundell TL (1993) Comparative protein modelling by satisfaction of spatial restraints. *J. Mol. Biol.* 234:779-815.

37. Phillips JC*, et al.* (2005) Scalable molecular dynamics with NAMD. *J. Comput. Chem.* 26:1781-1802.

38. MacKerell AD, Jr.*, et al.* (1998) All-atom empirical potential for molecular modeling and dynamics studies of proteins. *J. Phys. Chem. B* 102(18):3586-3616.

39. Klauda JB, Brooks BR, MacKerell AD, Jr., Venable RM, & Pastor RW (2005) An ab initio study on the torsional surface of alkanes and its effect on molecular simulations of alkanes and a DPPC bilayer. *J. Phys. Chem. B* 109:5300-5311.

40. Jorgensen WL, Chandrasekhar J, Madura JD, Impey RW, & Klein ML (1983) Comparison of simple potential functions for simulating liquid water. *J. Chem. Phys.* 79(2):926-935.

41. Essmann U*, et al.* (1995) A smooth particle mesh Ewald method. *J. Chem. Phys.* 103:8577-8593.

42. Darden T, York D, & Pedersen L (1993) Particle mesh Ewald: An $N \cdot \log(N)$ method for Ewald sums in large systems. *J. Chem. Phys.* 98:10089-10092.

43. Grubmüller H, Heller H, Windemuth A, & Schulten K (1991) Generalized Verlet algorithm for efficient molecular dynamics simulations with long-range interactions. *Mol. Simul.* 6:121-142.

44. Ryckaert J-P, Ciccotti G, & Berendsen HJC (1977) Numerical integration of the Cartesian equations of motion of a system with constraints: Molecular dynamics of *n*-alkanes. *Journal of Computational Physics* 23:327-341.

45. Miyamoto S & Kollman P (1992) An analytical version of the SHAKE and RATTLE algorithm for rigid water models. *J. Comput. Chem.* 13:952-962.

46. Martyna GJ, Tobias DJ, & Klein ML (1994) Constant-pressure molecular-dynamics algorithms. *J. Chem. Phys.* 101:4177-4189.

47. Feller SE, Zhang Y, Pastor RW, & Brooks BR (1995) Constant pressure molecular dynamics simulation: The Langevin piston method. *J. Chem. Phys.* 103(11):4613-4621.

48. Humphrey W, Dalke W, & Schulten K (1996) VMD: Visual molecular dynamics. *J. Mol. Graph.* 14(1):33-38.

49. Zhu F, Tajkhorshid E, & Schulten K (2004) Collective diffusion model for water permeation through microscopic channels. *Phys Rev Lett* 93(22):224501.

50. Krepkiy D*, et al.* (2009) Structure and hydration of membranes embedded with voltage-sensing domains. *Nature* 462:473-479.

51. Freites JA, Tobias DJ, & White SH (2006) A voltage-sensor water pore. *Biophys. J.* 91:L90-L92.

52. Jogini V & Roux B (2007) Dynamics of the Kv1.2 voltage-gated K1 channel in a membrane. *Biophys. J.* 93:3070-3082.

53. Sands ZA & Sansom MSP (2007) How does a voltage sensor interact with a lipid bilayer? Simulations of a potassium channel domain. *Structure* 15:235-244.

54. Treptow W & Tarek M (2006) Environment of the gating charges in the Kv1.2 *Shaker* potassium channel. *Biophys. J.* 90(9):L64-L66.

55. Papazian DM*, et al.* (1995) Electrostatic interactions of S4 voltage sensor in Shaker K^+ channel. *Neuron* 14(6):1293-1301.

56. Tiwari-Woodruff SK, Schulteis CT, Mock AF, & Papazian D (1997) Electrostatic interactions between transmembrane segments mediate folding of *Shaker* K^+ channel subunits. *Biophys. J.* 72:1489-1500.

57. Zhang L*, et al.* (2007) Contribution of hydrophobic and electrostatic interactions to the membrane integration of the Shaker K^+ channel voltage sensor domain. *Proc. Natl. Acad. Sci. U.S.A.* 104(20):8263-8268.

58. Jensen MØ & Mouritsen OG (2006) Single-channel water permeabilities of *Escherichia coli* aquaporins AqpZ and GllF. *Biophys J.* 90:2270-2284.

59. Hashido M, Kidera A, & Ikeguchi M (2007) Water transport in aquaporins: osmotic permeability matrix analysis of molecular dynamics simulations. *Biophys J.* 93:373-385.

60. Hashido M, Ikeguchi M, & Kidera A (2005) Comparative simulations of aquaporin family: AQP1, AQPZ, AQP0 and GlpF. *FEBS Lett.* 579:5549-5552.

61. Jensen MO*, et al.* (2008) Dynamic control of slow water transport by aquaporin 0: implications for hydration and junction stability in the eye lens. *Proc Natl Acad Sci U S A* 105(38):14430-14435.

62. Tao X, Lee A, Limapichat W, Dougherty DA, & MacKinnon R (2010) A gating charge transfer center in voltage sensors. *Science* 328:67-73.

63. Decoursey TE (2003) Voltage-gated proton channels and other proton transfer pathways. *Physiol. Rev.* 83:475-579.

64. Nagle JF & Morowitz HJ (1978) Molecular mechanisms for proton transport in membranes. *Proc Natl Acad Sci U S A* 75(1):298-302.

65. Chakrapani S, Cuello LG, Cortes DM, & Perozo E (2008) Structural dynamics of an isolated voltage-sensor domain in a lipid bilayer *Structure* 16:398-409.

66. Wilson MA & Pohorille A (1996) Mechanism of unassisted ion transport across membrane bilayers. *J. Am. Chem. Soc.* 118:6580-6587.

Chapter 3

Microsecond simulations of an open state model of the human Hv1 proton channel

3.1 Introduction

The human voltage-gated proton channel (hHv1) forms as a dimer consisting of two voltage-sensing domains (VSDs) but uniquely lacks a central pore domain. The recently solved structure of a voltage-gated proton channel chimera revealed the first insights into the resting state of a proton channel in a trimeric assembly(1). We assess the physiologic stability of the crystal structure in a trimeric and monomeric state after running microsecond simulations of the structure embedded in a fully hydrated lipid bilayer. A resting state homology model of the hHv1 channel was built using the crystal

structure as a template and run under a hyperpolarizing and depolarizing potential, producing an 8Å sliding-helix movement of the S4 segment and a gating charge displacement of 2.5e consistent with electrophysiology measurements. Voltage induced salt-bridge exchange yields experimentally predicted interactions between the putative selectivity filter and highly conserved arginines at an opening potential. An electric-field focusing feature reminiscent of non-conducting VSDs appears at a hyperpolarizing potential but is reshaped under an opening potential, revealing a second focusing feature around a highly conserved hydrophobic residue in the S1 helix (Val116). The final configuration of the channel after 20μs of opening potential supports hydrogen-bonded chains and recapitulates experimentally derived interactions between a small-molecule open-state blocker and the protein, supporting the notion that this structure represents an open-state model of hHv1.

Hv1 activity has been linked to stroke, hypertension and multiple sclerosis(2). Functional blockade of Hv1 inhibits highly metastatic breast cancer progression, highlighting channel blockade as a promising new avenue for therapeutics(3). Small-molecules blocking the open-state of Hv1 have been modified based on experimental insights to improve inhibitory activity but will continue to benefit from refinement as our understanding of channel structure evolves(4, 5). We present the first open-state structure of the human Hv1 proton channel generated from simulations of the recently solved voltage-gated proton channel chimera crystal structure in a realistic membrane environment under physiologically relevant potentials. This model provides insights useful for drug design, while the simulations further our understanding of VSD gating and permeation.

Hv1 is expressed in a wide range of tissues and serves a variety of important physiological functions. The channel is present in the medullary thick ascending limb of the kidney and acts as a sodium sensor, promoting superoxide production when intracellular Na is low(6). In phagocytes, the channel is functionally coupled with NADPH oxidase to repolarize the membrane potential after the respiratory burst, which is essential for pathogen elimination (7). The channel activates spermatozoa by inducing intracellular alkalization, making it an attractive target for controlling male fertility (8). In B-lymphocytes, channel activity enhances B-cell proliferation and differentiation through the B-cell antigen receptor (BCR) mediated intracellular signaling cascade that leads to B-cell proliferation and differentiation(9, 10).

Channel activity has been linked to several pathologic processes as well. In a mouse model of cuprizone-induced demyelination, a model for multiple sclerosis, Hv1 expression in microglial cells is required for NADPH-dependent ROS production(11). Mice lacking Hv1 have reduced ROS production and are partially protected from demyelination and motor deficits that follow cuprizone exposure, suggesting microglial Hv1 is a unique target for controlling the pathogenesis of multiple sclerosis. Channel expression is also increased in highly metastatic glioma, breast and colon cancer tissues and cell lines(3, 12, 13). Functional blockade of Hv1 using RNA-interference technology results in markedly decreased cellular proliferation and migration in both breast cancer and colon cancer cell lines (3, 12). In metastatic glioma cell lines, inhibition of Hv1 activity by zinc chloride induces apoptosis (12). Clinically, Hv1 expression is correlated with shorter overall and recurrence-free survival in both colorectal and breast cancer patients. In ischemic stroke patients, Hv1-dependent ROS

production is responsible for a substantial fraction of brain damage (14).

Compounds modulating Hv1 activity have potential applications in the diagnosis, prognosis and treatment of cancer metastasis, multiple sclerosis and stroke. To date, only three types of molecules have been identified as direct Hv1 inhibitors: Zn2+ (and other polyvalent cations), Hanatoxin and guanidine derivatives(15). The first guanidine derivative described by Hong et al (2GBI) was only able to block the channel current from the intracellular side with relatively low affinity(4, 5). However a simple modification to the 2GBI yields a compound able to bind from the extracellular side with 60% increased proton current inhibition, suggesting that optimization of guanidine derivatives based on the 2GBI scaffold can lead to clinically useful Hv1 inhibitors. The compounds have also revealed details regarding the structure of the inner vestibule and gating properties of the channel.

Hv1 is a member of the voltage-gated ion channel (VGIC) superfamily, which is composed of potassium (Kv), sodium (NaV), and calcium (CaV) channels. Typical VGICs have four subunits, each with 6 TM segments. The first four TM segments (S1-S4) form a voltage-sensing domain (VSD) and the last two form part of the pore domain. Hv1 lacks a designated pore domain and has only two subunits, each with four TM segments (S1-S4) which are homologous to the voltage-gated potassium channel VSD. In the plasma membrane Hv1 is expressed as a homodimer stabilized by an intracellular coiled coil in the C-terminus and an extracellular intersubunit interface, formed in part by interactions between S1 from each monomer(16). Deletions of Hv1's C-terminus inhibit the formation of dimers and create fully functional monomeric subunits, each with their own permeation pathway and voltage sensor(17, 18).

In voltage-gated potassium (Kv) channels, pore opening and closing is controlled (gated) by movement of the VSDs, which do not conduct ions and are highly sensitive to TM potential(19) Voltage sensitivity is conferred by a series of highly conserved residues, termed gating charges, which move through the membrane electric field in response to changes in TM potential(20, 21). The gating charges are primarily S4 basic residues (mostly arginines) occurring in triplet repeats of a basic side chain followed by two hydrophobic residues. In the *Shaker* Kv channel, the first four arginines in S4 (termed R1 through R4) contribute most of the gating charge during activation.(20, 22, 23) Hv1 exhibits three of these repeats, and mutations of the S4 arginines have been shown to alter its activation kinetics(24, 25).

Voltage-clamp fluorometry and state-dependent accessibility measurements in Hv1 report motion of S4 during activation,(26, 27) which has also been observed in Kv channels (28-31). A helical hairpin made of portions of Hv1's S3 and S4 helices can be transplanted into a Kv channel without loss of function.(32) These findings established a structural connection between Hv1 and nonconducting VSDs, motivating the use of Kv and NaV VSD crystal structures as templates for Hv1 homology models. The low sequence identity (13-19%) between Hv1 and NaV/Kv VSDs, as well as ambiguities in structural sequence alignment in the S4 region, led to a wide variety of models being proposed. Features such as salt-bridge paring and VSD hydration patterns differed depending upon the initial sequence alignment of the S4 helix in the template and hHv1. By contrast, the crystal structure for a *Mus musculus* Hv1 chimera (mHv1cc), solved to 3.45 Å resolution, has 65% sequence identity with human Hv1 in the TM regions.

Using Anton, a special purpose machine for MD simulations of biomolecules, we

ran multi-microsecond simulations of three systems: the mHv1cc trimer directly from the crystal structure, a mHv1cc monomer and a homology model of human Hv1 based on the mHv1cc monomer. We present an analysis of the stability and hydration of all three three systems when they are run for several microseconds in a hydrated lipid bilayer without an applied potential. To begin to investigate the gating and permeation mechanisms of Hv1, we ran the hHv1 model under an applied hyperpolarizing and depolarizing potential. We describe the salt-bridge exchanges giving rise to translocation of all three S4 arginines involved in the voltage activation of Hv1. We find a unique electrostatic focusing feature near a highly conserved valine in the S1 segment and characterize the changing electrostatic fingerprint of the VSD. The final configuration of the channel and the preceding several microseconds of simulation under a depolarizing potential recapitulate several experimental measures, including gating charge movement and 2GBI-protein interactions, pointing to the validity of our model as an open-state structure. This represents the first open-state structure for the human Hv1 channel generated from the mHv1cc crystal structure in a realistic membrane environment using a physiologically relevant potential to activate (i.e. open) the channel. The putative open-state structure enables a detailed understanding of drug-channel interactions and provides a template for high-throughput *in silico* screening for drugs targeting the open-state. In depth knowledge of Hv1's open state will ultimately allow for a more refined, structure-based approach to designing high affinity channel blockers with a variety of potential therapeutic uses.

3.2 Methods

3.2.1 System Setup

Starting with the chimera coordinates(accession code 3WKV) for the trimer or monomer, we built in the missing loops using Phyre2.0 (33). Experimental evidence suggests the physiologically relevant conducting state of the channel is either a dimer or a monomer truncated at the C-terminus.[3,4] Thus, we truncated the construct at E227 (R230 in human) in the C-terminus. We extracted one monomer from the trimer for the mHv1cc monomer simulation. We constructed a model of the *Homo Sapiens* Hv1 (hHv1), using the mHv1cc monomer coordinates as a template and the alignment presented by Takeshita et al. The final hHv1 construct is composed of residues F88 to R230. The protein constructs (F84 to E227 for the crystal structure constructs and F88 to R230 for hHv1) were inserted into a POPC ([(2*R*)-3-hexadecanoyloxy-2-[(*Z*)-octadec-9-enoyl]oxypropyl] 2(trimethylazaniumyl) ethyl phosphate) lipid bilayer, allowing the putative S0 helix (residues F84-S93/F88-S97) to be in the phosphate headgroup region of the bilayer and unburying the shortest extracellular loop between S1 and S2. We used CHARMM-GUI to embed the structures into a fully hydrated bilayer with150 mM NaCl for a total 91,969 atoms in the trimer system, 58,192 atoms for the mouse monomer system, and 58,241 for the human monomer system. Specifically, the hHV1 system is composed of 174 POPC molecules, 34 Na+, 38 Cl- and 10,788 waters. The monomeric mHv1cc system has 174 POPC molecules, 37 Na+, 36 Cl- and 10,788 waters. The trimer has 224 POPC molecules, 18,177 water molecules, 54 Na+ and 51Cl-.

3.2.2 Minimization and equilibration using NAMD2.9

We used the following protocol for all three systems (the mHv1cc trimer, the mHv1cc monomer and the hHv1 monomer). After 5000 steps of minimization with all protein atoms constrained, we ran the systems with 100ps in the constant temperature (T=300K), constant volume (NVT) ensemble, allowing the lipid molecules to relax. The systems were then equilibrated for several ns in the NPT ensemble (P=1atm T=300K) with the protein backbone atoms restrained harmonically to their initial positions and slowly released over 10ns using a decreasing force constant equal to 50kcal $mol^{-1}Å^{-1}$, 25kcal $mol^{-1}Å^{-1}$, 10kcal $mol^{-1}Å^{-1}$, 5kcal $mol^{-1}Å^{-1}$, and 2kcal $mol^{-1}Å^{-1}$. After the backbone was completely released, we ran the system several nanoseconds without an applied bias.

3.2.3 Microsecond timescale molecular dynamics simulation details

After several nanoseconds of equilibration with NAMD2.9, the systems were transferred to Anton, a special-purpose computer for molecular dynamics simulations of biomolecules, and simulated for several microseconds (Table 3.1), The CHARMM27 and CHARMM36 force fields were used for the protein and lipids, respectively, and the TIP3P model was used for water. Anton software version 2.12.4 was used. Specific simulation parameters are similar to those used during our previous Anton allocations (34). Briefly, an r-RESPA algorithm was employed to integrate the equations of motion with a time step of 6 fs for the long-range non-bonded forces, and 2 fs for short-range non-bonded and bonded forces. The k-Gaussian split Ewald method (35) was used for

long-range electrostatic interactions. All bond length involving hydrogen atoms were constrained using the SHAKE algorithm. The simulations were performed at constant temperature (300K) and pressure (1 atm), using Nose-Hoover chains and the Martyna-Tobias-Klein barostat (36). The RESPA algorithm and the temperature and pressure controls were implemented using the multigrator scheme.

Table 3.1: Summary of trajectories

System	Trajectory length (ms)
Chimera mHv1cc Trimer	7.8
Chimera mHv1cc Monomer	6.7
Human Hv1 Monomer	
No potential	7.3
Hyperpolarized	7.5
Depolarized	24.0

3.2.4 Water dynamics analyses

We define a transmembrane water wire as any configuration of H bonded waters in the channel connecting the extracellular side to the intracellular side. A H bond was defined using conventional geometric criteria (donor-acceptor distance < 3.5 Å and donor-hydrogen-acceptor angle > 140 Å). Water wire formation along each simulation trajectory was modeled as a binary process wire/no-wire, irrespective of the actual number of H bonded configurations or the identity of the water molecules. The reported correlation times correspond to single-exponential fits to the binary process

autocorrelation function and to the continuous time correlation function computed only over the configurations showing a wire. The latter is defined as

$$C(t) = \frac{\langle H(t)H(0)\rangle}{\langle H^2\rangle}$$

where *H(t) = 1* if a water wire has been present continuously from *t = 0* to time *t*, and *H(t) = 0* otherwise.

3.2.5 Membrane potential and gating charge

To model the applied membrane potential, we imposed a constant electric field with a magnitude equal to 120 mV/23 Å. The specific value for the thickness of the dielectric barrier was taken from a linearized Poisson- Boltzmann calculation of the electrostatic potential along a transmembrane axis passing through the center of the VSD, as previously described. The total charge displacement with respect to the initial configuration (Δq) was calculated as

$$\Delta q = \sum qi\ (\Phi m[zi(t)] - \Phi m[zi(0)])\ i$$

where t is time, Φm is the fractional membrane potential, and zi and qi are the position along the transmembrane direction and the partial charge of the *ith* atom, respectively. The sum was taken over the partial charges of the atoms that constitute the centers of charge of all the VSD basic and acidic side chains. The gating-charge displacement (Q) between the depolarized and hyperpolarized trajectories was calculated as

$$Q = \langle \Delta q \rangle\ d - \langle \Delta q \rangle\ h$$

where < Δq >d is the average charge displacement over the last μs of the depolarized trajectory and < Δq >h is the average charge displacement over the last μs of the hyperpolarized trajectory.

3.2.6 Docking

The docking calculations were performed using a Monte Carlo simulated annealing method implemented in the AutoDock Vina software package(37). Twenty protein configurations were selected from clustered configurations of the four internal residues in hHv1 that represent the selectivity filter at the center of the pore (D112, R211, F150, S181) from the last ~10 μs of the trajectory under depolarizing potential, in which S4 was in the up position. The clustering was performed using the VMD clustering utility (38) with an RMSD cutoff of 2.0 Å for non-hydrogen atoms in these four residues. The centroid structure from each cluster was selected as the target for rigid docking of the 2-GBI ligand. Twenty docking poses for 2-GBI were generated by AutoDock Vina within the search space confined to a cuboid of dimensions 33x33x24 $Å^3$ in the intracellular vestibule of the pore. The 400 poses were clustered with a 1.0 Å RMSD cutoff for non-hydrogen atoms of 2-GBI. The five most populated clusters had 2-GBI located directly below the selectivity filter in the intracellular vestibule with the guanidine moiety in proximity to R211 and D112 and the benzimidazole moiety facing F150 (Figure 3.5). An identical docking simulation was performed on the closed state using the ~7 μs trajectory of hHv1 with a hyperpolarizing potential. The selectivity filter for the closed state was chosen to be the four residues: D112, R205, F150, S181. The five most populated clusters for the closed state docking with a 1.0 Å RMSD cutoff for non-

hydrogen atoms either did not place 2-GBI near the selectivity filter or positioned it in a non-physical orientation compared to the mutant-cycle analysis results.

3.3 Results

3.3.1 The closed crystal structure and homology model in a hydrated lipid bilayer are stable on the microsecond timescale

We performed several microsecond all-atom MD simulations of the mHv1cc trimer, the mHv1cc monomer and an Hv1 model of the TM region of Hv from Homo Sapiens. All three proteins were embedded in a POPC lipid bilayer in excess water. The mHv1cc construct is a chimera where the cytoplasmic coiled coil (Val216–Asn269) and large intracellular portions of the S2–S3 (Glu149–Phe171) are replaced with the leucine-zipper transcriptional activator GCN4 from *S. cerevisiae* (Arg249–Arg281) and the intracellular portion of *Ciona intestinalis* voltage-sensing phosphatase (Asp164–Leu188), respectively(39). The transmembrane region for the human Hv1 model was constructed using the mHv1cc monomer as a template and the alignment from Takeshita et al.(39) Inter-segmental loops missing from the crystal structure were built using the Phyre2.0 web-server(33).

Examining the root-mean-squared deviation for the alpha carbons, we find that all three systems are stable on the multi-microsecond timescale. In the initial hundreds of nanoseconds of trimer simulation, the RMSD for alpha-carbons in each monomer versus time increases steeply for all three monomers. However, within the first 4 μs monomers 2 and 3 appear to have correlated motions separate from monomer 1, then

at around 4μs, monomer 1 and 2 appear to be correlated (Figure 3.1) separate from monomer 3. Not all monomers behave the same, and despite the triple coiled-coil motif, there appears to be a preference for correlative motions between pairs (versus triplets) of monomers. Over time and with the aid of an appropriate stimulus, likely involving disruption of the zipper, a monomer could potentially be expelled from the structure, favoring a more physiologically relevant dimeric state. This simulation provides a starting point for further investigation into the allosteric interactions between monomers in a trimer versus a dimer.

Prior to the publication of the structure, studies probing channel oligomerization and intersubunit interfaces revealed an intracellular S4-S4 coiled coil and suggested a possible extracellular S1-S1 dimer contact, a possible extracellular S2-S2 dimer contact or a dimer of dimers with both contacts(16, 40, 41). Crosslinking and blocker binding studies have further enforced the validity of the extracellular S1-S1 interaction(16). Detailed insights about this dimeric interface from our crystal structure trimer simulations are limited. In our system, the extracellular end of S1 is positioned closest to the extracellular end of S3 and separated from the next VSDs S1 by around 35Å.

The average RMSD versus sequence for each TM segment reveals the S2 helix is the most dynamic of all four segments. In the trimer system, S2 faces the membrane and is the only segment without inter-VSDs contacts, explaining the high RMSD. However, the S2 segment remains highly dynamic in the monomer simulations, implicating intra-VSD interactions. One possible explanation is that the S2 lacks the acidic residue conserved across non-conducting VSDs, termed E2 (E283 in Shaker). In lieu of a strong acid capable of forming strong salt-bridges, a serine (S143 in hHv1) is

highly conserved in proton channels across species and likely plays an important role in distinguishing Hv1's functional properties from Kv/NaV VSDs.

At the C-terminus, the introduction of the triple coiled-coil leucine-zipper motif was essential for crystallization, increasing the construct's thermostability. Thus, predictably, the C-terminus is highly stable throughout the simulation in the trimer, but loses its secondary structure in the monomeric simulations. The crystal structure also has an S0 helix located near the polar-apolar membrane interface, which we included in all three systems. The S0 segment of one of the monomers in the trimer loses its secondary structure and becomes highly dynamic (Figure 3.1), suggesting that the electron density in the region of S0 in the crystal structure may not represent the true S0 helix under physiologic conditions. The TM regions of the monomer are relatively stable, indicating that the contacts between monomeric interfaces of the trimer are not necessary for protein stability. This is consistent with the experimental evidence that Hv1 can be readily expressed as a voltage-gated proton conducting monomer.

Throughout the trimer simulations, the VSD exhibits the overall 'closed umbrella' hydration pattern suggested in the initial crystal structure, i.e. the total number of waters hydrating each VSD converges towards ~150 with the majority of the waters present underneath the protein 'umbrella' in an intracellular cavity (Figure 3.1). The chimera monomer retains the same hydration pattern. By contrast, waters in the human Hv1 monomer simulation converge towards a more canonical VSD hour-glass distribution, with the number of waters on the intracellular side being roughly equal to the number of waters on the extracellular side (Figure 3.2). The center of the hour glass is formed by two points of constriction, an intracellular site located -5A below the center of the bilayer

and formed by R2 and D174 and an extracellular site located around 5A above the center of the bilayer and formed by the sidechains of R1, D112 and F150 (Figure 3.3). The only difference between the monomeric mHv1cc and the hHv1 system is sequence, emphasizing that hydration pattern and side chain location in VSDs is sequence dependent in proton-channel VSDs. A similar finding has been established in non-conducting VSDs.

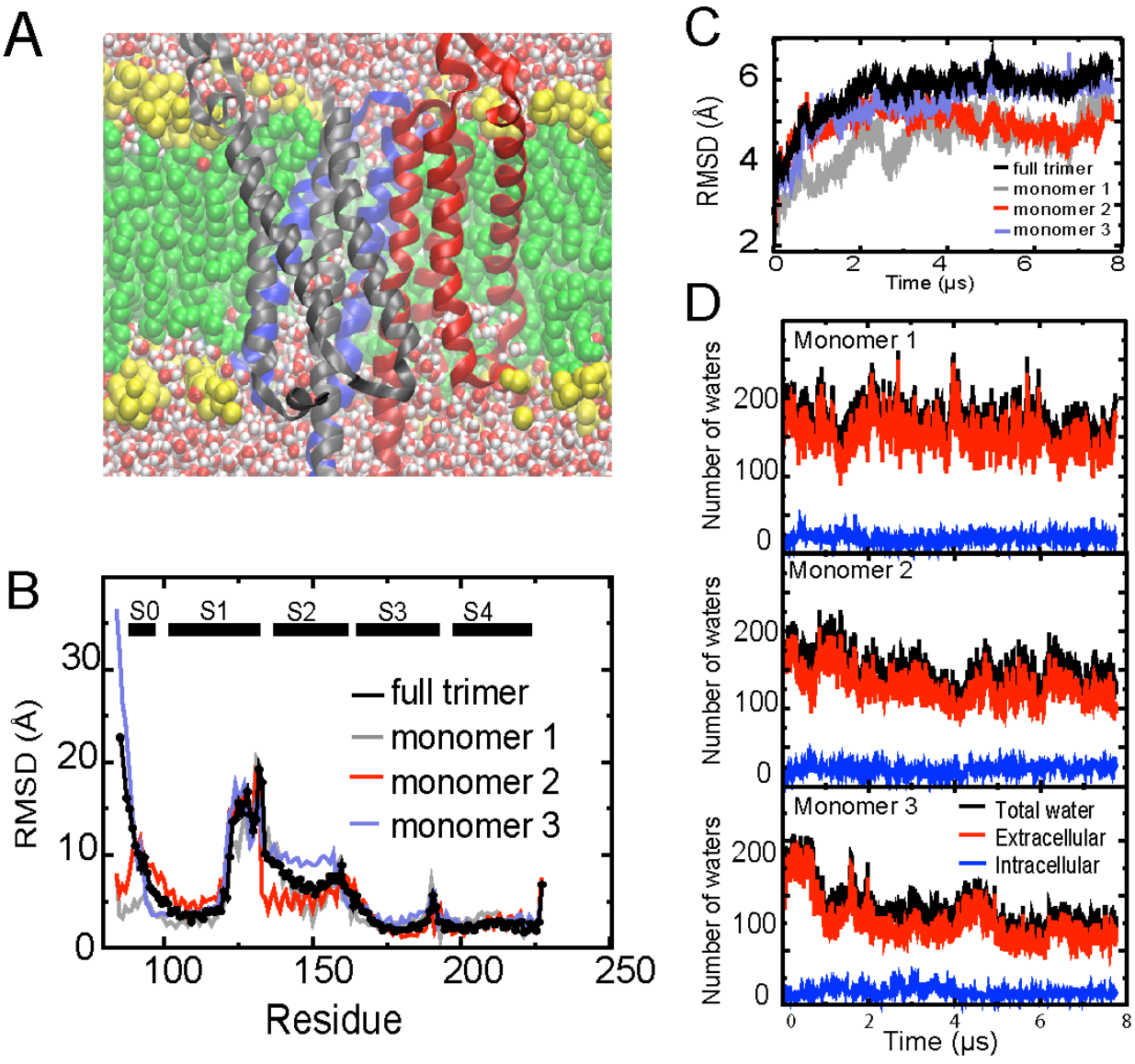

Figure 3.1. A. Snapshot of the mHv1cc trimer (Accession code: 3WKV) simulation

system. (B) Average RMSD for each residue's α-carbons, with respect to the initial crystal structure, calculated for the overall trimer structure and specific monomers. (C) RMSD for α- carbons in a specific monomer versus time. (D) Number of waters in the monomeric VSD versus time. The total number of waters within 5 Å of the VSD (black), the number of waters within the intracellular vestibule of the VSD (blue) and the number of waters within the extracellular vestibule of the VSD.

3.3.2 Microsecond simulations of the hHv1 model under transmembrane potential

Starting from the end of the simulation without potential, we applied a transmembrane potential equal to -140mV for ~10μs and a TM potential equal to +140mV for ~23μs. The starting configuration for the trajectory of hHv1 under potential was taken from the end of the simulation without applied potential. Experimental evidence and simulation data suggest that voltage-sensing in Hv1 is conferred via conserved S4 arginines and that the path taken by the S4 arginines overlaps with the proton permeation pathway. Mutagenesis of many key VSD lining residues (except D112) fail to abrogate proton current,(42) suggesting H+ conduction may partially involve the use of TM H-bonded water wires for conduction.

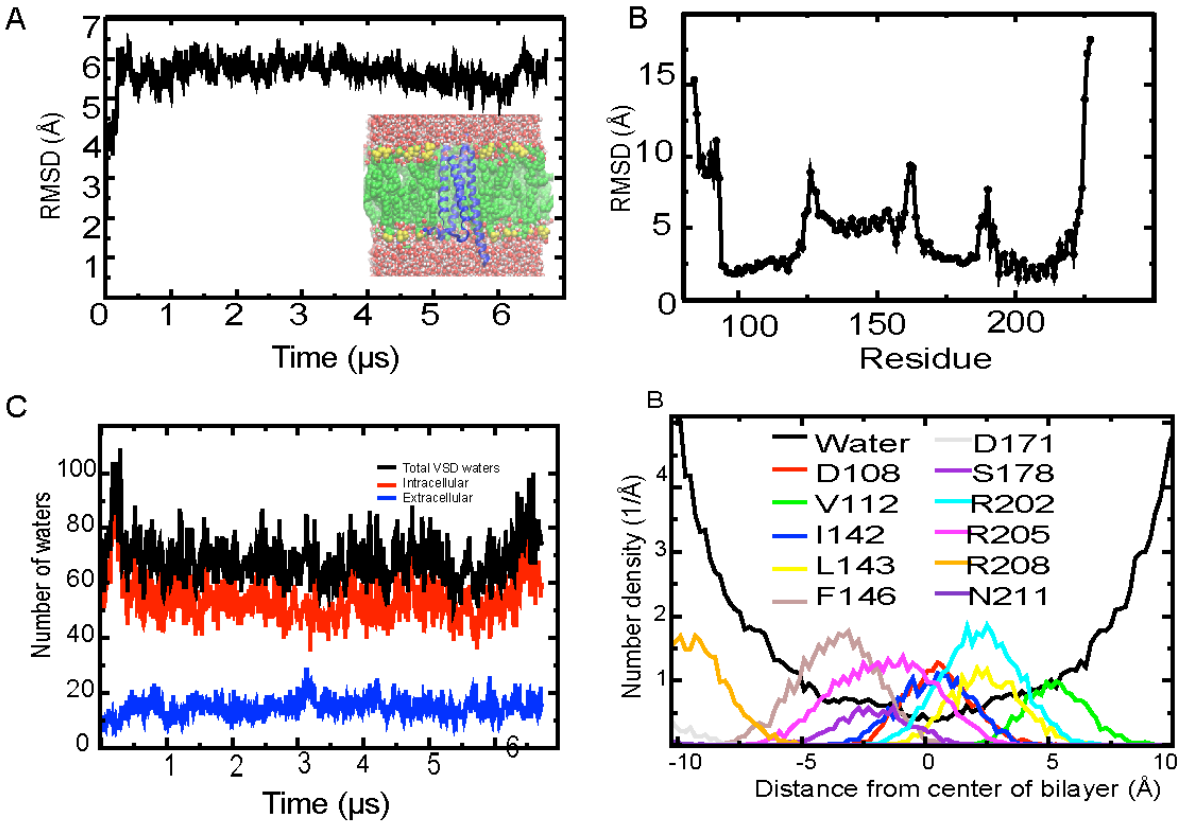

Figure 3.2. A. RMSD for α- carbons in the mHv1cc monomer versus time. (Inset-snapshot of the mHv1cc monomer simulation system. (B) Average RMSD for each residue's α-carbons, with respect to the initial crystal structure. (C) Number of waters in the monomeric VSD versus time. The total number of waters within 5 Å of the VSD (black), the number of waters within the intracellular vestibule of the VSD (blue) and the number of waters within the extracellular vestibule of the VSD. (D) Number densities for water and amino acids.

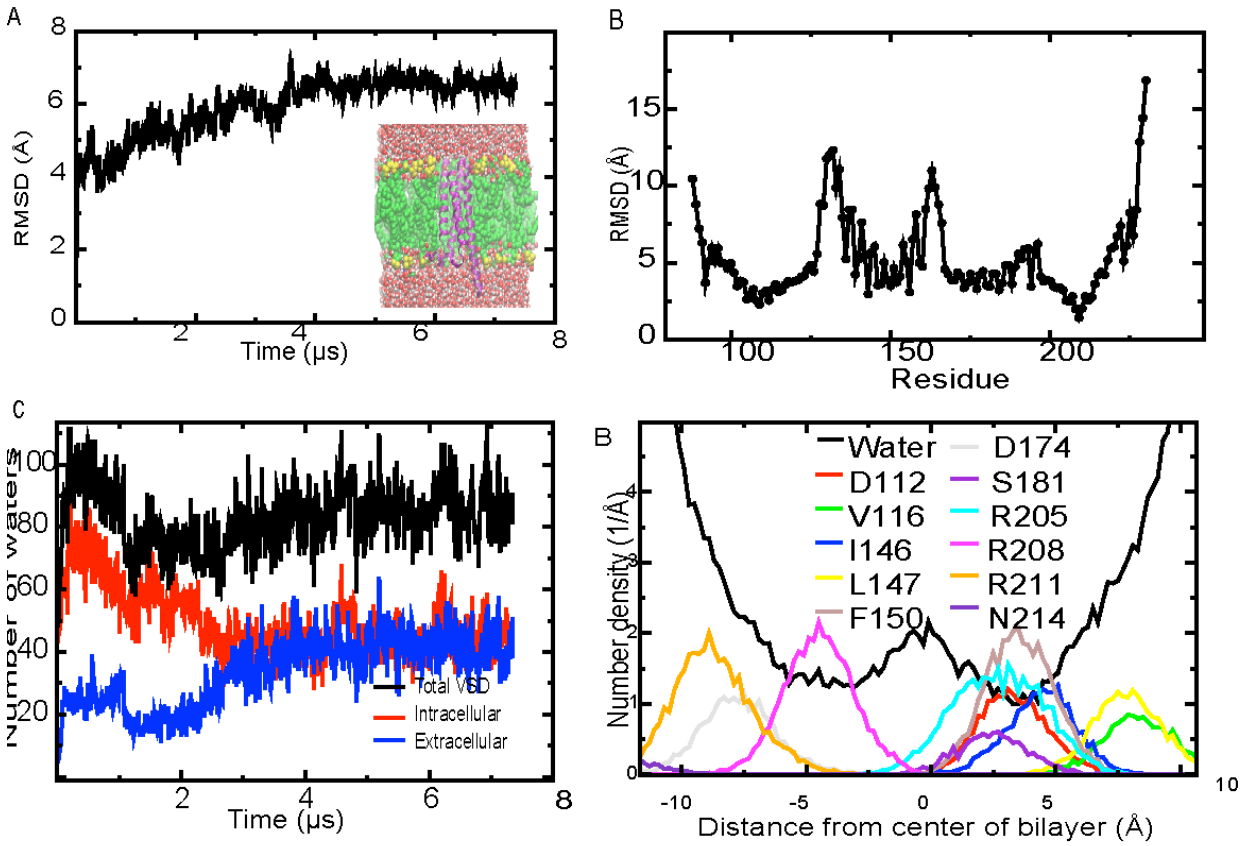

Figure 3.3. A. RMSD for α- carbons in the hHv1 monomer versus time. (Inset-snapshot of the hHv1cc monomer simulation system. (B) Average RMSD for each residue's α-carbons, with respect to the initial crystal structure. (C) Number of waters in the monomeric VSD versus time. The total number of waters within 5 Å of the VSD (black), the number of waters within the intracellular vestibule of the VSD (blue) and the number of waters within the extracellular vestibule of the VSD. Initially, the number of waters in the intracellular region are higher than the numbers of waters in the extracellular region, consistent with the notion of an 'open umbrella' where the intracellular vestibule is larger.(1) However, around 3μs, the number of intracellular waters decreases and extracellular increases. (D) Number densities for water and amino acids.

3.3.3 Kinetic stability of water wires through Hv1 model under an applied TM potential.

We previously reported that during hundreds of ns simulations without an applied transmembrane potential, our Hv1 model developed an open pathway occupied by

hydrogen-bonded water molecules through the center of the channel, supporting a possible Grotthuss hopping mechanism. A mixed Grotthuss mechanism, involving proton hopping along a hydrogen-bonded chain composed of water and titratable amino acids, has been proposed and supported by recent experimental and computational studies(42).

Here, we characterize hydrogen-bonded chains (HBCs) composed of water and/or a titratable side-chains connecting the intracellular and extracellular water-filled cavities of the VSD. We consider the occurrence of a TM HBC as a binary process (chain/no-chain), irrespective of the actual number of H-bonded configurations or the identity of the molecules. Block averaged time series for water only and water-protein HBCs under depolarizing potential are shown in panel G of figure 3.4. The HBC correlation times in Table 3.2 correspond to single-exponential fits to the binary process autocorrelation function and to the continuous time correlation function computed only over the configurations showing a HBC.

We find our model supports HBCs under both positive and negative potential, however, both pure water wires and mixed HBCs are supported more frequently and are longer lived at opening versus closing potential. Assuming Grotthuss hopping plays a role in Hv1 proton conduction, then the kinetics of the water wire formation and breaking in the mmHv1cc model are consistent with electrophysiological measurements of voltage dependent Hv1 channel opening and closing.

The inclusion of acidic residues in the hydrogen bonded chain analysis did not significantly change the lifetime or survival functions of the resultant HBCs, suggesting that no single amino acid is essential for a stable proton permeation pathway to form.

Conductance measurements in channels with D185 or D123 mutated to alanine reveal proton currents are not dependent upon any single titratable sidechain.

Table 3.2: Water wire kinetics

Selection included	**Binary Process (ns)**	**Survival Function (ns)**
Depolarized		
water	5715	3692
water or D112	5673	4181
water or D185	5735	3839
water or acidic	5676	4467
water or D119	5770	3391
water or D153	5747	3815
Hyperpolarized		
water	1087	1128
water or D112	1081	1228
water or D185	1089	1243
water or acidic	1440	1485
water or D119	1098	1128
water or D153	1336	1192
Unpolarized		
water	2785	1924
water or D112	3085	1923
water or D185	3219	1987
water or acidic	3406	1839
water or D119	2857	1928
water or D153	2845	1897

3.3.4 Water distribution and side-chain location change under potentials

We characterize water distribution and side-chain interactions in the hHv1 under an applied potential. At both opening and closing potentials, water number density profiles for the Hv1 model shows nonzero water density throughout the membrane (Left panel, Figure 3.5). The most constricted region differs in the down versus up state. In the most hyperpolarized 'down' state, the model retains an overall hour glass VSD hydration, with an extended region of low water density (number density of water < 1.5/A) extending for 10A (-5A above and below the center of the membrane). The region is flanked by two points of constriction. The intracellular constriction is composed of a salt-bridge between R208 and D174 while the extracellular is formed by R205 and E153. This configuration resembles the R2-Hv1 model proposed by Wood et al.(43) All S4 arginines sit intracellular to F150 and D112 in the membrane.

An applied opening potential causes reshaping of the water distribution, shortening the region of low water density. This appears to be caused by the arginines dragging a small amount of waters through the VSD as they up in the membrane, causing the intracellular site to become more hydrated. An extracellular constriction site remains, formed 5A above the center of the bilayer by a crowded arrangement composed of the R211-D185 salt-bridge and the hydrophobic cluster of V116 and I146. In our previous reports of R2-Hv1, this same highly conserved set of residues was identified to play a key role in shaping the constricted part of the putative permeation pathway.

In the open configuration, all three arginines are extracellular to F150 in the

membrane, with R1 and R2 clearly participating in salt-bridges with an extra-cellular set of acidic residues (D123 and E119). The sidechains of F150 and D112 sits near the most constricted extracellular site of the VSD throughout the simulations at both potential, and appear to be located at the same depth from the center of the membrane. Initially, both sidechains are 5A above the center of the membrane but become more intracellular in the open state.

3.3.5 Sequential salt-bridge pairing of the S4 arginines

Sequential pairing of S4 basic residues with neighboring VSD acidic residues is a well documented hallmark of voltage-induced conformational changes in Kv VSDSs. The translocation of the S4 arginines over the highly conserved S2 phenylalanine is mediated by several acidic residues in the S1-S3 helices, leading to S2 Phe and several acidic residues in S2 and S3 being termed the gating charge transfer center(44). As in non-conducting VSDs, we observe a sequential salt-bridge exchange involving a conserved set of acidic residues that can be characterized by a one-click mechanism. In the initial crystal structure configuration, R211 is salt bridged to D174, a residue homologous to 'D3' of the gating charge transfer center in Shaker described by Tao et al. R1 and R2 interact with D185 and D112, a universally conserved residue in Hv channels which helps confer channel selectivity for protons and does not have an associated homologous partner found in typical non-conducting Kv VSD sequences.

The S4 arginines, R1 and R2, move in a coupled fashion, taking similar sequential paths, salt-bridge hopping from the innermost acidic residues to outermost (112 to 185 to 119). However, R3 moves independently of R1 and R2. Instead of moving from intracellular to extracellular side chains, R211 brings the D185 sidechain intracellular to

sit at the same level as D112 in the bilayer. This configuration of R211 salt-bridged to D112 and D185 form the most constricted region of the VSD to maintain the hour-glass morphology.

Open state models proposed by Isacoff and Decoursey suggest interactions between R208 and D112 or R211 and D112, while the configuration of S4 arginines relative to D112 in a hyperpolarized state have not been directly probed until this study(45). Our models support an interaction between R3 and D112 in the activated state. Cysteine accessibility experiments reveal R2 is accessible from the intracellular side in the resting configuration and from the extracellular side when activated, suggesting that it moves through the whole membrane electric field. A histidine mutant at R3 is accessible to internally applied Zn2+ in the open state (46). Our simulations are consistent with these studies. In the most hyperpolarized configuration, R2 makes contact with intracellular phosphate headgroups and D174 while in the open-state, it interacts with E119 and E192, a residue found within the S3-S4 loop and at the level of the extracellular phosphate head groups. The third arginine remains accessible to the intracellular crevice in the open state as well. Recent mechanistic insights from Li et al. suggest at minimum, a one-click mechanism moving between the resting state and activated state, with a D112-R1-D185 triad becoming D112-R2-D185 in the activated state(47). Our data moves one-click beyond this, with the D112-R3-D185 triad favored in the most activated state. Our results support the notion that activation of the channel may involve all three arginines passing through the narrowest part of the VSD, interacting with D112 and translocating over both F150 and V116 to alter the putative water conductive pathway.

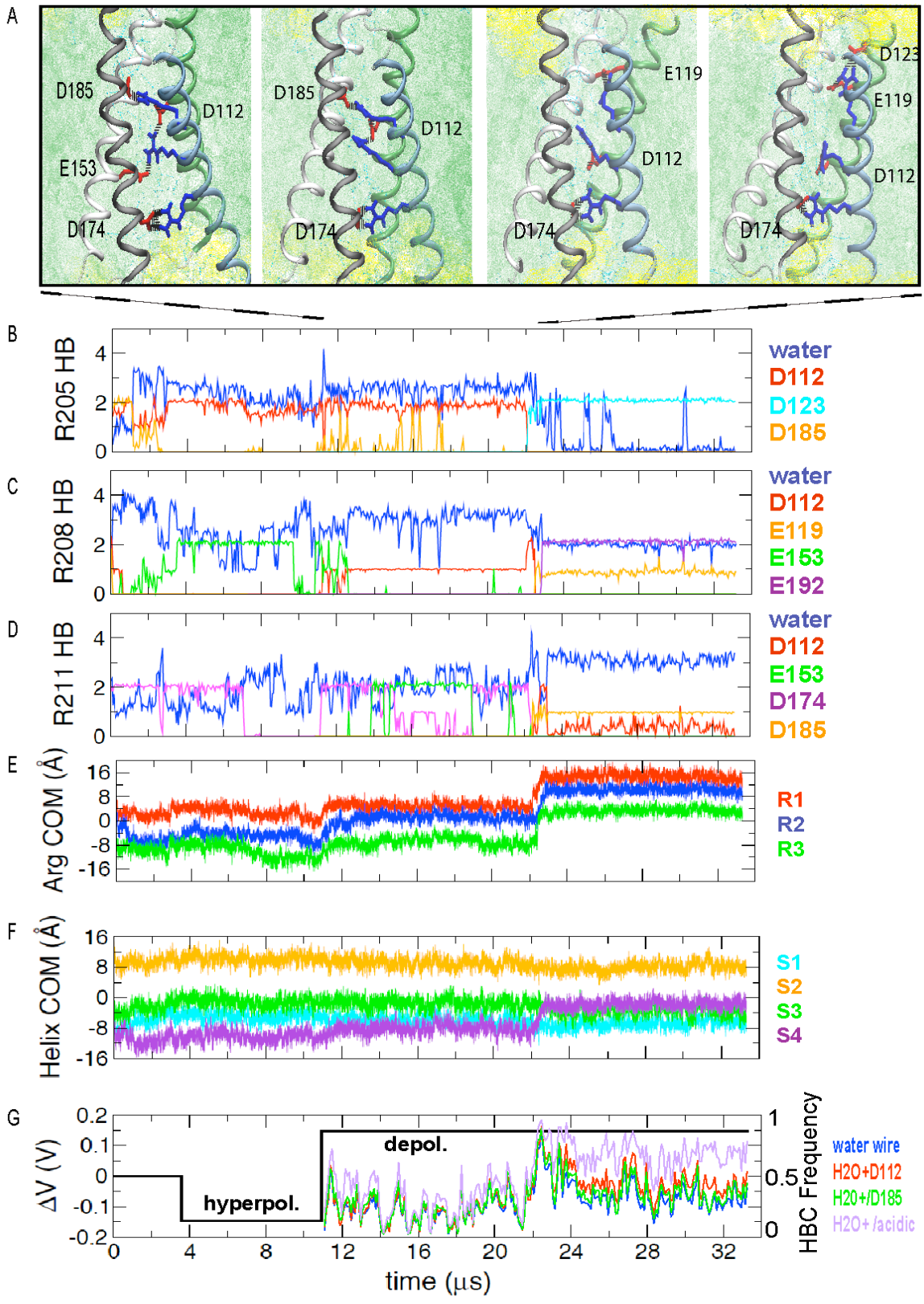

Figure 3.4. Motions of the S4 helix and hydrogen-bond chain analysis. (A)

Representative configurations of sequential salt-bridge pairs observed in the first 10 μs of simulation under a depolarizing potential. (B-D) H-bonds to the S4 arginines over time. E: Time evolution of the centers-of-mass of the voltage-sensing arginine residues in the S4 helix. F. Time evolution of the center-of-mass (relative to the bilayer center) of the S4 helix C_α atoms. (G) Transmembrane potential applied during a series of Anton simulations of hHv1 spanning ~33 μs (solid black line) and frequency of hydrogen-bond chain (HBC) formation in the depolarizing portion of the trajectory.

3.3.6 The hydrophobic sidechains of F150 and V116 mediate the one-click translocation

Numerous studies highlight the role of the highly conserved S2 phenylalanine in Kv VSD voltage-activation. Tao et al suggest that favorable sequential interactions between the highly conserved S2 phenylalanine (F290) and all of the S4 arginines take place during gating, while Lacroix and Bezanilla emphasize the importance of an interaction between F290 and the last S4 arginine.(48) In light of these studies, the motions of Hv1's third and last S4 arginine (R211) in relation to the analogous S2 phenylalanine (F150) are particularly relevant. In our studies, sequential interactions between all three S4 arginines and the phenylalanine take place during activation. Notably, in Hv1 a second hydrophobic residue, V116 appears to play a similar role to F290 by interacting sequentially with R1 and R2, which translocate past the hydrophobic side chain as they pass through the narrowest region of the VSD. However, the interaction between V116 and the last arginine appears to play an important role in the open state. The R3 sidechain is unable to translocate past V116, and appears to be locked into place between V116 and F150. These results are consistent with recent studies proposing V112 faces the proton permeation pathway (49).

3.3.7 Equipotential surface reshaping

Using linearized Poisson-Boltzmann theory and assuming a constant electrostatic potential difference across the membrane, we calculated electrostatic isopotential surfaces for the down and up VSD configurations. Examining the equipotential surfaces from the hyperpolarized trajectory, we find that the presence of F150 in close proximity to a R205-D112 salt-bridge results in a electrostatic focusing feature, in which the TM potential difference drops across a short distance at the center of the VSD cavities. A similar focusing feature has been described in simulation and experimental studies of Kv VSDs, highlighting the conserved nature of this hydrophobic gap(50, 51). Under opening/depolarized potentials that activate Kv channels, waters do not penetrate the central region of the VSD and the local electric field within the VSD remains focused near the S2 phenylalanine. This feature was predicted in previous simulations of homology models of mouse Hv1 (52). While the electric field is relatively unaltered during the voltage-activation process of non-conducing VSDs, we find at depolarized potentials that the equipotential surfaces in hHv1 are reshaped and become largely featureless near F150 when the pore is open. This reshaping was also observed using the Wood et al R2-Hv1 model after applying a depolarizing potential several hundreds of nanoseconds(53). In an N214R R2-Hv1 model, an extra Arg intracellular salt-bridge hinders reshaping under the same opening potential (unpublished data). These data taken together with experiments showing N214R is a non-conducting mutant, indicate the importance of an additional intracellular E2-S4 Arginine interaction in the voltage-activation process.

As the channel opens, a second focusing feature appears along the S1 helix in

the region of the hydrophobic sidechain of V116, a residue conserved in sequence position as either a valine or leucine across all proton channels. The corresponding position in non-conducting Kv VSDs is conserved as a Phe. In hHv1 voltage-induced activation, the V116 residue appears to play a similar role as F150 in helping to focus the field, facilitating S4 arginine translocation across a greater proportion of the field in a shorter TM distance. In combination with the sidechains of E119 and D112, V116 may form a secondary specialized ‘gating-charge transfer center’ unique to proton channels.

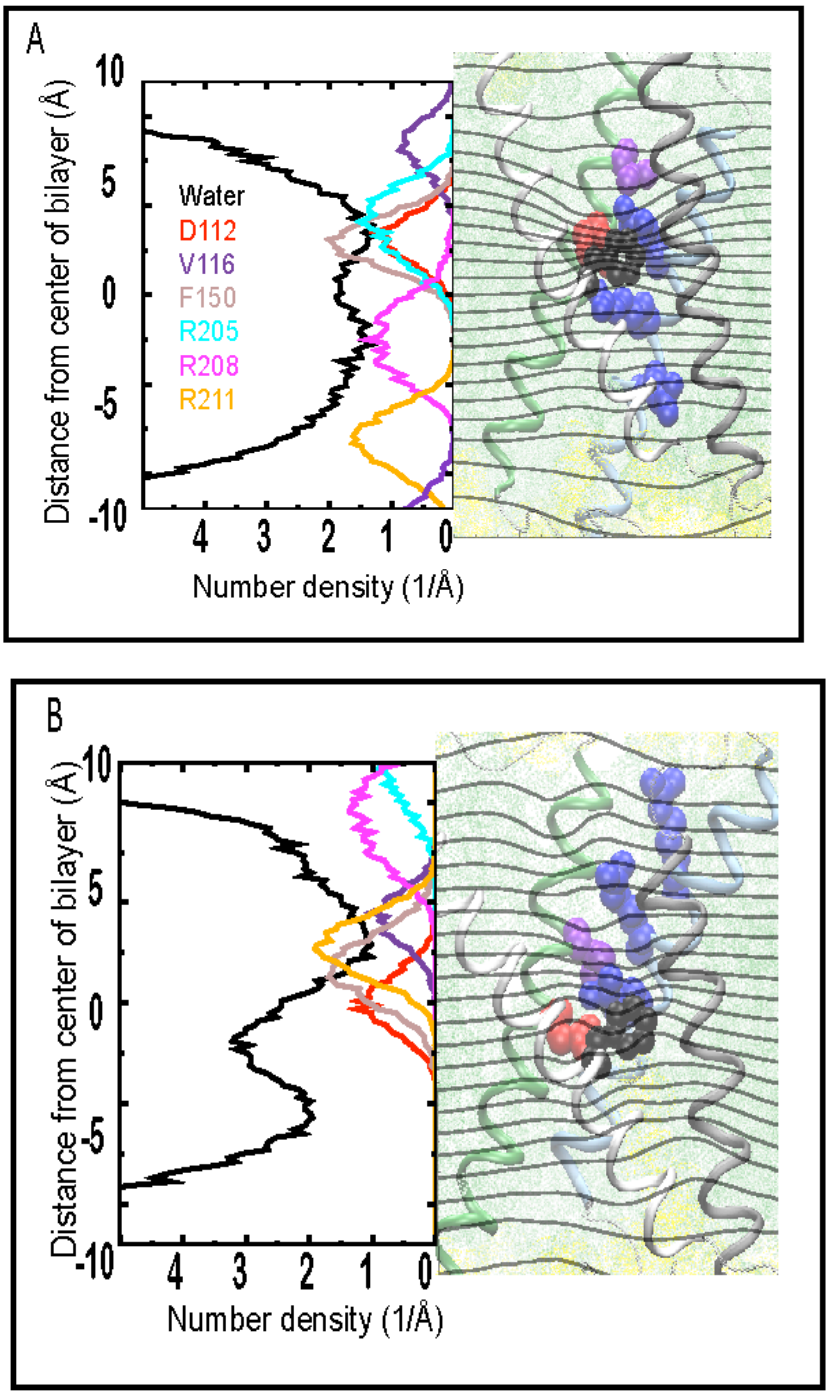

Figure 3.5. Equipotential surfaces reveal a focusing feature similar to that observed in non-conducting VSDs in the down-state (A). An applied depolarizing potential reveals a secondary focusing feature near V116 centered on the S1 helix (B) of the human Hv1 monomer in the up-state. Proteins are shown in ribbon representation and colored by segment. Lipid tails (green), head groups (yellow) and water (oxygen red, hydrogen white) are in van der Waals representation.

3.3.8 Motions of the S4 helix suggest a sliding-helix model of voltage-activation and recapitulate gating charge measurements

The motion of the S4 helix has been well studied in nonconducting VSDs, leading to several models being proposed. However the sliding-helix model has taken precedence in the literature. In our simulations, we observe an 8Å translocation of the S4 helix that is unaccompanied by changes in the center of mass of the other TM helices, consistent with a sliding-helix model, (Figure 3.4). Gonzalez et al. characterize a two-step motion of the S4 under voltage that involves cooperative gating between monomers, however the initial S4 movement occurs independently in the two subunits(54). Our data supports the notion that movement of S4, facilitated through intra-VSD salt bridge exchange, occurs independently in each subunit. In initial studies of an open-state model generated prior to publication of the crystal structure using targeted MD, Chamberlin et al. did not observe a rigid-body movement of an entire helical bundle, but rather a sequential rearrangement: the gating transition from closed to open is achieved by a translocation of S4 by ~10–12 Å, followed by a coupled rotation of the paddle-motif (S3–S4) relative to S1–S2(55). We note a translocation of S4 by 8A without significant rotation of the S3 and S4 motif.

Using the limiting slope method, the number of charges displaced relative to the TM electric field during channel activation was determined to be 5.9e for the dimer (54) and 2.7e for the monomer. Neutralization of individual arginines reduced charge displacement by about 1e and 2e in the monomeric and dimeric channels. We calculated gating charge

movement between the open and closed state using ensemble of 800 configurations taken at even intervals from the hyperpolarizing and depolarizing portion of the simulations. In good agreement with experimental measures, we find the computed gating charge from simulation is 2.5 *e,* with the largest contributions from the movement of the three arginines.

3.3.9 Docking of 2-GBI to the open state

The organic ligand 2-guanidinobenzimidazole (2-GBI) has been shown to inhibit proton conduction within Hv1 (4, 5) by binding within the intracellular side of the selectivity filter region of the channel in the open state. Mutant-cycle analysis of this binding event places the aromatic ring of the benzimidazole moiety of 2-GBI near F150's side chain and the basic guanidine group next to D112.

We performed docking studies of the 2-GBI ligand within our equilibrated closed and open state models (Figure 3.6) using AutoDock Vina (37). The four residues chosen to represent the selectivity filter were D112, F150, S181 and either R1 for closed-state or R3 for open-state. The configurations of these residues were clustered based on the root-mean squared deviation (RMSD) being less than 1 Å. The twenty most probable configurations for each state were used to perform the docking calculations. The resulting 2-GBI configurations were also clustered based on RMSD (with respect to?) with the most probable configurations selected. The open-state model showed favorable binding of 2-GBI with the aromatic group next to F150 and the guanidine group pointed between D112 and R211 (Fig 3A). The ligand is positioned directly below the selectivity filter and effectively blocks the formation of a hydrogen bonded water wire through the open channel via steric hindrance.

A similar docking calculation on the closed-state of Hv1 shows that the orientation of the selected residues does not allow the 2-GBI to choose a favorable binding conformation near the selectivity filter. The two most probable configurations of the ligand place it pointing parallel to the channel with the aromatic group located in the solution of the intracellular vestibule of the channel and the guanidine group pointing towards the selectivity filter, primarily D112 (Figure 3.6). Our docking poses recapitulate experimentally predicted GBI-protein interactions between the sidechains of F150, R211 and the benzimidizole and guanidinium groups of the drug, providing additional validation for our open state model.

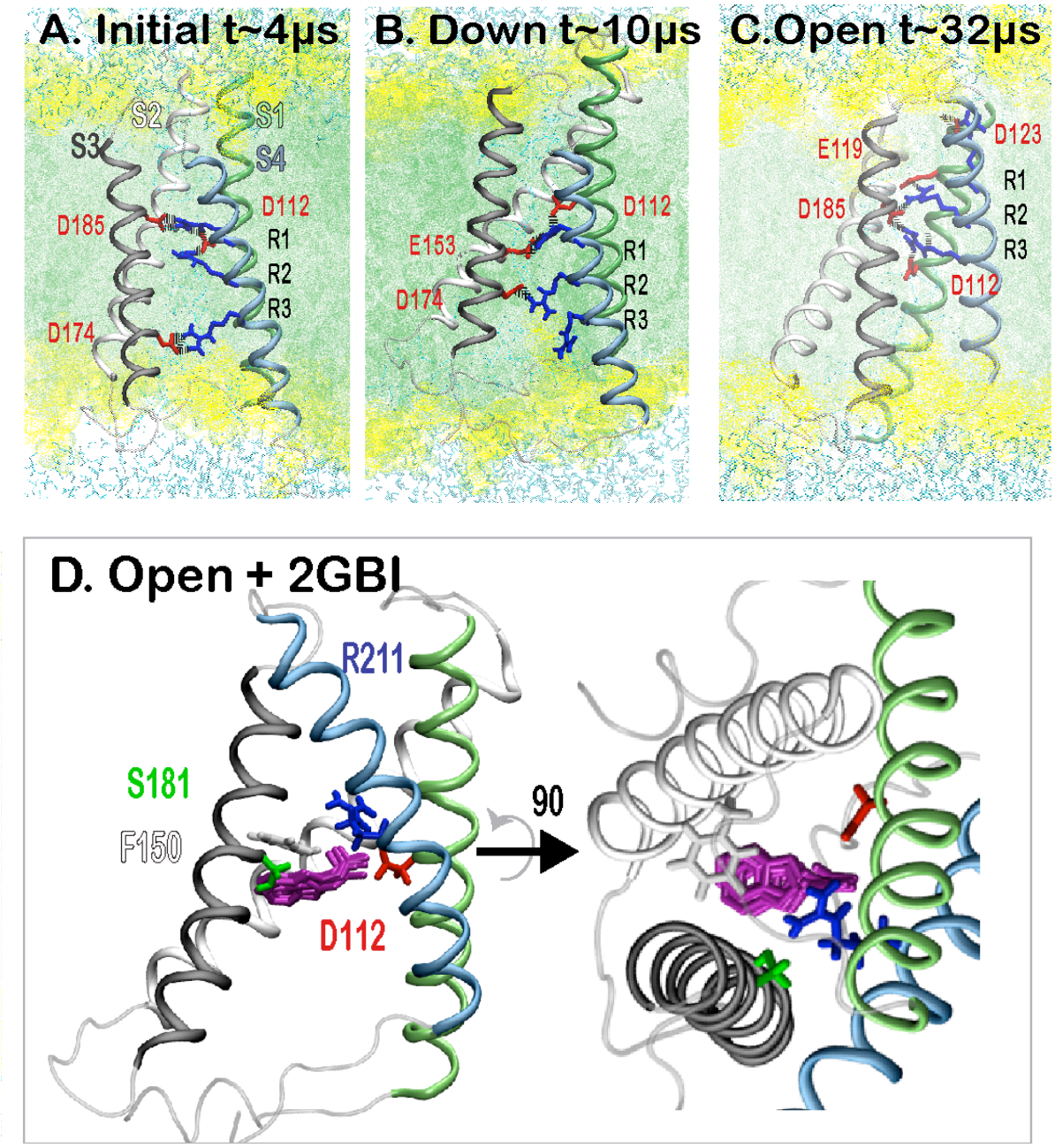

Figure 3.6. Configurations of hHv1 with internal salt-bridges depicted. A. Equilibrated structure of the resting state in the absence of a transmembrane electric field, B. under hyperpolarized potential (–140 mV), C. under depolarized potential (+140 mV). S4 (in blue) is seen to be in the "up state" in the depolarizing potential (panel C), with R3 interacting with D112 to form the selectivity filter. The protein backbone is shown in the ribbon representation colored corresponding to the VSD helix segment (S1-S4). Selected residues are colored by type (blue are basic, red are acidic). D. Two-views (transmembrane and extracellular) of docking results for 2-guanidinobenzimidazole (2-GBI) into the intracellular side of the open state. We observe interactions between the guanidinium group and the selectivity filter region, including D112, R211, S181. The 2-

GBI sits at the selectivity filter with the benzyl ring stacks near F150 and the guanidine group pointing towards R211.

3.4 Concluding remarks

Before the structure of a voltage-gated H^+ channel was solved in 2014,(1) our understanding of the atomistic details of Hv1 dynamics was limited primarily by the lack of a high-resolution structure. This led several groups, including ours, to construct different Hv1 homology models using structures of VSDs from voltage-gated ion channels (VGICs) as templates(46, 52, 56). A comprehensive review of the modeling techniques and their comparison to the crystal structure has been reported by Pupo et al.(57) Our final depolarized configuration is most similar to the R3D model proposed by Berger and Isacoff(45). We have presented the first microsecond simulations of the crystal structure construct and an Hv1 homology model based on the structure. We find both the trimer and monomeric structures of the crystal structure, embedded in a lipid bilayer, are stable on the microsecond timescale.

This study offers the first analysis of unbiased simulations of the hHv1 channel under physiologically relevant TM potentials. Previous attempts to shed light on the atomistic details of proton channel voltage-gating relied on the application of an applied force along the RMSD between a down and up homology model, using a method called targeted MD (TMD)(55). TMD offers limited insight into the interactions during gating because of the application of a constant force along an artificial reaction coordinate. Our unrestrained simulations not only recapitulate experimental gating charge measurements, but allow for insights to be made about the atomistic motions, e.g. movement of the S4 helix and salt-bridge rearrangements, connecting the initial and

final structures. Our open-state model taken from the final depolarized configuration recapitulates experimentally derived small molecule-protein interactions and reveals the first insights into the voltage-activation process, including details about electric field reshaping and the atomistic interactions underlying electrophysiological and biochemical experimental observations.

3.5 References

1. Takeshita K*, et al.* (X-ray crystal structure of voltage-gated proton channel. *Nat Struct Mol Biol* 21(4):352-357.
2. DeCoursey TE (2013) Voltage-gated proton channels: molecular biology, physiology, and pathophysiology of the H(V) family. *Physiol Rev* 93(2):599-652.
3. Wang Y, Li SJ, Wu X, Che Y, & Li Q (2012) Clinicopathological and Biological Significance of Human Voltage-gated Proton Channel Hv1 Protein Overexpression in Breast Cancer. *J Biol Chem* 287(17):13877-13888.
4. Hong L, Kim IH, & Tombola F (2014) Molecular determinants of Hv1 proton channel inhibition by guanidine derivatives. *Proc Natl Acad Sci U S A* 111(27):9971-9976.
5. Hong L, Pathak MM, Kim IH, Ta D, & Tombola F (2013) Voltage-sensing domain of voltage-gated proton channel Hv1 shares mechanism of block with pore domains. *Neuron* 77(2):274-287.
6. O'Connor PM, Guha A, Stilphen CA, Sun J, & Jin C (2016) Proton channels and renal hypertensive injury: a key piece of the Dahl salt-sensitive rat puzzle? *American journal of physiology. Regulatory, integrative and comparative physiology* 310(8):R679-690.
7. Ramsey SI, Ruchti E, Kaczmarek JS, & Clapham DE (2009) Hv1 proton channels are required for high-level NADPH oxidase-dependent superoxide production during the phagocyte respiratory burst. *Proc. Natl. Acad. Sci. U.S.A.* 106:7642-7647.

8. Musset B*, et al.* (2008) Detailed comparison of expressed and native voltage-gated proton channel currents. *J Physiol* 586(10):2477-2486.

9. Hondares E*, et al.* (2014) Enhanced activation of an amino-terminally truncated isoform of the voltage-gated proton channel HVCN1 enriched in malignant B cells. *Proc Natl Acad Sci U S A* 111(50):18078-18083.

10. Capasso M*, et al.* (2010) HVCN1 modulates BCR signal strength via regulation of BCR-dependent generation of reactive oxygen species. *Nat Immunol* 11(3):265-272.

11. Liu J*, et al.* (2015) Microglial Hv1 proton channel promotes cuprizone-induced demyelination through oxidative damage. *J Neurochem* 135(2):347-356.

12. Wang Y, Wu X, Li Q, Zhang S, & Li SJ (2013) Human voltage-gated proton channel hv1: a new potential biomarker for diagnosis and prognosis of colorectal cancer. *PLoS One* 8(8):e70550.

13. Wang Y, Zhang S, & Li SJ (2013) Zn(2+) induces apoptosis in human highly metastatic SHG-44 glioma cells, through inhibiting activity of the voltage-gated proton channel Hv1. *Biochem Biophys Res Commun* 438(2):312-317.

14. Wu LJ*, et al.* (2012) The voltage-gated proton channel Hv1 enhances brain damage from ischemic stroke. *Nat Neurosci* 15(4):565-573.

15. Seredenina T, Demaurex N, & Krause KH (2015) Voltage-Gated Proton Channels as Novel Drug Targets: From NADPH Oxidase Regulation to Sperm Biology. *Antioxidants & redox signaling* 23(5):490-513.

16. Hong L, Singh V, Wulff H, & Tombola F (2015) Interrogation of the intersubunit interface of the open Hv1 proton channel with a probe of allosteric coupling. *Scientific reports* 5:14077.

17. Tombola F, Ulbrich MH, & Isacoff EY (2008) The voltage-gated proton channel Hv1 has two pores, each controlled by one voltage sensor. *Neuron* 58:546-556.

18. Ida M*, et al.* (2008) An investigation of magnetic resonance imaging features in 14 patients with synovial chondromatosis of the temporomandibular joint. *Dento maxillo facial radiology* 37(4):213-219.

19. Swartz KJ (2008) Sensing voltage across lipid membranes. *Nature* 456:891-897.

20. Aggarwal SK & MacKinnon R (1996) Contribution of the S4 segment to gating charge in the *Shaker* K^+ channel. *Neuron* 16:1169-1177.

21. Ruta V, Jiang YX, Lee A, Chen JY, & MacKinnon R (2003) Functional analysis of an archaebacterial voltage-dependent K^+ channel. *Nature* 422:180-185.

22. Schoppa NE, McCormack K, Tanouye MA, & Sigworth FJ (1992) The size of gating charge in wild-type and mutant *Shaker* potassium channels. *Science* 255:1712-1715.

23. Seoh SA, Sigg D, Papazian DM, & Bezanilla F (1996) Voltage-sensing residues in the S2 and S4 segments of the Shaker K^+ channel. *Neuron* 16(6):1159-1167.

24. Sasaki M, Takagi M, & Okamura Y (2006) A voltage-sensor domain protein is a voltage-gated proton channel. *Science* 312:589-592.

25. Ramsey IS, Moran MM, Chong JA, & Clapham DE (2006) A voltage-gated proton-selective channel lacking the pore domain. *Nature* 440:1213-1216.

26. Gonzalez-Perez LM, Congregado-Cordoba J, & Salinas-Martin MV (2011) Temporomandibular joint synovial chondromatosis with a traumatic etiology. *International journal of oral and maxillofacial surgery* 40(3):330-334.

27. Tombola F, Ulbrich MH, Kohout SC, & E.Y. I (2010) The opening of the two pores of the Hv1 voltage-gated proton channel is tuned by cooperativity. *Nature Structural and Molecular Biology* 17:44-50.

28. Larsson B, Baker OS, Dhillon DS, & Isacoff EY (1996) Transmembrane movement of the *Shaker* K+ channel S4. *Neuron* 16:387-397.

29. Glauner KS, Mannuzzu LM, Gandhi CS, & Isacoff EY (1999) Spectroscopic mapping of voltage sensor movement in the *Shaker* potassium channel. *Nature* 402(6763):813-817.

30. Ruta V, Chen J, & MacKinnon R (2005) Calibrated measurement of gating-charge arginine. *Cell* 123:463-475.

31. Pathak MM*, et al.* (2007) Closing in on the resting state of the Shaker K^+ channel. *Neuron* 56:124-140.

32. Alabi AR, Bahamonde MI, Jung HJ, Kin JI, & Swartz KJ (2007) Portability of paddle motif function and pharmacology in voltage sensors. *Nature* 450:370-376.

33. Kelley LA, Mezulis S, Yates CM, Wass MN, & Sternberg MJ (2015) The Phyre2 web portal for protein modeling, prediction and analysis. *Nature protocols* 10(6):845-858.

34. Freites JA, Schow EV, White SH, & Tobias DJ (2012) Microscopic origin of gating current fluctuations in a potassium channel voltage sensor. *Biophys. J.* 102(11):L44-L46.

35. Shan Y, Klepeis JL, Eastwood MP, Dror RO, & Shaw DE (2005) Gaussian split Ewald: a fast Ewald mesh method for molecular simulation. *J. Chem. Phys.* 122:054101-054101 to 054101-054113.

36. Martyna GJ, Tobias DJ, & Klein ML (1994) Constant-pressure molecular-dynamics algorithms. *J. Chem. Phys.* 101:4177-4189.

37. Trott O & Olson AJ (2010) AutoDock Vina: improving the speed and accuracy of docking with a new scoring function, efficient optimization, and multithreading. *J Comput Chem* 31(2):455-461.

38. Humphrey W, Dalke W, & Schulten K (1996) VMD: Visual molecular dynamics. *J. Mol. Graph.* 14(1):33-38.

39. Takeshita K*, et al.* (2014) X-ray crystal structure of voltage-gated proton channel. *Nat Struct Mol Biol* 21(4):352-357.

40. Musset B*, et al.* (2010) Oligomerization of the voltage-gated proton channel. *Channels* 4:260-265.

41. Mony L, Berger TK, & Isacoff EY (2015) A specialized molecular motion opens the Hv1 voltage-gated proton channel. *Nat Struct Mol Biol* 22(4):283-290.

42. Musset B*, et al.* (Aspartate 112 is the selectivity filter of the human voltage-gated proton channel. *Nature* 480(7376):273-277.

43. Wood ML*, et al.* (2012) Water wires in atomistic models of the Hv1 proton channel. *Biochim. Biophys. Acta* 1818:286-293.

44. Tao X, Lee A, Limapichat W, Dougherty DA, & MacKinnon R (2010) A gating charge transfer center in voltage sensors. *Science* 328:67-73.

45. Berger TK & Isacoff EY (2011) The pore of the voltage-gated proton channel. *Neuron* 72(6):991-1000.

46. Kulleperuma K*, et al.* (Construction and validation of a homology model of the human voltage-gated proton channel hHV1. *J Gen Physiol* 141(4):445-465.

47. Li Q*, et al.* (2015) Resting state of the human proton channel dimer in a lipid bilayer. *Proc Natl Acad Sci U S A* 112(44):E5926-5935.

48. Lacroix JJ & Bezanilla F (2011) Control of a final gating charge transition by a hydrophobic residue in the S2 segment of a K^+ channel voltage sensor. *Proc. Natl. Acad. Sci. U.S.A.* 108:6444-6449.

49. Morgan D*, et al.* (2013) Peregrination of the selectivity filter delineates the pore of the human voltage-gated proton channel hHV1. *J Gen Physiol* 142(6):625-640.

50. Yarov-Yarovoy V*, et al.* (2012) Structural basis for gating charge movement in the voltage sensor of a sodium channel. *Proc Natl Acad Sci U S A* 109(2):E93-102.

51. Freites JA & Tobias DJ (2015) Voltage Sensing in Membranes: From Macroscopic Currents to Molecular Motions. *The Journal of membrane biology* 248(3):419-430.

52. Chamberlin A*, et al.* (Hydrophobic plug functions as a gate in voltage-gated proton channels. *Proc Natl Acad Sci U S A* 111(2):E273-282.

53. Wood ML*, et al.* (Water wires in atomistic models of the Hv1 proton channel. *Biochim Biophys Acta* 1818(2):286-293.

54. Gonzalez C, Koch HP, Drum BM, & Larsson HP (2010) Strong cooperativity between subunits in voltage-gated proton channels. *Nature Struct. Mol. Biol.* 17:51-56.

55. Chamberlin A, Qiu F, Wang Y, Noskov SY, & Larsson HP (2015) Mapping the gating and permeation pathways in the voltage-gated proton channel Hv1. *J Mol Biol* 427(1):131-145.

56. Ramsey IS*, et al.* (2010) An aqueous H^+ permeation pathway in the voltage-gated proton channel Hv1. *Nature Structural and Molecular Biology*:1-7.

57. Pupo A, Baez-Nieto D, Martinez A, Latorre R, & Gonzalez C (Proton channel models: Filling the gap between experimental data and the structural rationale. *Channels (Austin)* 8(3).

Chapter 4

Atomistic modeling of ion conduction through voltage-sensing domains

4.1 Introduction

Voltage-sensing domains (VSDs) are modular membrane protein units that sense changes in the membrane electrostatic potential, and through conformational changes, regulate a specific function. The VSDs of voltage-dependent K^+, Na^+ and Ca^{2+} channels do not conduct ions under physiological conditions, but they can become ion-permeable under pathological conditions through mutations in the voltage sensor, particularly of S4 basic side chains. Relatively little is known about the underlying mechanisms of conduction through VSDs. The most detailed studies have been performed on *Shaker*

K^+ channel variants that include the mutation of the outermost Arg residue in S4 to a smaller, uncharged side chain[1,2]. Ion conduction through the *Shaker* VSD is manifested in electrophysiology experiments as a separate voltage-dependent inward current that appears when the VSDs are in their resting state conformation[1]. Only monovalent cations permeate the *Shaker* VSD through a narrow and twisted pathway after reaching a vestibular region on the extracellular side of the VSD[1,2]. This permeation pathway is, at least in part, the same as that one followed by the S4 basic side chains during voltage-dependent activation. We sampled VSD ion conduction events on the μs timescale under a membrane potential using experimentally validated models of the *Shaker* VSD[3] in a resting state in order to shed light on the molecular mechanisms of ion conduction, gating, and selectivity.

Voltage-gated ion channels (VGICs) open and close in response to changes in the membrane potential and are typically associated with impulse generation and propagation in excitable cells. A typical VGIC channel is a tetramer and each subunit is composed of 6 transmembrane segments (termed S1-S6). Segments S5-S6 from all four subunits contribute to the formation of the pore domain, which contains the ion conduction pathway and the activation gate (1), (2). Segments S1 to S4 make up the voltage-sensing domain (VSD). In Kv channels, pore opening and closing is controlled (gated) by movement of the VSDs, which are highly sensitive to changes in TM potential. Voltage sensitivity in VSDs is conferred by a series of highly conserved positions for charged residues, which move through the membrane in response to changes in transmembrane potential and are known as gating charges. In particular, the S4 segment contains a highly conserved region of several triplet repeats composed of a

basic side chain (mostly arginine) followed by two hydrophobic residues. In the case of the *Shaker* voltage-gated K^+ channel, it has been shown that the first four arginines in S4 (termed R1 through R4) contribute most of the gating charge during activation

The voltage-sensing domains (VSDs) of VGICs are modular membrane protein units sense changes in the membrane electrostatic potential, and through voltage-induced conformational changes, regulate a variety of processes in the cell. In addition to the K+ VGICs, the superfamily of membrane proteins that contain VSDs, includes voltage-dependent Na^+ and Ca^{2+} channels (Kv, Nav, and Cav, respectively) (3), the voltage-dependent proton channel Hv (4),(5) and voltage-sensitive phosphatases (6) (7) These voltage-dependent ion channels play key roles in the generation and propagation of electrical impulses in excitable cells), the activation and proliferation of immune cells (8), and the proliferation and motility of cancer cells.

The VSDs of Kv, Nav, and Cav channels do not conduct ions under physiological conditions, but they can become ion-permeable through mutations in the voltage sensor, particularly of S4 basic side chains (9), (10). VSD conduction in Nav1.4 channel mutants has been found to be the cause of some hypokalemic and normokalemic periodic paralyses(10-15). Mutations of the S4 basic side chains in other voltage-dependent ion channels are associated with a number of genetic diseases, thus it is possible that VSD conduction may play a central role in their pathophysiology (12), (16). Cation conduction through separate, selective, pore domains in voltage-dependent ion channels is reasonably well understood at the molecular level (17).

In contrast, relatively little is known about the underlying mechanisms of conduction through VSDs. The available experimental evidence on Shaker K+ channel mutants suggests that ions permeating through the VSD follow, at least in part, the same pathway as S4 basic side chains during voltage-dependent activation (29,39,40). The selective VSD cation conduction occurs at a closing/hyperpolarizing (negative on the inside) potential. The lack of a high resolution closed state for the Shaker channel previously limited our ability to understand conduction through VSDs, however recent electrophysiology recordings of Cd^{2+}-bridged double cysteine mutants of *Shaker* enabled Henrion et al.. to generate a subset of the experimental constraints, which were used to generate Rosetta models of the conformations that were subjected to molecular simulation and tested against the remaining constraints. They present coordinates for five Shaker conformations (Open, “O”; Closed 1, “C1”; Closed 2, “C2”; Closed 3, “C3”; Closed 4, “C4”), informed by experiment and homology modeling using the Kv1.2-2.1 paddle chimera as a template. They predict the Shaker K channel goes through at least the C1-C2-C3 sequence of conformations during closing, and, in some cases, it appears to be possible to capture the VSD in a C4 conformation.

We used the C3 coordinates to create a quadruple mutant (R362S/E283D/S357C/M356D) of the Shaker VSD, termed the big omega-current mutant (BOM). Because omega conductance of the single point mutant R362S (R1S) was small, Tombola et al.. considered 18 additional manipulations that increased omega current and found that the addition of the three mutations (E283D/S357C/M356D) increased the omega current 13-fold, hence the term big

omega-current mutant. The single-channel conductance of the BOM omega pore was 3.42±0.12 pS and the open probability (at -250mV) was 0.53±0.02 (*n*=9).

The expected rate of ion turnover events during a single atomistic simulation, n_ω, can be estimated from experimental measurement as

$$n_\omega = \frac{P_g \gamma_\omega V}{e}$$

where γ_ω and P_g are, respectively, the conductance and open probability of a single VSD, and *V* is the applied potential. In the BOM mutant the corresponding values were reported as γ_ω = 3.42 ± 0.12 pS and P_g = 0.53 ± 0.02 at -250 mV, which would result n_ω ~2.84 ions/μs. Because these values correspond to K+ conduction, they can be interpreted as a lower bound to our simulations in guanidinium chloride. At -250 mV, guanidinium ion VSD currents have been found to be three times larger than K+ currents in the R1C Shaker mutant, assuming that this ratio is also valid for the BOM mutant, an upper bound for the rate of ion turnover events in a single simulation trajectory is n_ω ~8.52 ions/μs.

We performed atomistic MD simulations on the 10-**μ**s timescale to directly model VSD cation conduction events through the BOM. We observe and describe cation permeation for two cations, K+ and Gdm+ under a range of applied voltages. The structural and mechanistic insight from simulations, combined with the growing literature of therapeutic ion channel modulation, could one day lead to the development of novel small molecule drugs targeting voltage-sensing domains.

4.2 Methods

4.2.1 C3 state VSD system setup and equilibration

The wild-type C3 state Shaker VSD configuration from Henrion et al.. was used for initial protein coordinates. The simulation system was composed of one Shaker VSD (residues 225–379), 180 1-palmytoyl-2-oleoyl-sn-glycero-3-phosphatidylcholine (POPC) molecules (90 per leaflet) fully hydrated in 150 mM KCl for a total of 51,294 atoms. We used CHARMM-GUI (18) to assemble the membranes and waters. Before being transferred to Anton, MD runs were performed with NAMD 2.9. The system was equilibrated for several ns by means of a restrained all-atom MD simulation followed by a several ns unrestrained simulation as described in the multistage equilibration procedure.

4.2.2 Multistage equilibration procedure

After 5000 steps of minimization with all protein atoms constrained, we ran the wild-type C3 system for 100ps in the constant temperature (T=300K), constant volume (NVT) ensemble, allowing the lipid molecules to relax. The system was then equilibrated for several ns in the NPT ensemble (P_n=1atm T=300K) with the protein backbone atoms restrained harmonically to their initial positions and slowly released over 10ns using a decreasing force constant equal to 50kcal $mol^{-1}Å^{-1}$, 25kcal $mol^{-1}Å^{-1}$, 10kcal $mol^{-1}Å^{-1}$, 5kcal $mol^{-1}Å^{-1}$, and 2kcal $mol^{-1}Å^{-1}$. After the backbone was completely released, we ran the system several nanoseconds without an applied bias, followed by several ns with an applied voltage.

4.2.3 NAMD 2.9 simulation details

The equilibration simulations were performed with NAMD2.9 (19). CHARMM27 and CHARMM36 force fields (20, 21)} were used for the protein and lipids, respectively, and the TIP3P model was used for water (22). The smooth particle mesh Ewald method ((23) and (24)) was used to calculate electrostatic interactions, and the short-range, real-space interactions were cut off at 11 Å via a switching function. A reversible, multiple time-step algorithm (25) was employed to integrate the equations of motion with a time step of 4 fs for electrostatic forces; 2 fs for short-range, non-bonded forces; and 1 fs for bonded forces. All bond lengths involving hydrogen atoms were held fixed using the SHAKE (26) and SETTLE (27) algorithms. The system was run at a constant temperature of 300 K and constant pressure of 1 atm. A Langevin dynamics scheme was used for temperature control, and a Nosé-Hoover-Langevin piston was used for pressure control (28), (29).

Starting from the end configuration of the wild-type C3 state equilibration run, we converted the WT VSD into the big omega-current pore by making the following mutations, (R362S/E283D/S357C/M356D). The BOM was solvated in either 500mM GdmCl or 500mM KCl. We equilibrated the 500mM KCl BOM system using the multistage equilibration procedure. The two simulation systems were composed of one Shaker VSD (residues 225–379), 180 POPC molecules (90 per leaflet) fully hydrated in either 500 mM guanidinium chloride (GdmCl) or 500 mM KCl for a total 55,698 or 55,140 atoms, respectively.

Starting with the coordinates from the 500mM KCl system, we changed the

potassium ions to GdmCl and repeated the multistage equilibration protocol. Molecular graphics and simulation analyses were performed using VMD 1.9.1 (30).

4.2.4 Microsecond timescale simulation details

After the equilibration in NAMD2.9, the systems were transferred to Anton, a special-purpose computer for molecular dynamics simulations of biomolecules, and simulated under a range of hyperpolarized (intracellular side negative) membrane potentials (Table 4.1 and 4.2), The CHARMM27 and CHARMM36 force fields were used for the protein and lipids, respectively, and the TIP3P model was used for water. Anton software version 2.11.4 was used. Specific simulation parameters are similar to those used during our previous Anton allocations (31). A reversible multiple-timestep algorithm was employed to integrate the equations of motion with a time step of 6 fs for the long-range nonbonded forces, and 2 fs for short-range non- bonded and bonded forces. The k-Gaussian split Ewald method(32) will be used for long-range electrostatic interactions. All bond lengths involving hydrogen atoms were constrained using the SHAKE algorithm. The simulations were performed at constant temperature (300K) and pressure (1 atm), using Nose-Hoover chains and the Martyna-Tobias-Klein barostat (28). The RESPA algorithm and the temperature and pressure controls were implemented using the multigrator scheme.

Table 4.1. Summary of trajectory lengths for the 500mM KCl system

	Applied TM Voltage (mV)	Number of K^+ Permeation Events	Trajectory length (μs)
500mM KCl	-250	0	5
	-500	1	5.8
	-750	2	4.3*

*VSD swells with water and ions, resuting in non-selective permeation of both K+ (inward) and Cl- (outward) after ~3.76 μs

Table 4.2. Summary of trajectory lengths for the 500mM GdmCl system

	Applied TM Voltage (mV)	Number of Gdm^+ Permeation Events	Trajectory length (μs)
500mM GdmCl	-750	6	3.2*
	-500	11	4.6**
	-250	3	9.7

*VSD swells with water and ions, resuting in non-selective permeation ion permeation (i.e. hydrated Cl- ions flow outward at a higher rate than Gdm+ flow inward) after ~3.75 μs
**VSD distorts around a bound Gdm ion after ~2μs

4.2.5 Membrane electrostatics calculations

To model the applied membrane potential used in electrophysiology recordings, a transmembrane potential was imposed as a constant electric field, with a magnitude determined by the potential profile around the center of the VSD calculated using linearized Poisson-Boltzmann theory (33). We used a range of hyperpolarizing (negative on the intracellular side) electric fields with a magnitude equal to 250, 500 or 750 mV/23 Å. The specific value for the thickness of the dielectric barrier (23 Å) was taken from a linearized Poisson-Boltzmann calculation of the electrostatic potential along a transmembrane axis passing through the center of the VSD, as previously described (33).

4.3 Results

4.3.1 Rate of ionic turnover through VSDs at hyperpolarizing voltages

The rate of cation turnover events measured by Tombola et al.. for potassium ion conduction through the BOM at -250mV is 2.84 ions/μs. We observe three potassium events over the aggregate 15μs of trajectory for the 500mM KCl system. The calculated rate of K^+ ion turnover in our simulations (as determined by dividing the number of ionic events by the length of the trajectory) is 1.75 ions/μs with an applied voltage of -750mV and 0.17 ions/μs with an applied voltage of -500mV (Table 1).

The experimentally measured rate for Gdm^+ turnover in the BOM is three times larger (8.52 ions/μs) than the K+ permeation rate. The calculated rate of Gdm turnover in our simulations is 1.93 ions/μs with a -750mV voltage, 1.96 ions/μs with an applied -500mV voltage and 0.31 ions/μs under a -250mV voltage (Table 2). Thus, our results are in qualitative agreement with experimental measurements, i.e. the total number of Gdm permeation events are greater than K+ permeation at all voltages, however the relatively low number of cation permeation events collected in this study preclude us from extracting accurate conductance values.

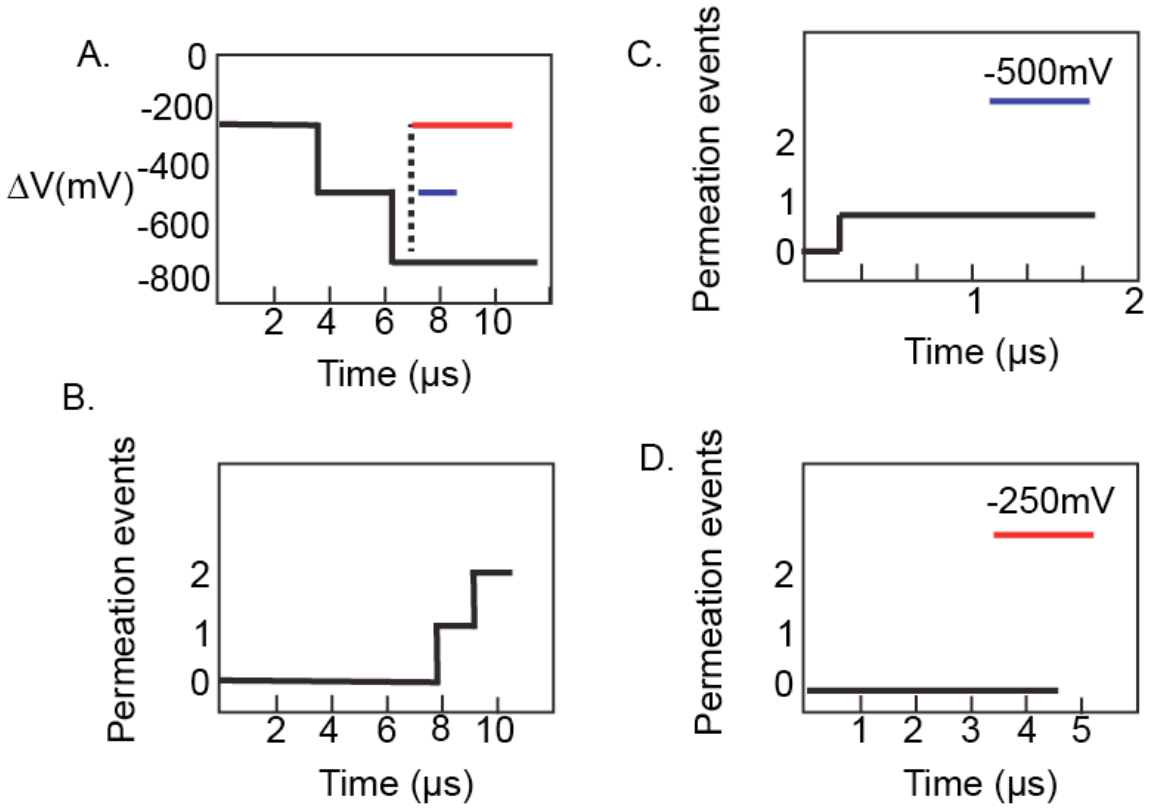

Figure 4.1. Potassium permeation. (A) Time-dependence of applied membrane potential, ΔV, relative to the intracellular side of the membrane (black solid line). The same configuration (Fig), taken from ~6us was used to start two trajectories with an applied -500mV (blue line) or -250mV (red line). (B) K+ permeation events during the stepwise voltage increase. (C) K+ permeation events during the trajectory with an

applied -500mV potential. (D) K+ permeation events (none) during the trajectory with an applied -250mV potential

4.3.2 The potassium cation binding sites and permeation pathway in the BOM VSD

Defining unassisted permeation as a movement of a cation from the extracellular space into the intracellular space, we observe two potassium permeation events during the simulation with a -750mV applied voltage. These permeation events are preceded and followed by a silent time period, i.e. no cation permeation occurs. In the simulation with an applied 750mV voltage, the majority of the time the VSD is empty and the cations remain in the bulk water. Before and after the K+ permeation event the VSD is hydrated by at least one water, as indicated by the time evolution of number density profiles for water.

The first potassium ion permeates in a burst interval of time, entering the VSD from the intracellular side and exiting into the intracellular space over a time span of several tens of nanoseconds, as shown by the time evolution of the z coordinate for the potassium permeation event (Figure 4.2, left panel). The second potassium permeation event is more gradual and occurs over a time span of several hundreds of nanoseconds. Though the time span between entrance and exit are different between the burst and gradual permeation events, both cations events eventually bind into the gating charge transfer center (GTC), defined by Tao et al. as the side chains from F290, E293 and D316. The GTC is composed of a rigid cyclic "cap" from the sidechain of F290 and two negatively charged sidechains, which together gate the transmembrane movement of a positive charge, presumably a basic residue from S4 in the typical non-

conducting VGIC VSD. Consistent with the notion that F290 caps the channel while E293 and D316 interact electrostatically to gate positive charges traveling through the region, we observe the potassium cations bind into the GTC-binding through electrostatic interactions with D316, E293 and cation-π interactions with F290. (Figure 4.3 and Figure 4.4 show sequential snapshots of the first K+ and second K+ entering the BOM VSD). These snapshots of the permeation event over time also reveal several amino acid sidechains involved in K+ permeation.

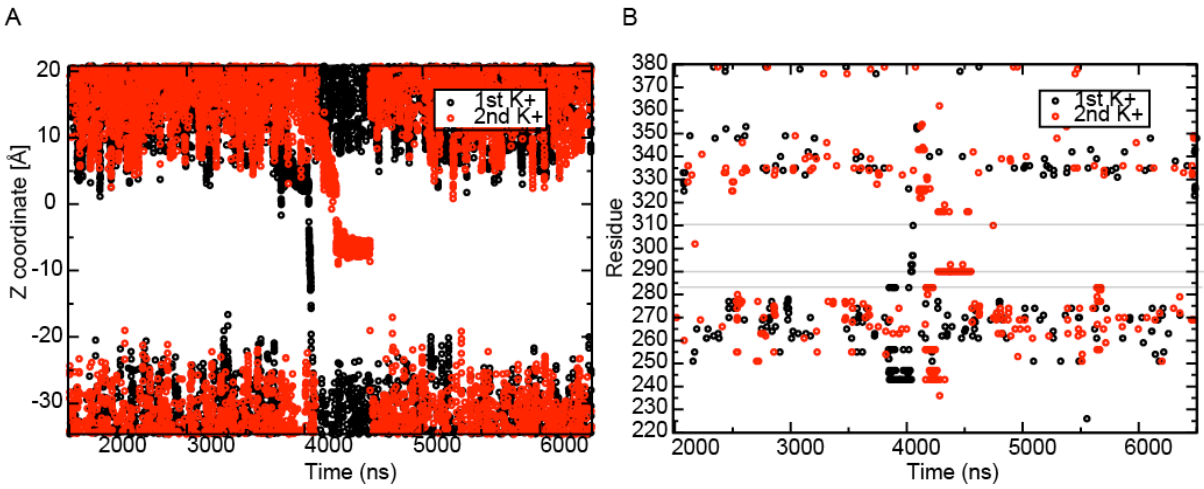

Figure 4.2. The time evolution of the z coordinate for each potassium permeation event (Left) and the time evolution of the sidechains within 4Å of the first (black circles) or second (red circles) the permeating ion. Note that the first K+ ion (black) permeates at around 2000ns and the second event (red) happens from 2125 to 2500ns. Both ions interact first with D283 (Right panel, bottom grey line), then F290 (middle grey line) and finally V310 (top grey line) before completely leaving the center of the VSD.

We observe two different 'entrances' to the omega pore by potassium ions. In the first event, the ion enters between the S1 and S2 helices, being captured from the bulk by the negatively charged sidechain of E268 (Figure 4.3). The second potassium

enters between the S3 and S4 helices (Figure 4.4) and interacts with a different set of residues to enter the pore. Though the extracellular entrance sites are composed of different sidechains, both potassium ions eventually bind into the gating charge transfer center.

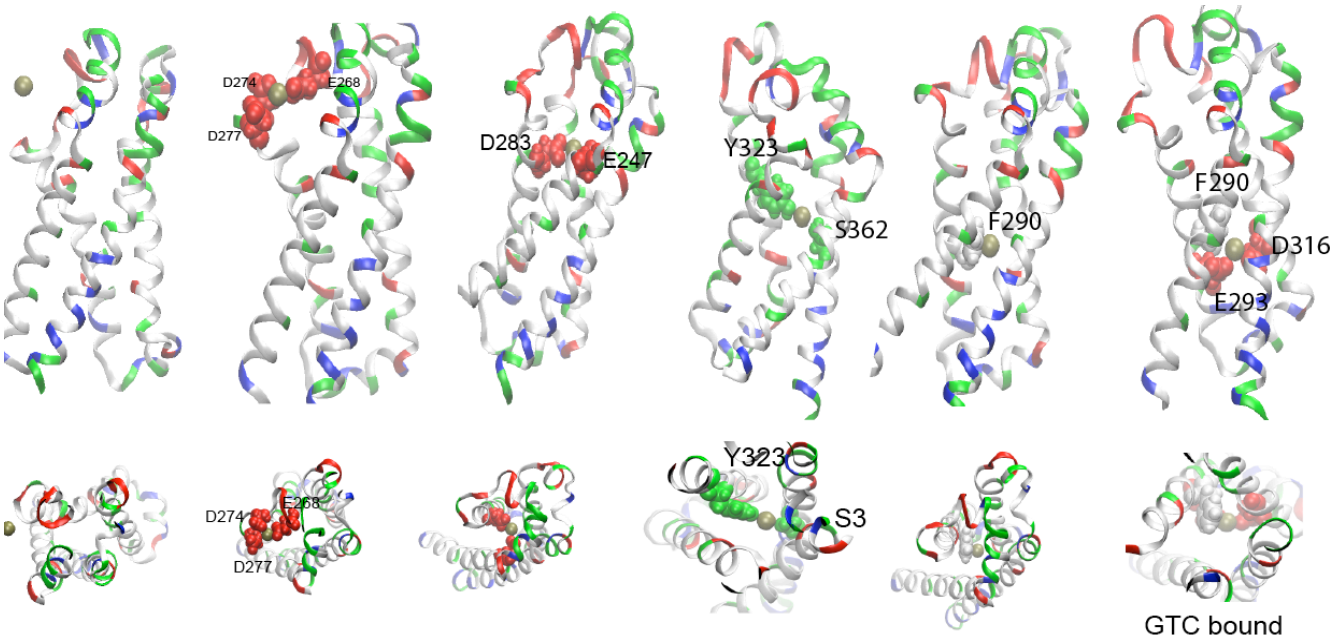

Figure 4.3. Sequential snapshots of the first K+ entering the BOM VSD. The ion gets caught between D274 and D277, binds into a space between D293 and E247, then gets pushed to the center of the VSD by interactions with Y323 and S363 (R1S). The ion stays bound to F290, which rotates intracellularly to trap the potassium in the D316 (D2) and E293 (E1) gating charge transfer center (GTC).

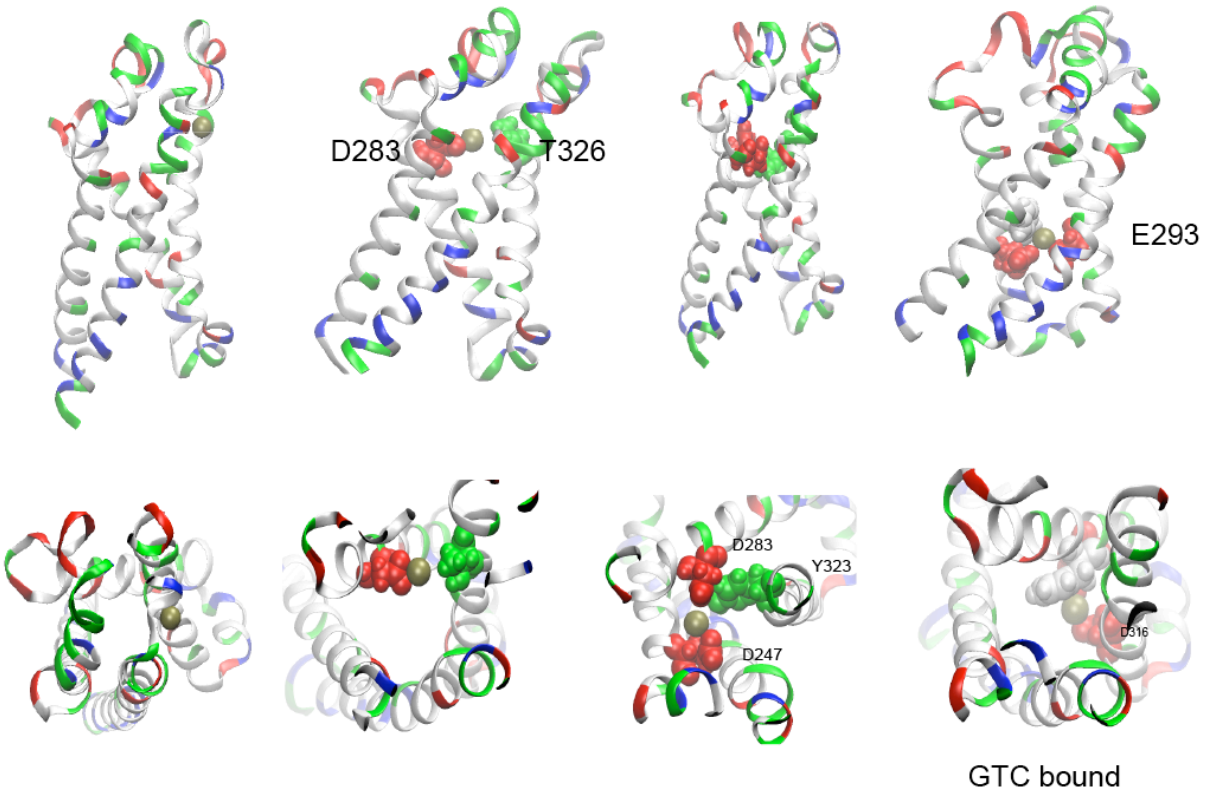

Figure 4.4. Sequential snapshots of the second K+ entering the BOM VSD. The ion enters between S4 and S3 and becomes lodged between D283 and T326. It moves further inward when it binds to D247, D293 and Y323. The last step is for the ion to get pushed into the GTC, where electrostatics and sterics keep the ion bound for several hundred nanoseconds before the ion gets released into the intracellular space. into a space between D293 and E247, then gets pushed to the center of the VSD by interactions with Y323 and S363 (R1S). The ion stays bound to F290, which rotates intracellularly to trap the potassium in the D316 (D2) and E293 (E1) gating charge transfer center (GTC).

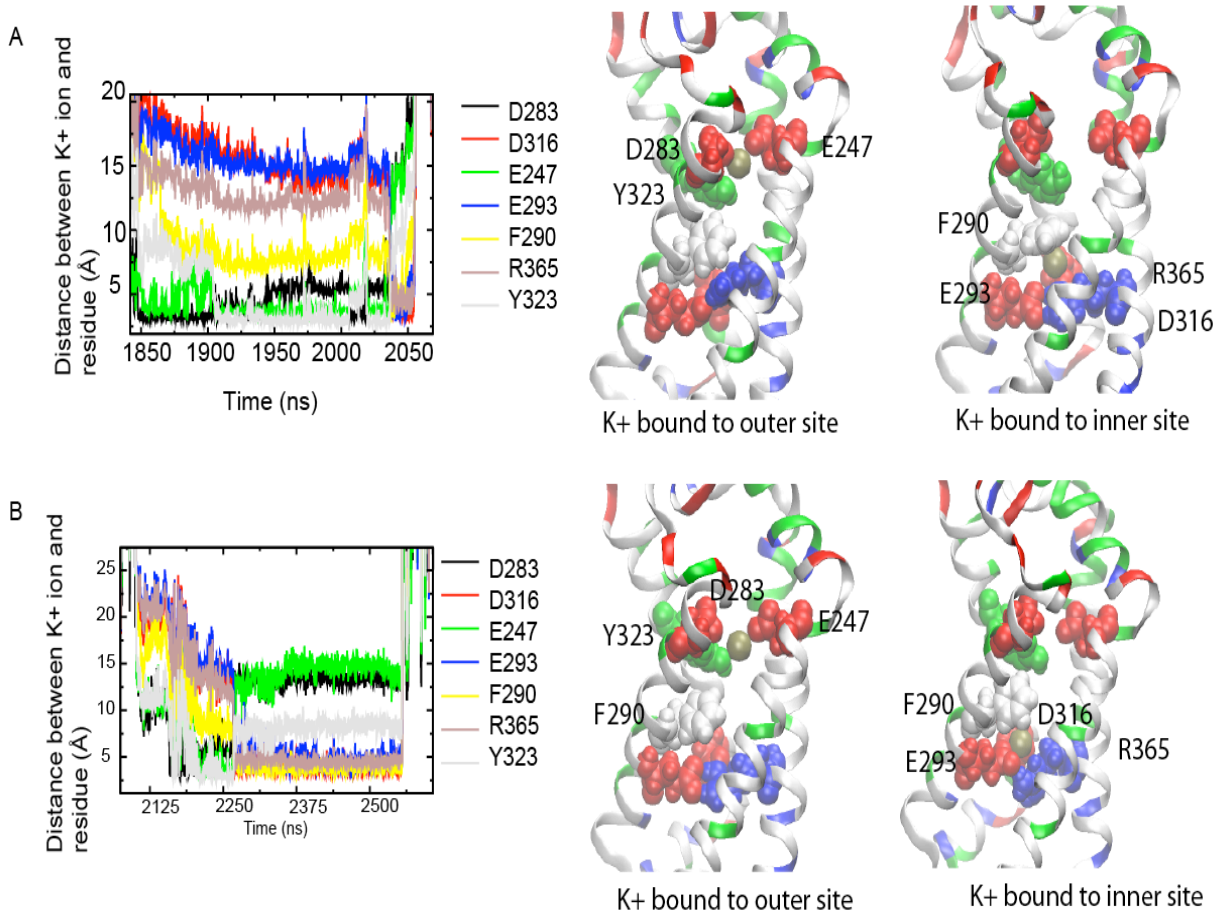

Figure 4.5. The time evolution of distances between the permeating cations and salient sidechains involved in potassium permeation are plotted. Top panel shows the first permeation event, occurring over a ~200ns time frame (1850 to 2050 ns). The bottom panel shows the second permeation event, occurring over a much longer ~400ns time frame. In both cases, an abrupt transition from an outer binding site composed of the D283 (black line), E247 (green line), Y323 (grey line) to an inner binding site composed of F290 (yellow line), D316 (red line), E293 (blue line), R365 (brown line) occurs at 2030ns for the first event and at around 2250ns in the second permeation event

4.3.3 Potassium cation permeation dependence on voltage

To explore the relationship between voltage and K+ binding into the gating charge transfer center (GTC), we took one configuration from the -750mV simulation before the K+ is bound into the GTC (termed K-out) and a second configuration from after K+ is bound into the GTC (termed K-GTC). We applied a -250mV voltage to both configurations and ran each for several (~3μs) μs. We did not observe K+ permeation in either trajectory. Within the first 40ns of the K-GTC bound trajectory, the cation is displaced from the GTC by the basic sidechain of R365 (Figure 4.8). R365 is the second of the highly conserved S4 gating charges (R3) that presumably passes through the GTC in the physiological state of the VSD.

When a K+ is bound into the GTC in the -750mV and -500mV simulations, sidechains from F290 and E293/D316 frequently prevent cation permeation by blocking its release to the extracellular space through steric and electrostatic interactions with the ion. In the -750mV simulation, the next step is moving of the ion into the intracellular space. However starting from a K-GTC configuration and applying a decreased electric field (250mV), the potassium ion is released to the extracellular side, as described, with no additional K+ occupying the GTC during the remaining 3μs simulation. Thus, the release of the ion from the GTC appears to not require or even benefit from a higher voltage, suggesting ion permeation requires a high voltage to bind into the GTC but once bound, the motion of the ion is less voltage-dependent and more dependent on other factors, such as favorable sidechain configuration. To investigate whether the potassium movement out of the GTC site at -250mV was mediated primarily by electric

field strength (as might be expected due to the R3S salt-bridges dominating the interactions) or by sidechain configuration (e.g. the K-GTC configuration was destined to result in the cation getting kicked out, regardless of electric field strength), we used the K-GTC configuration as a starting point for a ~6μs trajectory with an applied -500mV voltage. We found that the extra 250mV made a difference, and the K+ bound into the GTC was moved from the GTC to the intracellular side after 120ns (Figure 4.6).

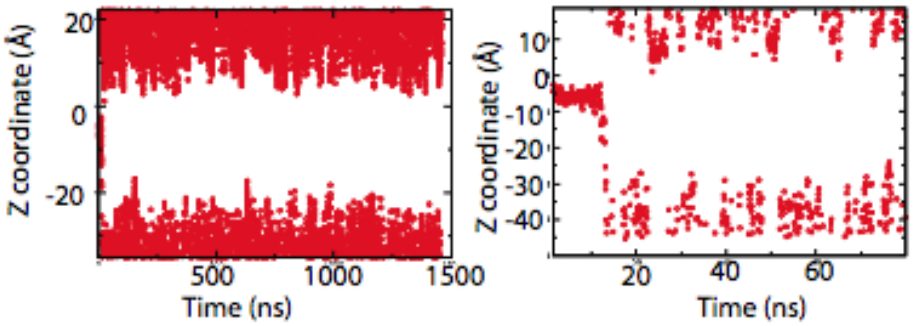

Figure 4.6. The time evolution of the Z coordinate of the potassium ion bound into the GTC, under an applied -500mV field. The left panel includes the z coordinate over the entire 1.5μs trajectory, in which no other ion enters the VSD. The right panel is a closer look at the initial permeation event, which occurs on the order tens of nanoseconds.

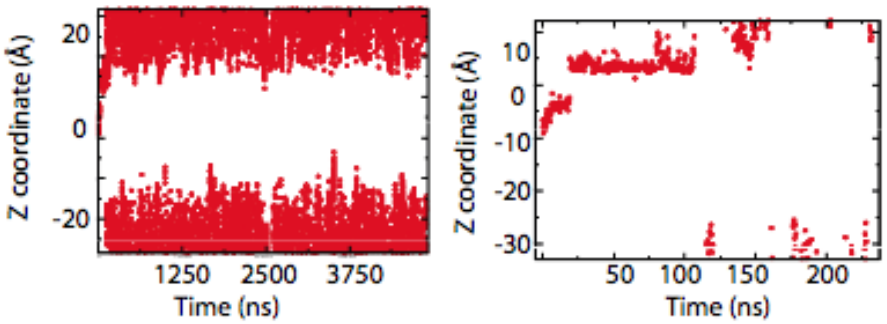

Figure 4.7. The time evolution of the Z coordinate of the potassium ion bound into the GTC, under an applied -250mV field. The left panel includes the z coordinate over the entire ~4.5μs trajectory, in which no other ion enters the VSD. The right panel takes a closer look at the initial hundreds of nanoseconds, where the K+ is unable to permeate and instead ends up pushed back into the extracellular space. The ion floats out of the GTC binding site occurs on the order tens of nanoseconds and is mediated by the rotation of the rigid cyclic cap (F290).

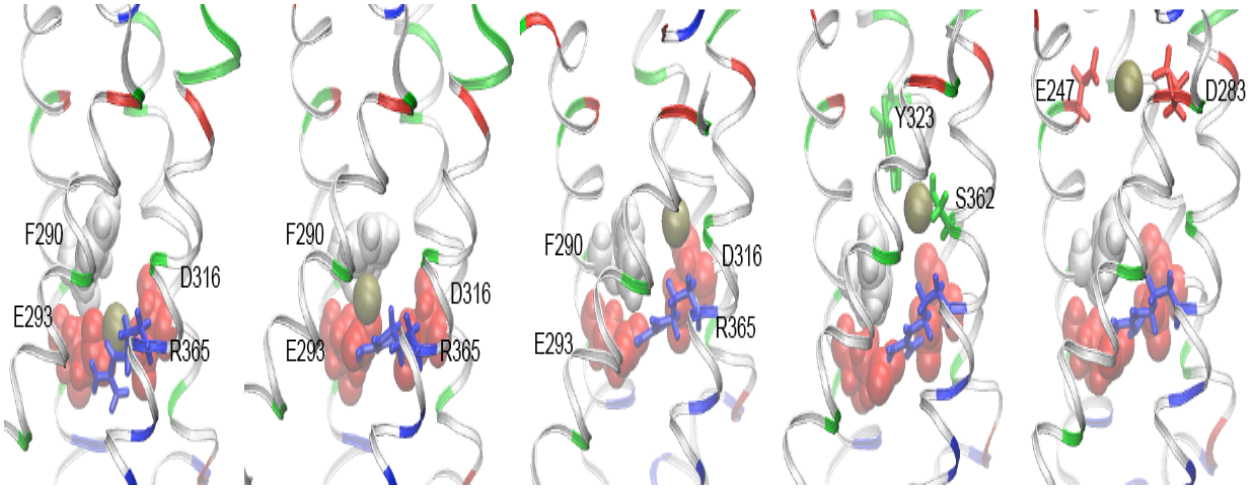

Figure 4.8. Snapshots from the K+ unbinding event at -250mV. The face of the 'rigid cap' F290 sidechain rotates approximately 45° allowing the cation to be released back into the extracellular space. This rotation is prompted by the arginine (R365) sidechain pushing the potassium ion out of the binding pocket and coordinating the acidic charges of the GTC. The protein backbone is in ribbon representation and colored as described in Figure 4.2. The sidechains of F290, D316 and E284 are represented as white or red van der Waal spheres. The R365, E247, D283, Y323 and S362 sidechains are shown in licorice. The potassium ion is gold.

However, after the initial permeation event, we never observe any additional cations binding into the GTC. Thus, the unbinding/release of the ion from the GTC into the extracellular space is not hindered by a voltage larger than 250mV, however it doesn't appear to require a voltage any higher than 500mV. In contrast, potassium only binds to the GTC under voltages higher than 750mV.

4.3.4 Water and sidechain densities of the pore cavity over time for the 500mM KCl -750mV simulation

Analysis of the water density profile along the z axis, normal to the membrane plane, shows the narrowest region in the BOM runs from z=5Å to 7.5Å, where z is the distance from the center of the bilayer (Figure 4.9, left panel).

During the permeation event from 2 to 3 us, the VSD swells with water between z=2.5 and z=0. In the μs after permeation, the swelling decreases and the overall qualitative features (i.e. the most constricted sites) of the water density return to the state preceding permeation. During the last ~μs of simulation, the VSD swells with water and becomes a non-specific hole in the membrane, allowing Cl- ions to pass outward.

The width of the z-coordinate density profiles for residue sidechains involved in the gating charge transfer center become wider over time (Figure 4.9, right panel), indicating that the motions of the sidechains become more dynamic as the VSD permeates potassium.

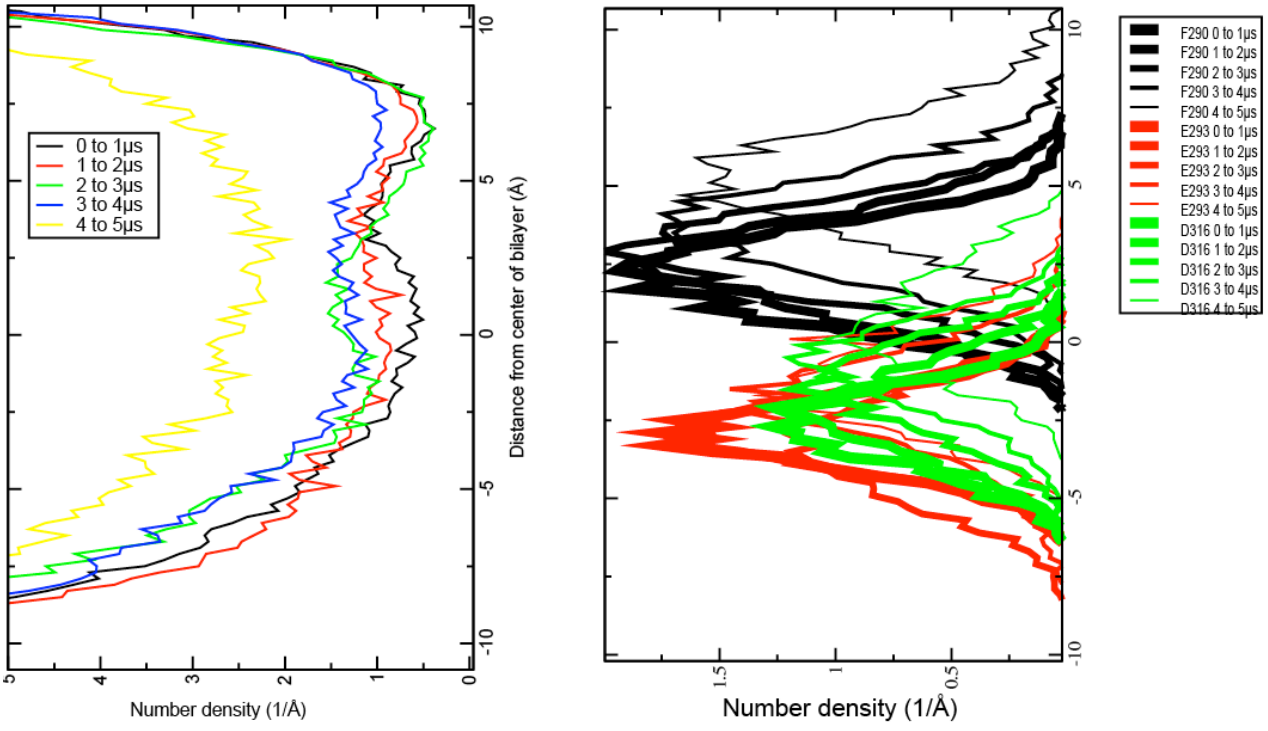

Figure 4.9. The time evolution of number density profiles for water (left panel) and gating charge transfer center sidechains (right panel) during the trajectory with an applied -750mV voltage. The most constricted region of the BOM, where the water

density drops below 1/A, is initially between z=5Å and 7.5Å (black line), here z is the distance from the center of the bilayer.

4.3.5 The Gdm+ cation binding sites and permeation mechanism in the BOM VSD

The potassium permeation events occur independently, i.e. one potassium permeates before the next one enters the VSD. In contrast, Gdm+ permeation occurs in a two-ion 'knock-off' mechanism, where the entrance of a second Gdm+ into the VSD drives permeation of the first Gdm+ into the extracellular space (Figure 4.11 and 4.1210). The knock-off event occurs near the region of the GTC, where one Gdm binds and the next Gdm binds and pushes the first Gdm+ out. The sidechain of F290 initially faces the VSD interior, playing a large role in K+ permeation through cation-π interactions and steric hindrance, blocking the K+ from being ejected back into the intracellular space. During permeation, the large Gdm molecule pushes the bulky F290 side chain from the most constricted region of the VSD, forcing the sidechain to turn away from the hydrated VSD crevice toward the bilayer. This configuration of the GTC sidechains is unique when compared to the usual GTC, thus we refer to this Gdm+ binding site as the modified GTC (mGTC) site.

The cation permeation event is largely driven by electrostatics in both the KCl and GdmCl simulations, i.e. the cations tend to associate with acidic residues as they traverse the pore. Thus, the sidechains of residues along the Gdm+ permeation pathway are similar to those involved in K+ permeation (Figure 4.13 shows sidechain distance to the permeating ion over time for Gdm+) The most extracellular binding site for both ions involves sidechains from residues Y323, E247 and D283. The intracellular

binding site is composed of R365, and the sidechains from the GTC residues F290, E293, D316.

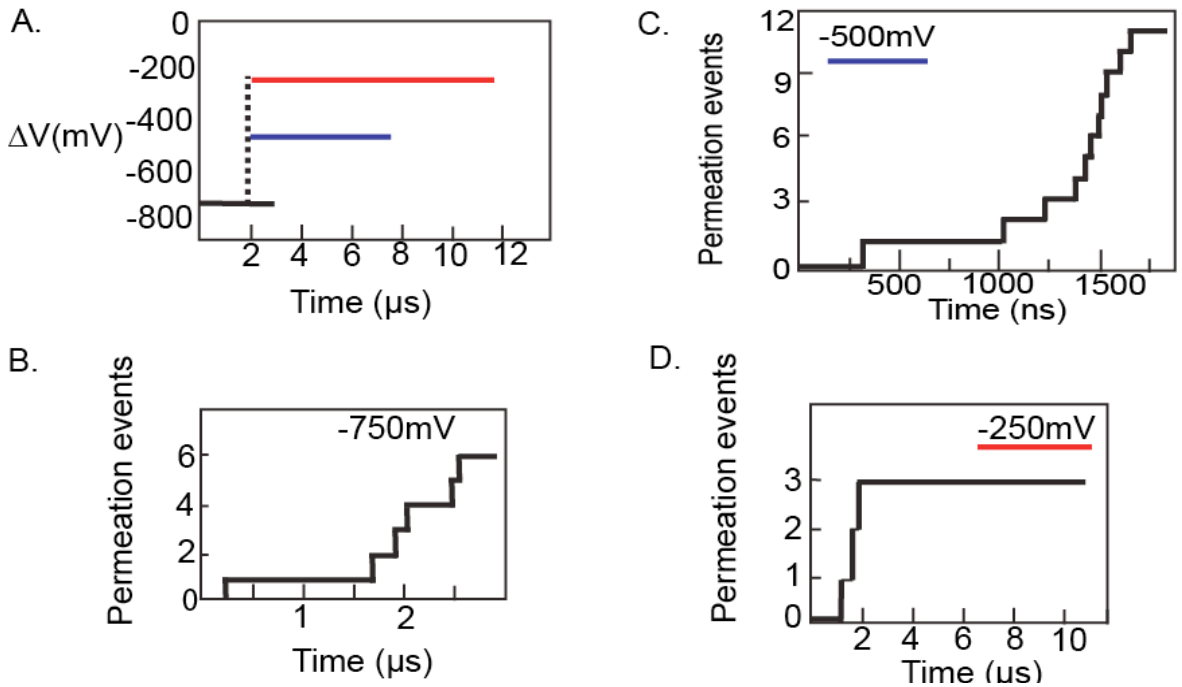

Figure 4.10. Voltage and permeation in the 500mM GdmCl simulation (A) Time-dependence of applied membrane potential, ΔV, relative to the intracellular side of the membrane. The starting structure came from the K+ -750mV trajectory and was run under a -750mV potential for ~3.2μs. After observing 6 permeation events under a -750mV potential, we started two simulations taken from the same GdmCl configuration but decreasing the magnitude of the voltage from -750mV to -250mV (red line) or -500mV (blue line). (B) Gdm+ permeation events over time in the -750mV trajectory. (C) 11 Gdm+ permeation events occur over time during the -500mV trajectory. (D) Three Gdm+ permeation events occur over time during the -250mV trajectory.

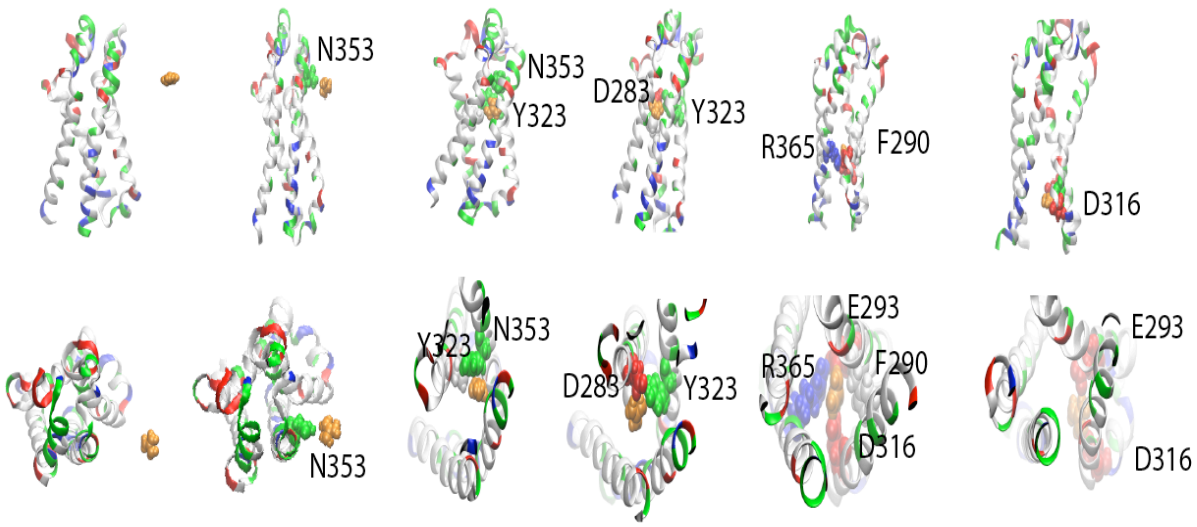

Figure 4.11. Representative snapshots for the sequence of events in Gdm permeation. Two ions are coordinated within the area of the GTC. The Phe 290 is pushed out by the incoming Gdm. This is different than the previously described potassium permeation events, where permeation occurs sequentially and independently. The ion enters between S3 and S2 and becomes lodged between near N353 and Y323. It moves further inward when it interacts with the negatively charged D283 and the bulky sidechain of Y323. The last step is for the ion to get pushed into the region of the GTC residues (F290, E293 and D316), where electrostatics and sterics keep the ion bound for several tens of nanoseconds before a second Gdm ion enters the region and knocks the first ion off into the intracellular space (Figure 12). The crowded sidechain and Gdm+ configuration near the GTC causes the F290 sidechain to be pushed from an inward VSD facing configuration to an outward lipid facing conformation. Because the Gdm+ modifies the prototypical architecture of the GTC, we call this binding site the modified GTC (mGTC).

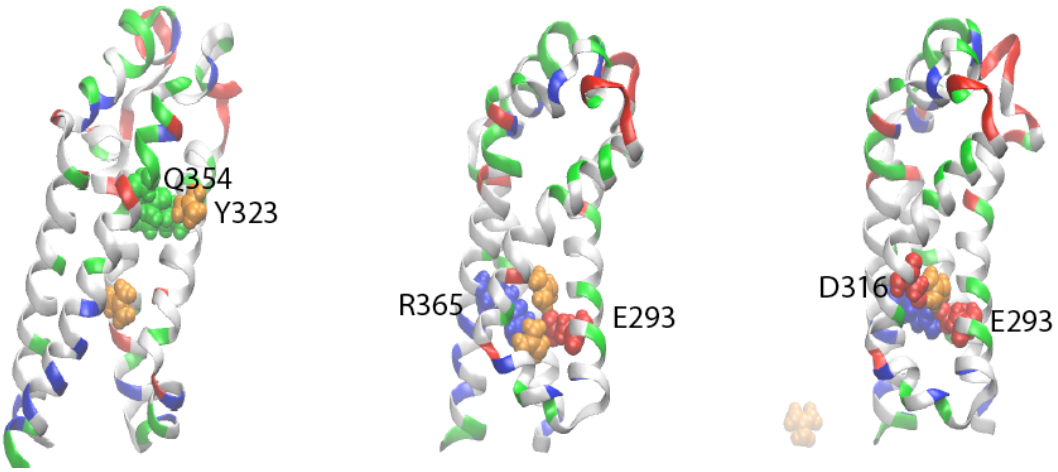

Figure 4.12. Representative snapshots of the two-ion knock off mechanism, where the first Gdm ion is bound into a modified GTC (left) and then a second Gdm enters (middle), which forces the first Gdm+ to be released into the intracellular space. The BOM protein is shown in ribbon representation colored by residue type (basic residues are blue, acidic resides are red, polar sidechains are green and hydrophobic or nonpolar residues are white). The salient side chains are in van der Waals representation and colored by residue type. The Gdm+ ions are orange and shown in vdW representation.

4.3.6 The Gdm+ cation permeation dependence on voltage

To explore the relationship between voltage and the Gdm+ permeation mechanism, we took a configuration from the -750mV simulation where the first Gdm+ is bound in the mGTC site and the second Gdm+ has not yet entered the center of VSD. To this configuration, we applied either a -500mV or -250mV voltage and ran the systems for 4.6μs and 9.7μs, respectively. We observed 11 permeation events in the -500mV trajectory and three events in the -250mV trajectory. The sidechain distance to the permeating ion over time for all permeation events are available in the Supplementary Material.

The aggregate 20 Gdm permeation events were observed at three applied voltages (Figure 4.14), whereas K+ permeation only occurred with the higher voltages. This suggests the architecture of the VSD is uniquely suited to allow large guanidine ions through the center of the VSD easier than the physiologically available monovalent cations. The similarity in molecular size and charge of a Gdm with the sidechain guanidine of arginine residues supports the experimentally proposed notion that the path followed by the Gdm could overlap with the motions of the S4 arginines.

The time scale for Gdm permeation events varied from ten to hundreds of nanoseconds, (Figure 4.14) however, all 20 events followed the 2-ion knock-off mechanism where the first Gdm binds into the mGTC VSD and the second cation binding forces it out.

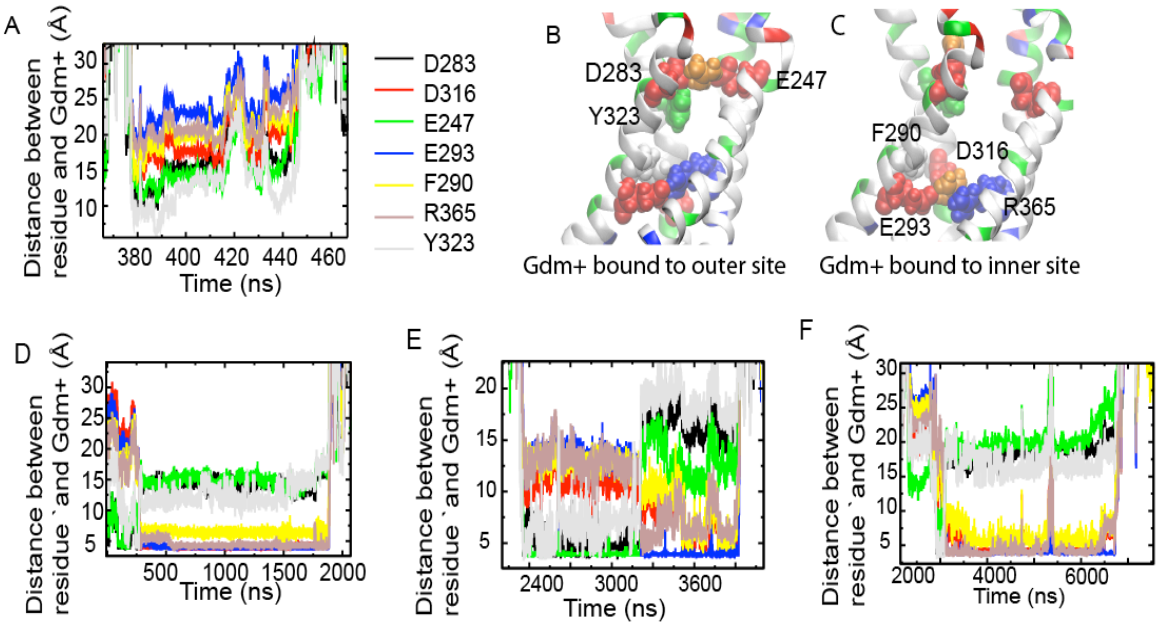

Figure 4.13. Time evolution of residue distances to the permeating Gdm ion, for the first permeation event (A) in the applied -750mV trajectory. Panel B and C show representative snapshots of the inner and outer binding site for Gdm+. Representative plots for permeation events in the applied -750mV (D), -500mV (E) or -250mV (F) trajectories show that the overall time to permeate a Gdm ion ranges from hundreds (i.e. A vs D) to thousands of nanoseconds, the side chains involved are the same in all events, and two-ion knock-off permeation mechanism is observed in the modified GTC binding site. (These plots are available for all 20 permeation events and can be found in the supplementary material.)

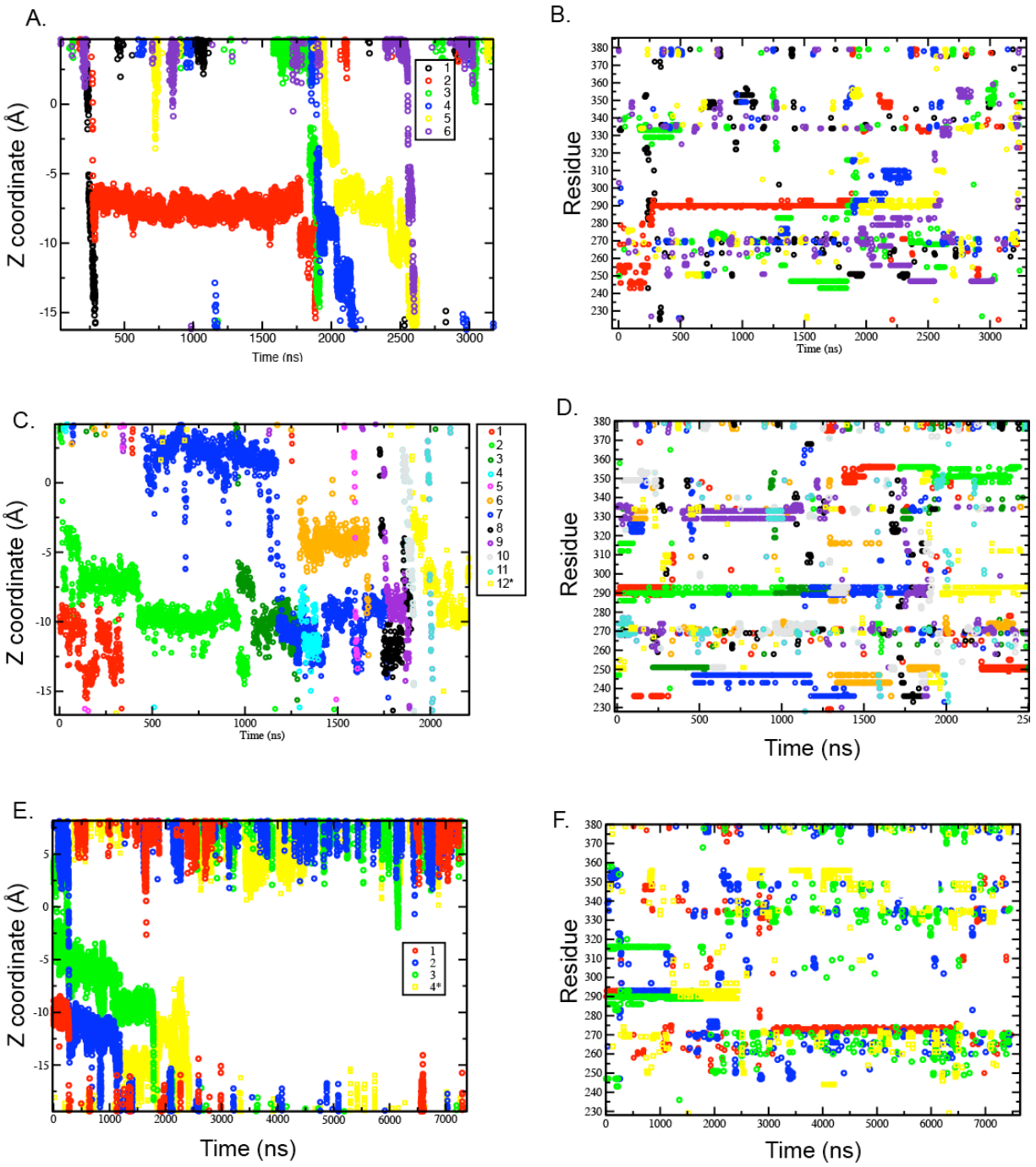

Figure 4.14. Panels A and B, C and D, and E and F come from 500mM GdmCl simulations with an applied -750mV, -500mV or -250mV potential, respectively. Gdm permeation. First frame taken from the 750mV trajectory where two Gdm are bound in the pore.

4.3.7 Gdm+ permeation events and water density in the pore over time

During the first μs of 500mM GdmCL simulation with an applied -750mV voltage and prior to Gdm+ entrance into the VSD, the most constricted region of the pore stretches from z=2.5Å to 7.5Å, where z is distance from the center of the bilayer (Figure 4.15). Before and after Gdm+ permeation the outer constricted site becomes hydrated and an area of high water density develops in the 0 to 2.5 region. The analogous investigation in a typical non-conducting VGIC VSD (e.g. Kv1.2-2.1) reveals a single constriction at the center of the bilayer where the water density drops to zero. This 'double-gasket' hydration pattern, where the VSD develops two constricted regions and a water bleb in the middle, has been described in simulations and structures of other conducting VSDs, including the proton-conducting hHv1 VSD (R2-Hv1 model by Wood et al.) and the recently solved chimera voltage-gated proton channel mHv1cc structure (34).

In the -500mV simulation, we observe eleven permeation events in the first ~3μs of trajectory. The water density profile reveals a well-hydrated VSD interior (Figure 4.15, panel B) for the entirety of the trajectory, i.e. none of the water density profiles dropping below 1/Å.

In the 9.7μs trajectory of the BOM with an applied -250mV potential, the water density in the VSD drops to zero (Figure 4.15, panel C) after three Gdm permeate, suggesting that Gdm+ permeation is not the primary cause of VSD breakdown but rather the field strength and subsequent non-selective water/anion permeation. After the initial permeation events in the first few μs, the VSD remains completely impermeant to cations and anions for the remainder of the trajectory.

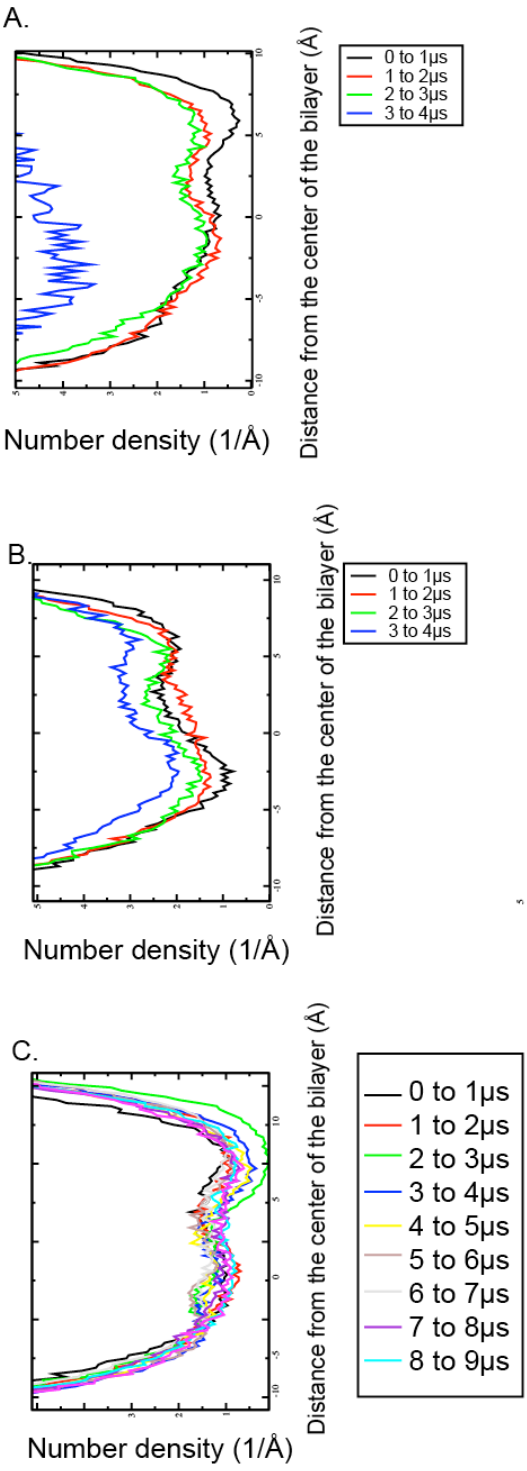

Figure 4.15. Probing hydration of the VSD during Gdm+ permeation. The evolution of water density profiles over time for the 500mM Gdm system with an applied -750mV (Panel A.), -500mV (Panel B.) or -250mV (Panel C.).

4.4 Discussion

Since the big omega-current mutant exhibits single-channel cation currents on the order of ~1 pA in patch-clamping experiments, we predicted that cation permeation events could be adequately sampled using atomistic simulations in the 10 μs timescale. Thus, we performed atomistic MD simulations on the 10-**μ**s timescale of the omega current in the *Shaker* closed state BOM VSD mutant under potential. By simulating the BOM under a range of 250mV, 500mV or 750mV hyperpolarizing voltages in the presence of either 500mM KCl or 500mM GdmCl, we observed a total of three K+ permeation events and 20 Gdm+ permeation events.

4.4.1 Comparing computational results to experiment

Our observation of cation displacement over ~3-5μs is compatible with electrophysiological measurements on eukaryotic channels. The stochastic nature (i.e. rapid on and rapid off kinetics of the current) of cation permeation makes it difficult to accurately sample ion conductance, however the rate of Gdm+ turnover versus K+ turnover in our simulations is in qualitative agreement with the current measurements reported by Tombola et al. (i.e. gdm was measured to have a rate three times the K ionic turnover rate.) Additionally, we observe relatively long time periods (several μs) without ionic conduction in both the KCl and GdmCl trajectories, suggesting the lack of sampling may account for the quantitative discrepancy between the experimentally

measured current and simulation.

We observe several different pathways available to monovalent cations to enter the VSD. Tombola et al. present a model where the cations typically enter between the interface of the VSD and the pore domain. The physiological omega pore exists as part of a homotetrameric assembly, where the alpha-current runs through the pore domain and the omega current travels through 4 VSDs. Tombola et al. find that the entrance to the omega pore is between the interface of the VSD and the pore domain. Thus, a limitation of our BOM model is that it is a monomer of only the VSD (S1-S4), and thus the effects of the pore region (S5-S6) on ion permeation are not represented.

In addition to describing the mechanistic role of the GTC residues in the cation binding event, we are able to observe every amino acid interaction with the permeating cation on an atomistic scale. Tombola et al. characterized interactions between permeating cations and the omega-pore, and determined which residues change the omega current and what type of interaction the sidechain has with the permeating cation, i.e sterics, electrostatics, null or indirect (SENI). The residues shown to have the largest impact on the omega current are S240 in S1, E283, C286, F290 in S2, T329 in S3 and Q354, S367, L348 and A359 in S4. The BOM is a quadruple mutant of R362S, S357C, E283D and M356D. We find residue 283 plays a role in the outer binding site, while F290 plays a role in the inner binding site.

4.4.2 Comparing computational results to previous simulations of omega currents

To date, our simulations are the first to use an experimentally validated closed state for

Shaker to model the omega-current. Previous computational simulation studies from Jensen et al. (35), Delemotte et al. (36) and Khalili-Araghi et al. (37) used the Kv1.2 structure as the template for modeling the Shaker VSD. Ambiguity about the closed state model of the VSD persist due to the lack of TM potential in the VGIC crystal structures. Several experimental and computational studies have proposed closed-state VSD structures, however the Henrion et al. models are the first to experimentally trap and validate closed state configurations for the Shaker channel. Additionally, the Shaker VSD sequence shares only X percent identity with the Kv1.2 channel, thus, many key residues from Shaker are different from the Kv1.2. The differences in sequence between the two VSDs hinder the direct comparison to the original omega-pore experiments, which were performed with Shaker.

The water density profiles in the Khalili-Araghi et al. study are distinct from the observations made by Delemotte et al., who described the mutant conducting VSDs are reported to be ‘swollen-stable’ structures, where a connected hydration pathway opens up between the intra- and extracellular media. Khalili et al. report a formation of a connected hydrated pathway through however, no significant swelling of the VSD driven by the penetration of water molecules is observed in the current simulations. We also find swelling on the several μs timescale.

4.4.3 Hypothesizing a role for the two-cation Gdm+ knock-off permeation mechanism in enhancing K+ omega currents

According to Tombola et al. (38), K+ currents through the VSD are enhanced by small concentrations of Gdm+. Our GdmCl simulations may offer insight into this phenomenon. Based on the observed two-ion knock-off Gdm permeation mechanism, our hypothesis is that the Gdm may get lodged into the mGTC and then 'hold the door open' for other positive ions to pass. The mechanism may involve the bound Gdm removing the steric hindrance and hydrophobic effect by pushing the rigid cyclic cap (F290) outward. This modifies the GTC in such a way that the potassium ions may be able to enter the site at lower voltages or at lower concentrations. To test this hypothesis, simulations of a Gdm bound into the GTC with 500mM KCl are necessary, but beyond the scope of the current study.

4.4.4 Limitations of the applied electric field approach

Modeling an accurate representation of the experimental transmembrane voltage is a challenge for simulation experts, and several methods exist. Tarek and coworkers report that an ion imbalance method has been successful to model a TM voltage, (39), however, to maintain an ion imbalance in a periodic boundary condition (PBC) membrane protein system, the system size must be doubled to create two distinct areas of bulk water. Alternatively, one can employ the constant electric field approach, which we used in the current study.

The constant electric field approach exploits the approximation that the membrane acts as a parallel plate capacitor, where the voltage drop (ΔV) across the membrane/capacitor can be calculated as:

$$\Delta V = Ed$$

where E is the external electric field and d is the distance between the parallel plates.

The calculated value for d in simulations is non-trivial and two distinct methods are commonly used. Assuming the membrane potential falls linearly across the width of the bilayer, we calculate the distance using the method described previously. (33) Alternatively, d can be set to the entire simulation cell dimension in the Z direction. Either way, the constant field method simply adds a constant force q_iE acting on all the charges, q_i in the system, regardless of their position. This is problematic since has been shown that the TM potential arises from charge distributions at the microscopic level (40). Thus, we acknowledge that the magnitude of the applied voltage may not quantitatively match experiment or physiologic values, but by running both GdmCl and KCl systems under the same electric field strengths (i.e. increasing the voltage systematically by 250mV and keeping d=23A) we are controlling for possible errors in absolute magnitude and focus instead on the effects of changes in magnitude.

Our observation that K+ movement into the GTC binding site requires a -750mV voltage at minimum could be the result of the assumptions made in the applied electric field approach. Thus, this observation could suggest that permeating a K+ into the GTC requires a field strength > 250mV/23A, or that the way the electric field is applied in the Z direction does not allow for realistic motions of a twisted protein. We employed the same approach with a -500mV voltage and found the field strength was enough to permeate the K+ ion already bound to the GTC within the first 125ns. However we did not observe any K+ enter the GTC for any part of the remaining 6.12μs.

4.5 Concluding remarks

In summary, we have characterized the permeation of monovalent cations through the BOM. We find a potassium ion can bind into the GTC when a -750mV voltage is

applied, but not when -500mV or -250mV is applied. When we start potassium in the GTC binding site, we observe permeation at lower voltages (500mV) but not (250mV), suggesting that the energetic barrier between the extracellular space and the intracellular space is the GTC. We report on atomistic details of Gdm permeation in a VSD for the first time. Cation conduction through VSDs is often pathological and is linked to a variety of disease states, including cancer, neurological disorders and heart problems(41-43). Understanding how cation conduction occurs through VSDs at the atomistic level has numerous potential applications in the development of novel therapeutics.

4.6 References

1. Iwasaki H*, et al.* (2008) A voltage-sensing phosphatase, Ci-VSP, which shares sequence identity with PTEN, dephosphrylates phophatidylinositol 4,5-biphosphate. *Proc. Natl. Acad. Sci. U.S.A.* 105:7970-7975.
2. MacKinnon R, Aldrich RW, & Lee AW (1993) Functional stoichiometry of Shaker potassium channel inactivation. *Science* 262:757-759.
3. Hille B (2001) *Ion Channels of Excitable Membranes* (Sinauer Associates, Inc., Sunderland) 3rd Ed pp 1-814.
4. Sasaki M, Takagi M, & Okamura Y (2006) A voltage-sensor domain protein is a voltage-gated proton channel. *Science* 312:589-592.
5. Ramsey IS, Moran MM, Chong JA, & Clapham DE (2006) A voltage-gated proton-selective channel lacking the pore domain. *Nature* 440:1213-1216.
6. Kohout SC, Ulbrich MH, Bell SC, & Isacoff EY (2008) Subunit organization and functional transitions in Ci-VSP. *Nature Struct. Mol. Biol.* 15:106-108.
7. Murata Y, Iwasaki H, Sasaki M, Inaba K, & Okamura Y (2005) Phosphoinositide phosphatase activity coupled to an intrinsic voltage sensor. *Nature* 435:1239-1243.
8. Cahalan MD & Chandy KG (2009) The functional network of ion channels in T lymphocytes. *Immunol Rev* 231(1):59-87.
9. Tombola F, Pathak MM, & Isacoff EY (2005) Voltage-sensing arginines in a potassium channel permeate and occlude cation-selective pores. *Neuron* 45:379-388.

10. Sokolov S, Scheuer T, & Catterall WA (2005) Ion premeation through a voltage-sensitive gating pore in brain sodium channels having voltage sensor mutations. *Neuron* 47:183-189.
11. Sokolov S, Scheuer T, & Catterall WA (2010) Ion permeation and block of the gating pore in the voltage sensor of NaV1.4 channels with hypokalemic periodic paralysis mutations. *J Gen Physiol* 136(2):225-236.
12. Sokolov S, Scheuer T, & Catterall WA (2008) Depolarization-activated gating pore current conducted by mutant sodium channels in potassium-sensitive normokalemic periodic paralysis. *Proc Natl Acad Sci U S A* 105(50):19980-19985.
13. Sokolov S, Scheuer T, & Catterall WA (2007) Gating pore current in an inherited ion channelopathy. *Nature* 446(7131):76-78.
14. Struyk AF, Markin VS, Francis D, & Cannon SC (2008) Gating pore currents in DIIS4 mutations of NaV1.4 associated with periodic paralysis: saturation of ion flux and implications for disease pathogenesis. *J Gen Physiol* 132(4):447-464.
15. Struyk AF & Cannon SC (2007) A Na+ channel mutation linked to hypokalemic periodic paralysis exposes a proton-selective gating pore. *J Gen Physiol* 130(1):11-20.
16. Catterall WA (2010) Ion channel voltage sensors: structure, function, and pathophysiology. *Neuron* 67(6):915-928.
17. Andersen OS (2011) Perspectives on: Ion selectivity. *J Gen Physiol* 137(5):393-395.

18. Jo S, Kim T, Iyer VG, & Im W (2008) CHARMM-GUI: a web-based graphical user interface for CHARMM. *J Comput Chem* 29(11):1859-1865.

19. Phillips JC*, et al.* (2005) Scalable molecular dynamics with NAMD. *J. Comput. Chem.* 26:1781-1802.

20. MacKerell AD, Jr.*, et al.* (1998) All-atom empirical potential for molecular modeling and dynamics studies of proteins. *J. Phys. Chem. B* 102(18):3586-3616.

21. Klauda JB*, et al.* (2010) Update of the CHARMM all-atom additive force field for lipids: validation on six lipid types. *Journal of Physical Chemistry B* 114:7830-7843.

22. Jorgensen WL, Chandrasekhar J, Madura JD, Impey RW, & Klein ML (1983) Comparison of simple potential functions for simulating liquid water. *J. Chem. Phys.* 79(2):926-935.

23. Darden T, York D, & Pedersen L (1993) Particle mesh Ewald: An $N \cdot \log(N)$ method for Ewald sums in large systems. *J. Chem. Phys.* 98:10089-10092.

24. Essmann U*, et al.* (1995) A smooth particle mesh Ewald method. *J. Chem. Phys.* 103:8577-8593.

25. Grubmüller H, Heller H, Windemuth A, & Schulten K (1991) Generalized Verlet algorithm for efficient molecular dynamics simulations with long-range interactions. *Mol. Simul.* 6:121-142.

26. Ryckaert J-P, Ciccotti G, & Berendsen HJC (1977) Numerical integration of the Cartesian equations of motion of a system with constraints: Molecular dynamics of *n*-alkanes. *Journal of Computational Physics* 23:327-341.

27. Miyamoto S & Kollman P (1992) An analytical version of the SHAKE and RATTLE algorithm for rigid water models. *J. Comput. Chem.* 13:952-962.

28. Martyna GJ, Tobias DJ, & Klein ML (1994) Constant-pressure molecular-dynamics algorithms. *J. Chem. Phys.* 101:4177-4189.

29. Feller SE, Zhang Y, Pastor RW, & Brooks BR (1995) Constant pressure molecular dynamics simulation: The Langevin piston method. *J. Chem. Phys.* 103(11):4613-4621.

30. Humphrey W, Dalke W, & Schulten K (1996) VMD: Visual molecular dynamics. *J. Mol. Graph.* 14(1):33-38.

31. Freites JA, Schow EV, White SH, & Tobias DJ (2012) Microscopic origin of gating current fluctuations in a potassium channel voltage sensor. *Biophys. J.* 102(11):L44-L46.

32. Shan Y, Klepeis JL, Eastwood MP, Dror RO, & Shaw DE (2005) Gaussian split Ewald: a fast Ewald mesh method for molecular simulation. *J. Chem. Phys.* 122:054101-054101 to 054101-054113.

33. Krepkiy D*, et al.* (2009) Structure and hydration of membranes embedded with voltage-sensing domains. *Nature* 462:473-479.

34. Takeshita K*, et al.* (X-ray crystal structure of voltage-gated proton channel. *Nat Struct Mol Biol* 21(4):352-357.

35. Jensen MO*, et al.* (2012) Mechanism of voltage gating in potassium channels. *Science* 336(6078):229-233.

36. Delemotte L, Treptow W, Klein ML, & Tarek M (2010) Effect of sensor domain mutations on the properties of voltage-gated ion channels: molecular dynamics studies of the potassium channel Kv1.2. *Biophys. J.* 99:L72-L74.

37. Khalili-Araghi F, Tajkhorshid E, Roux B, & Schulten K (2012) Molecular dynamics investigation of the omega-current in the Kv1.2 voltage sensor domains. *Biophys J* 102(2):258-267.

38. Tombola F, Pathak MM, Gorostiza P, & Isacoff EY (2007) The twisted ion-permeation pathway of a resting voltage-sensing domain. *Nature* 445:546-549.

39. Delemotte L, Dehez F, Treptow W, & Tarek M (2008) Modeling membranes under a transmembrane potential. *J Phys Chem B* 112(18):5547-5550.

40. Roux B (2008) The membrane potential and its representation by a constant electric field in computer simulations. *Biophys. J.* 95:4205-4216.

41. Wu LJ (Voltage-Gated Proton Channel HV1 in Microglia. *Neuroscientist*.

42. Cannon SC (2006) Pathomechanisms in channelopathies of skeletal muscle and brain. *Annu Rev Neurosci* 29:387-415.

43. Fiske JL, Fomin VP, Brown ML, Duncan RL, & Sikes RA (2006) Voltage-sensitive ion channels and cancer. *Cancer Metastasis Rev* 25(3):493-500.

4.7 Supporting Material

After several microseconds of applied -750mV, the proteins fall apart and chloride ions flow outward. This outward flow of anions is an non-physiological finding. By replacing the monovalent anions with large non-vsd permeable anions, Tombola et al. confirm the omega current is carried by cations moving outward rather than cations moving inward. Since the electric field is modeled simply by imposing the force F=qE in the z direction and assumes a constant drop across the membrane, and E=V/d both the chloride ions and potassium ions feel the same magnitude electric field, a limitation of the current simulation models and one potential reason for the observed protein instability in the presence of chloride as the counter-anion.

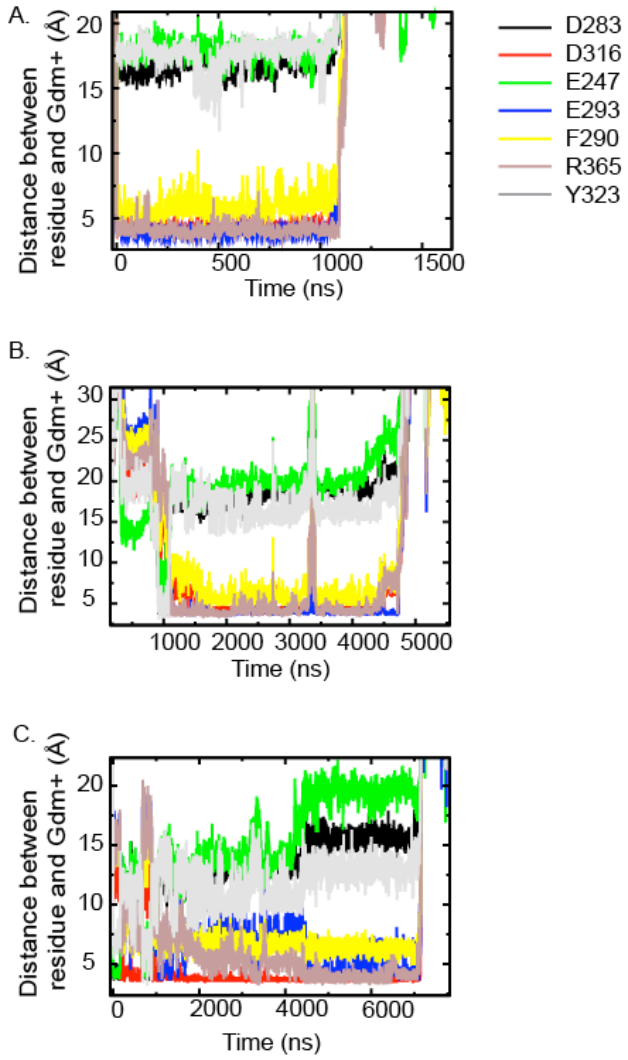

Figure S1: Time evolution of residue distances to the permeating Gdm ion, for all three permeation events observed in the applied -250mV trajectory. The overall time to permeate a Gdm ion ranges from hundreds (i.e. A vs B) to thousands of nanoseconds, the side chains involved are the same in all events, and the two-ion knock-off permeation mechanism is observed in the modified GTC binding site.

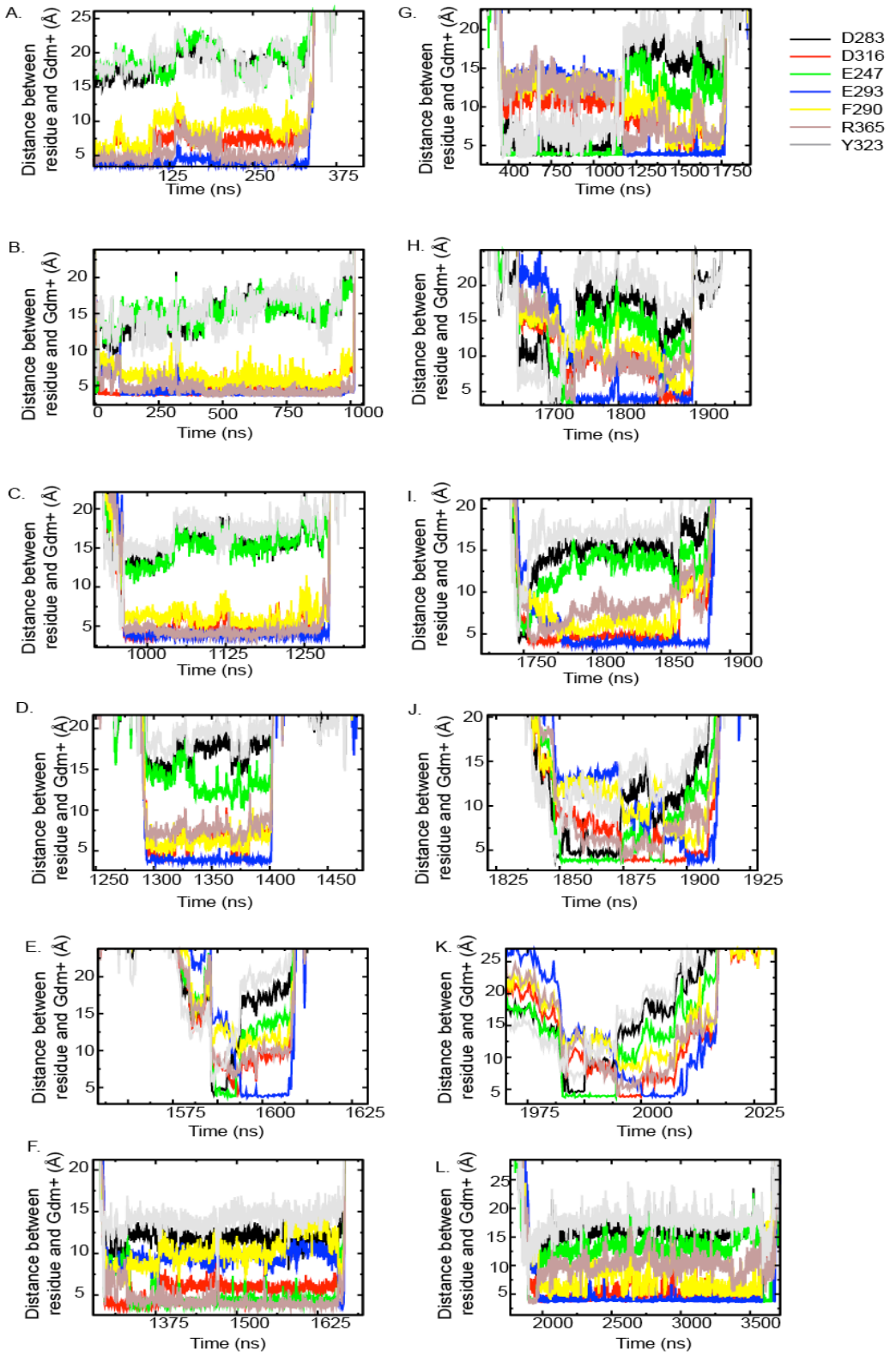

Figure S2: (A to K) Time evolution of residue distances to the permeating Gdm ion, for all 11 permeation events observed in the applied -500mV trajectory. The overall time to permeate a Gdm ion ranges from hundreds to thousands of nanoseconds, the side

chains involved are the same in all events, and the two-ion knock-off permeation mechanism is observed in the modified GTC binding site. (J) Time evolution of residue distances to the last VSD-bound Gdm, which gets lodged into the GTC and is not part of the selective permeation events.

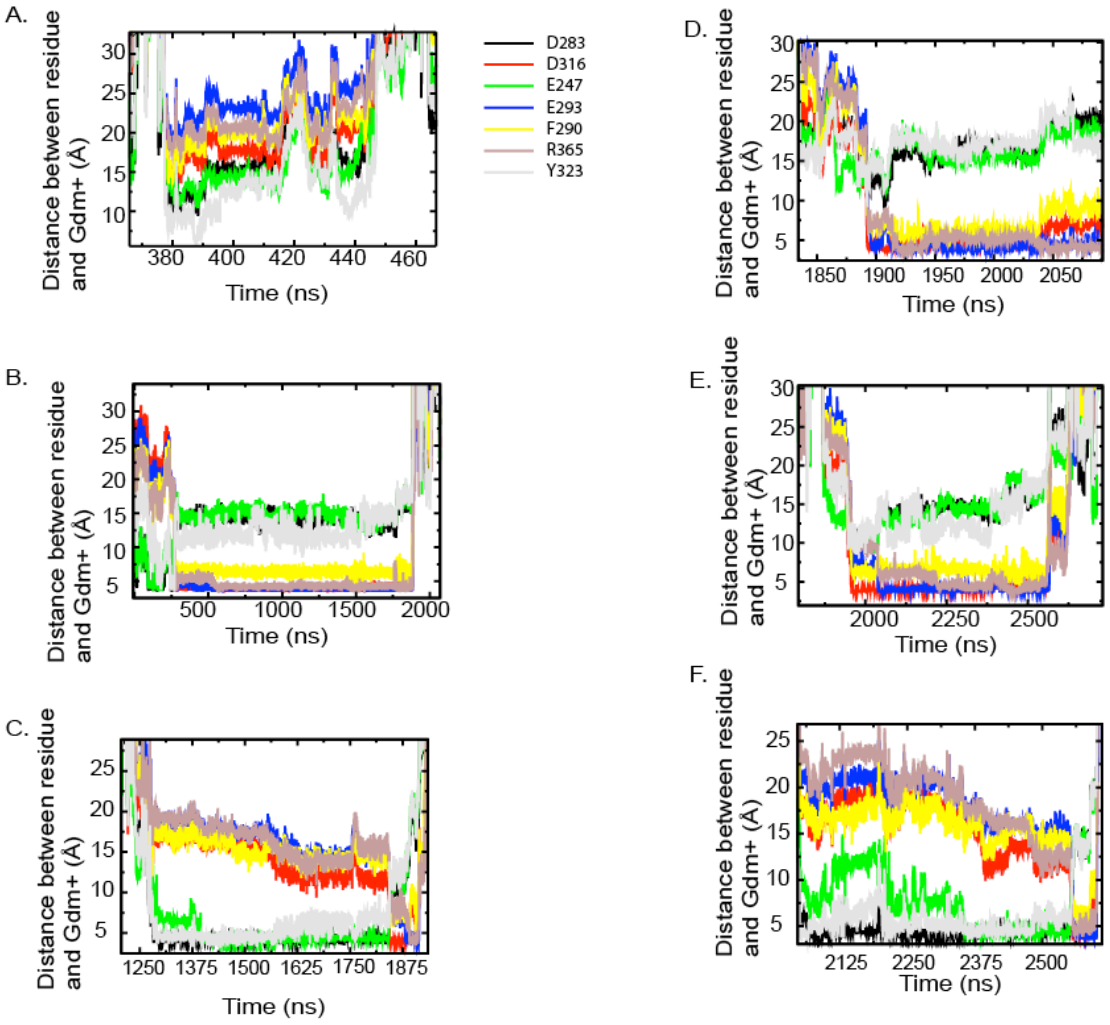

Figure S3: (A to F) Time evolution of residue distances to the permeating Gdm ion, for all 6 permeation events observed in the applied -750mV trajectory.

Chapter 5

Hv1 blockers as potential anti-neoplastic therapeutics

5.1 Introduction

Cancer is the cause of over 10% of deaths worldwide and many current treatments cause severe side effects in survivors. To improve clinical outcomes, new targets for cancer therapeutics are desirable. Towards this end, research studies in the past few decades have discovered ion channel proteins as potential new targets for cancer therapy.(1) Ion channels have long been known to play important roles in cellular excitability, however it was not until the observation that blockers of some K^+ and Ca^{2+} channels modulate proliferation in vitro that ion channels came to be examined in cancer related processes.(2) To date, ion

channels have emerged as key players in regulating malignant cell growth, and research on several anti-neoplastics targeted to ion channel function has progressed to the clinical trial stage. (3) (4, 5) (6)

Voltage-gated ion channels (VGICs) open and close in response to changes in the transmembrane (TM) potential and are associated with impulse generation and propagation in excitable cells. Studies have shown that increased VGIC expression enhances cell proliferation, migration and survival in various nonexcitable cancerous tissues, including breast, prostate, glia and colon.(7, 8) Blocking VGIC activity with small molecules can impair the growth of some cancers, both in vitro and in vivo.(3) Thus ion channels have emerged as promising antineoplastic targets, and several antineoplastics that act through VGIC blockade have progressed to the clinical trial stage, including a voltage-gated Cl^- channel blocker in Phase II trials for the treatment of gliomas.(6)

The binding sites of known small molecule VGIC blockers are being used as starting points for the rational design of antineoplastics with superior activity and minimal acute toxicity (e.g. phenytoin for treating prostate cancer).(4) The rational drug design of antineoplastics targeting VGICs requires knowledge of the channel's structure and function at a molecular level. Here we focus on a unique and newly discovered VGIC, the human voltage-gated proton channel Hv1(9, 10), as a potential target for antineoplastic therapeutics.

Hv1 only recently emerged as a potential target for breast cancer diagnostics and treatment. A clinical study of 105 breast cancer patients showed that high Hv1 expression in tumors was associated with shorter overall and recurrence-free survival. (11) In vitro

evidence suggests Hv1 aids cancer cell migration by increasing H+ extrusion, which activates acid-sensitive proteinases that degrade the extracellular matrix, allowing cancer cells to escape (i.e. metastasize). Functional blockade of Hv1 proton conductance in vivo and in vitro has been shown to inhibit cancer progression and metastasis, (11) highlighting channel blockade as a promising new avenue for cancer therapeutics. In previous studies, (11),(12) the functional blockade of Hv1 in vivo and in vitro was achieved using RNA-interference technology. Here we explore small molecule blockers of Hv1 as antineoplastic therapeutics.

5.2 Methods

To test whether Hv1 small molecule blockers may have antineoplastic properties, we employed a wound healing assay. Since migration is a prominent hallmark of tumor malignancy, the ability to inhibit migration during wound healing is indicative of the compound's anti-neoplastic therapeutic potential. The wound healing assay is performed as described. Cells are grown to confluence in 6 well tissue culture plates. Scraping the flat end of a pipette tip across the center of the plate creates a wound of standard width in each plate. Various concentrations of strong and weak Hv1 blockers were applied to the cells, including a 0mM concentration as a negative control for the buffer. The width of the wound at three locations in the plate was measured at 12hr intervals post-wound creation.

5.3 Results

5.3.1 Hv1 blockers inhibit wound healing in highly metastatic cancer cell lines

We hypothesized that high affinity Hv1 blockers, designed using insights from simulation, may inhibit antineoplastic activity when administered to cancer cells. Recent work by Wang et al. showed that Hv1 is preferentially expressed on the triple-negative (i.e. lacks Her2/neu and receptors for estrogen and progesterone), highly metastatic MB-231 breast cancer cell line.(11, 12) Their data suggest that enhanced Hv1 expression promotes invasion and metastasis in breast cancer cells by facilitating H^+ efflux, contributing to a dysregulated pH gradient (high intracellular pH and low extracellular pH) characteristic of most cancers. (13) Increased H^+ secretion aids cell survival by inhibiting acid-induced apoptosis, and the acidification of the extracellular matrix (ECM) promotes matrix remodeling and stimulates acid-activated proteases to facilitate tumor cell invasion and dissemination.(14)

Functional blockade of Hv1 using RNA-interference technology results in significant inhibition of breast cancer proliferation and migration in vivo and in vitro. (11) Our preliminary data from wound healing assays suggest blocking Hv1 with small molecules may also inhibit cell migration. Because the tumor cell's migratory activity correlates directly to its metastatic ability, the slowed rate of wound healing after treatment with blocker may be indicative of its therapeutic potential. Finding a drug that effectively inhibits a triple-negative cell line, i.e. MB-231, has considerable clinical implications, since triple-negative breast cancers have a poor prognosis and limited treatment options.(15)

Guanidinium inhibits Hv1 proton current in the mM concentration range, suggesting more complex molecules containing the guanidine moiety could have a higher binding

affinity for Hv1. Our collaborators in the Tombola lab designed guanidine derivatives with different steric features (Fig. 5.1) and tested their blocker activity on inside-out patches from Xenopus oocytes expressing the human Hv1 channel.(16)

The molecular structure of strong channel blockers (Compounds 7,12) has been identified as a guanidine moiety on a benzodiazole or benzothiazole ring and is being used as a starting point for future modifications to increase binding affinity. Using structural insights from experiments and simulation, the Tombola lab designed Compound 13, which has a modification on the benzodiazole ring of Compound 7 (GBI) and is the strongest blocker to date, with the IC50 (concentration resulting in 50% proton current inhibition) equal to 1.8μM.

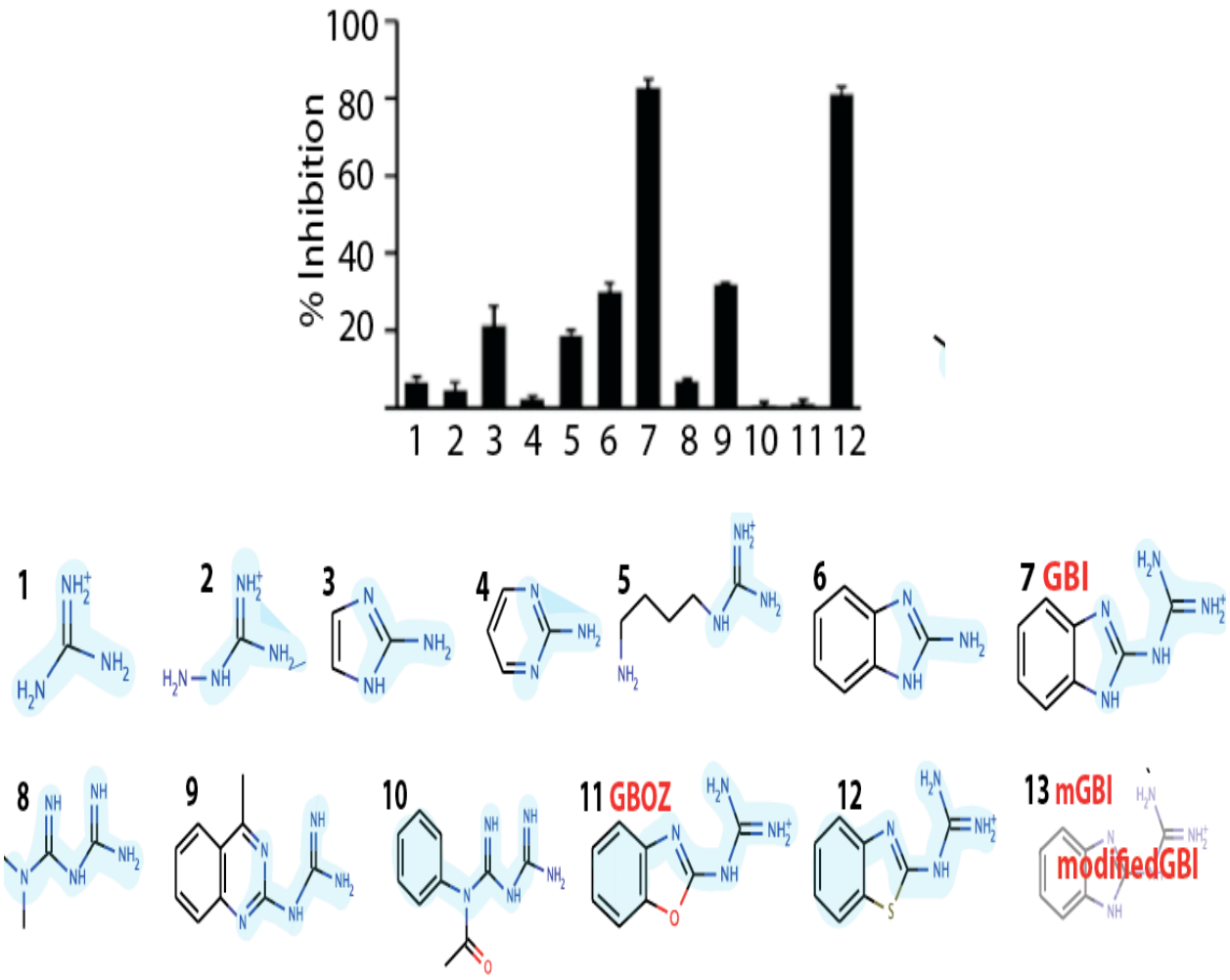

Figure 5.1. Average inhibition of Hv1 activity by guanidine derivatives. Using an inside-out patch from Xenopus oocytes expressing Hv1, proton current elicited by depolarization to +120mV was measured before and after addition of each compound to the bath solution at a final concentration of 200μM. Guanidine moieties are highlighted in blue. Parts of compound 7 that are conserved in 8-12 are also highlighted. Data from Tombola lab. (16)

The IC50 for blockers was determined by measuring proton currents in an inside-out patch from a Xenopus oocyte expressing human Hv1 before and after addition of compound in the bath solution at varying concentrations (GBI data shown Fig. 5.2). Currents were activated by depolarization to +120mV from a holding potential of -80mV. Current was measured at the end of the depolarization step (black arrow), and percent inhibition was

calculated by normalizing current in the presence of blocker to current in the absence of GBI. Percent inhibition for each concentration is plotted in Fig. 5.2, where the curve is a Hill fit of the data points. From this plot, the IC50 for GBI was determined to be 38 μM.

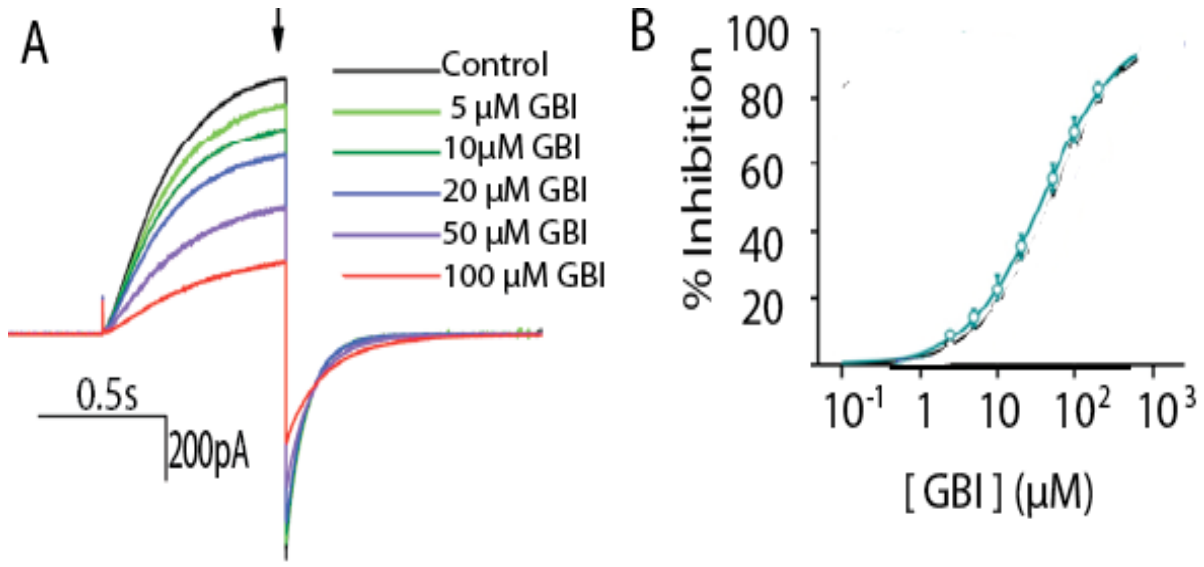

Figure 5.2. A) Proton currents measured in an inside-out patch from Xenopus oocyte expressing Hv1, before (black trace) and after (color traces) addition of GBI. Current was activated by depolarization to +120mV from a holding potential of -80mV. pHin=pHout=6.0. The current measured at the end of the depolarization step was used to produce plot shown in B. **B)** Dose dependence of GBI inhibition. Curve is a Hill fit of the data points. Data from Tombola lab(16)

Using reverse transcription PCR on total cell RNA extracts from our collaborator Dr. Phang-Lang Chen, I surveyed Hv1 mRNA expression in a panel of breast cancer cell lines (Fig. 5.3). I found expression patterns consistent with Wang et al. data, and identified an additional breast cancer cell line (MB-361) with Hv1 expression. (11)

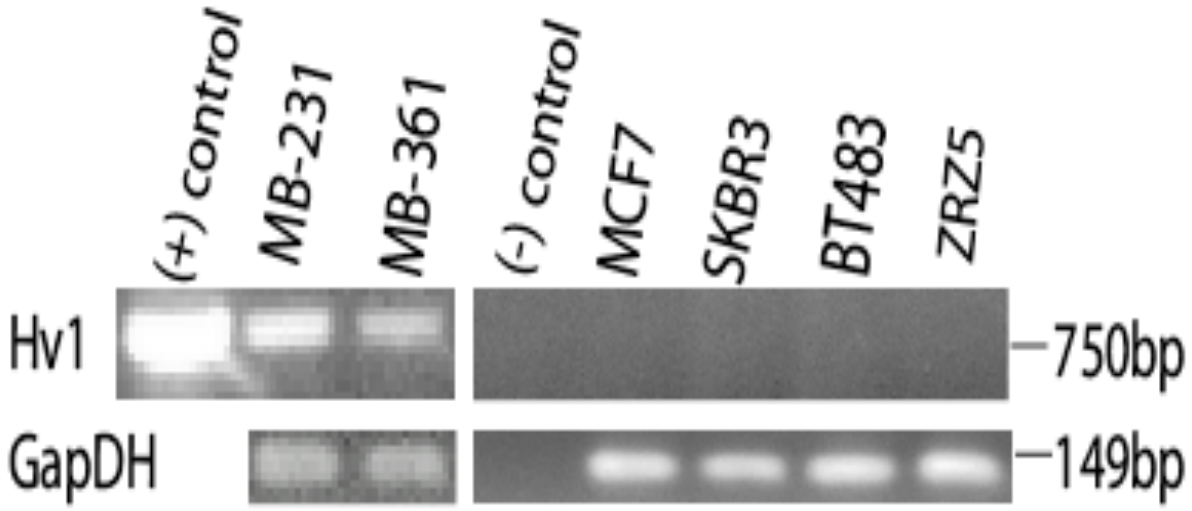

Figure 5.3. Hv1 mRNA expression in breast cancer cell lines detected by RT-PCR

In the MB-231 cell line, we tested three Hv1 blockers, Compounds 11, 7 and 13 (termed GBOZ, GBI and mGBI) for ability to inhibit cell migration using the wounded monolayer assay (Fig. 5.4). Briefly, MB-231 cells were seeded in six-well plates and grown to confluence. The cell monolayer was mechanically wounded with a 200μl pipette tip and washed three times to remove detached cells. Following injury, cells were maintained in media with varying concentrations of drug (50, 100 or 200 μM blocker in 10% DMSO) or drug-vehicle control (DMSO). Cells then migrated to close the wound. This movement was observed using an inverted bright field microscope, and images were captured with a digital camera at 0, 14 and 26 hours post-wounding. Wound distance at each time point was determined by measuring the distance between the confluent edges of cells using NIS-Elements software. Fraction wound remaining was calculated as wound distance at the specified time point divided by initial wound distance. As expected, the weakest blocker, GBOZ, had no effect on migration, and the strongest blocker, mGBI, slowed wound healing dose-dependently, suggesting Hv1 blockers may have anti-metastatic activity.

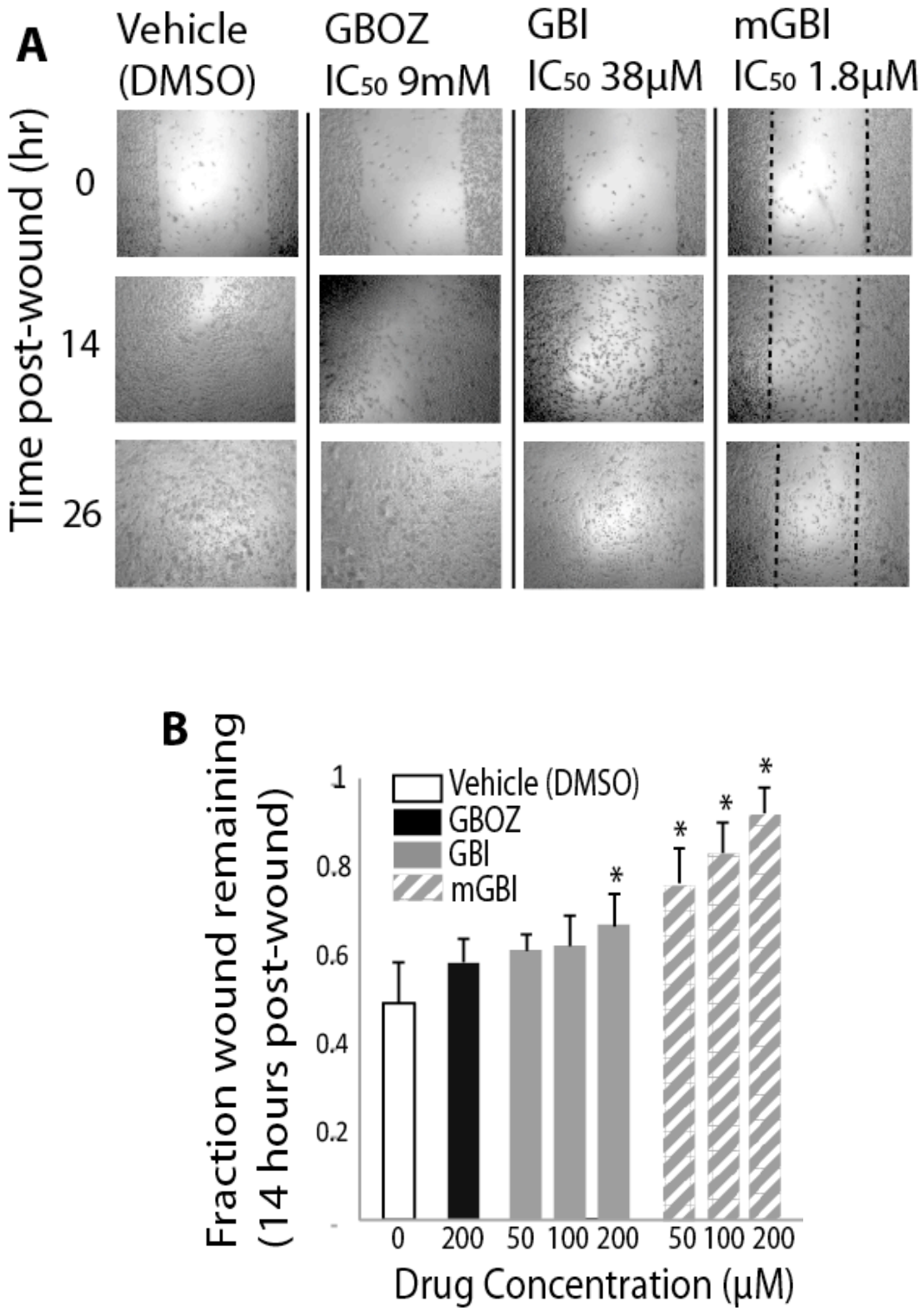

Figure 5.4. Hv1 blockers decrease cell migration A) Images of wound healing in MB-231 cells treated with blocker (200 μM in 10% DMSO) or without blocker (DMSO) for 0, 14 or 26hr post-wound infliction. B) Wound healing is significantly inhibited by treatment with

mGBI at 50,100 and 200μM and with GBI at 200μM. Fraction wound remaining is calculated using the equation: [wound area at $T_{14\ hours}$/wound area at T_0)], where T_{14} is the 14 hr time point and T_0 is the time immediately after wounding. Values are mean + SD (n=3), *P<0.05, versus vehicle control, unpaired t-test.

5.4 Concluding remarks

Detailed atomistic structure/function data will continue to address questions about how Hv1 is able to sense voltage and conduct protons, which will help to establish basic principles of ion conduction through VSDs. Insight into these principles may guide the design of high affinity Hv1 blockers, which should be evaluated for their potential use in cancer treatment. Based on our preliminary data presented in this chapter, it appears Hv1 blockade may be a a viable mechanism for breast cancer cell inhibition.

5.5 References

1. Kunzelmann K (2005) Ion channels and cancer. *J Membr Biol* 205(3):159-173.
2. Prevarskaya N, Skryma R, & Shuba Y (Ion channels and the hallmarks of cancer. *Trends Mol Med* 16(3):107-121.
3. Arcangeli A*, et al.* (2009) Targeting ion channels in cancer: a novel frontier in antineoplastic therapy. *Curr Med Chem* 16(1):66-93.
4. Sikes RA*, et al.* (2003) Therapeutic approaches targeting prostate cancer progression using novel voltage-gated ion channel blockers. *Clin Prostate Cancer* 2(3):181-187.
5. Anderson JD*, et al.* (2003) Voltage-gated sodium channel blockers as cytostatic inhibitors of the androgen-independent prostate cancer cell line PC-3. *Mol Cancer Ther* 2(11):1149-1154.
6. Mamelak AN*, et al.* (2006) Phase I single-dose study of intracavitary-administered iodine-131-TM-601 in adults with recurrent high-grade glioma. *J Clin Oncol* 24(22):3644-3650.
7. Arcangeli A (Ion channels and transporters in cancer. 3. Ion channels in the tumor cell-microenvironment cross talk. *Am J Physiol Cell Physiol* 301(4):C762-771.
8. Fiske JL, Fomin VP, Brown ML, Duncan RL, & Sikes RA (2006) Voltage-sensitive ion channels and cancer. *Cancer Metastasis Rev* 25(3):493-500.
9. Sasaki M, Takagi M, & Okamura Y (2006) A voltage-sensor domain protein is a voltage-gated proton channel. *Science* 312:589-592.

10. Ramsey IS, Moran MM, Chong JA, & Clapham DE (2006) A voltage-gated proton-selective channel lacking the pore domain. *Nature* 440:1213-1216.

11. Wang Y, Li SJ, Wu X, Che Y, & Li Q (Clinicopathological and biological significance of human voltage-gated proton channel Hv1 protein overexpression in breast cancer. *J Biol Chem* 287(17):13877-13888.

12. Wang Y*, et al.* (Specific expression of the human voltage-gated proton channel Hv1 in highly metastatic breast cancer cells, promotes tumor progression and metastasis. *Biochem Biophys Res Commun* 412(2):353-359.

13. Webb BA, Chimenti M, Jacobson MP, & Barber DL (2011) Dysregulated pH: a perfect storm for cancer progression. *Nature Reviews Cancer* 11(9):671-677.

14. Giannelli G & Antonaci S (2002) Gelatinases and their inhibitors in tumor metastasis: from biological research to medical applications. *Histol Histopathol* 17(1):339-345.

15. Bae SY*, et al.* (The prognoses of metaplastic breast cancer patients compared to those of triple-negative breast cancer patients. *Breast Cancer Res Treat* 126(2):471-478.

16. Hong L, Pathak, M., Kim, I.H., Ta, D., Tombola, F. (In press) Voltage-sensing domain block in the Hv1 channel. *Neuron*.

Chapter 6

Concluding Remarks

The work presented in this dissertation focused primarily on uncovering the molecular mechanisms governing the basic properties of voltage-sensing domains. Molecular dynamics simulations allowed us to hypothesize a mechanism for proton conduction in the Hv1 channel described in Chapter 2, propose an open-state structure described in Chapter 3 and propose binding sites for channel blockers as described in Chapter 5. I tested the antineoplastic activity of a set of Hv1 channel blockers using two-dimensional wound assays, which measure the ability of cancer cells to migrate across the tissue culture plane. I found a dose-dependent decrease in wound healing ability in cancer cells treated with Hv1 inhibitors, suggesting that channel blockade may represent a viable new approach to inhibiting cancer cell growth. Essential to the development of clinically useful antineoplastic therapeutics is the formulation of compounds with a high specificity and selectivity for the channel, since these properties are related to off-target unwanted side effects. To design compounds that target Hv1, a better understanding of how the blockers may enter the

channel and where the blockers may finally bind is needed. Towards this end, I developed force-field parameters for modeling the Hv1 channel blocker, GBI. Simulations of GBI in complex with the open-state configuration of Hv1 described in Chapter 3 will attempt to shed light on the drug binding pathway while sampling potential docking sites.

Data from the classical MD simulations described in Chapter 2 and 3 support Grotthuss hopping indirectly; to test its feasibility directly, proton transfer (PT) along a water wire in Hv1 must be simulated. The transfer of a proton from one water molecule to another involves breaking an O-H bond in the proton-donor water molecule and forming an O-H bond proton-acceptor water molecule. This bond breaking and forming is a quantum mechanical process, so to simulate PT, software such as CP2K may be used to perform a QM/MM (Quantum Mechanics/Molecular Mechanics) simulation in which the water wire and selected ionizable side chains comprise the region treated quantum mechanically. The QM region is surrounded by the MM region (protein, membrane and bulk water) containing explicitly represented atoms that are described by a classical force field.

The free energy profile, or potential of mean force (PMF), for PT across Hv1 could be calculated using umbrella sampling,(1) which involves a series of biased simulations where the reaction coordinate is kept near a desired value by imposing a harmonic restraint. This technique ensures adequate sampling of the entire reaction coordinate (e.g. the ion conduction path along the pore interior axis). Biased simulations of PT in Hv1 necessitate implementation of a novel CP2K reaction coordinate for H+ translocation along a QM water wire based on the 'center of excess charge' coordinate,(2) which corresponds roughly to the proton location. The PMF may be constructed from these biased simulations by using the weighted histogram analysis method (WHAM).(3) By correlating minima and barriers in the

PMF profile to structure features in the open model of Hv1, one may gain insight into molecular mechanisms underlying proton conduction. We expect energetic minima to correspond to areas in Hv1 where the H^+ has favorable electrostatic interactions with charged residues or where the water wire is particularly stable. Additionally, If Grotthuss hopping is a feasible mechanism of proton transfer in Hv1, we expect low barriers (<5kcal/mol) in the PMF for proton conduction through the channel.

Using the equation for maximum ion conductance assuming quasi one-dimensional ion transport, maximum proton conductance for our model may be computed. The formula exponentially depends on the free energy profile (i.e. PMF) and is linearly proportional to the reaction coordinate-dependent diffusion coefficient, which can be calculated according to Hummer's simplified Woolf-Roux equation.(4, 5) We expect that the calculated maximum conductance would agree with experimental measurements, thereby supporting the validity of the model.

The implementation of a novel reaction coordinate for biased QM/MM simulation requires a series of benchmark calculations. The first step would be to develop the center of excess charge coordinate for a simple system; i.e. a single-file QM water wire treated in vacuum. Biased simulations of H+ transfer along the simple water wire would be an appropriate initial control to verify correct implementation of the CEC coordinate and should yield a PMF which is relatively flat at the center. Once the expected PMF for this simple system is produced, the logical next step is to implement the reaction coordinate into the more complex system of Hv1 embedded in membrane.

Ultimately, many questions still remain regarding the open state of the Hv1 channel and the pathway taken by the permeating proton. Answers to questions about the fundamental properties of the proton channel may be partially informed by our simulations of the structurally similar omega pore. The pathway taken by the permeating Gdm ion in the omega pore likely overlaps with the basic residues on the S4 helix. These are the same residues which are thought to overlap with the proton permeation pathway in Hv1. Accordingly, the two-ion knock-off mechanism observed during Gdm permeation in the omega pore is similar to the movement of the S4 helix observed in Hv1, where two arginine side groups travel together under the influence of an electric field before the third one clicks into place. The omega pore simulations also dovetail with the current set of small molecule Hv1 channel blockers developed out of the Tombola lab, which all contain a guanidinium moiety. Thus, the binding pathway and binding sites observed during the Gdm permeation event through the omega pore may be similar to those taken/occupied by the Hv1 channel blockers. Taken together, the simulations of these two ion-conducting VSDs provide a foundation for designing small molecule channel modulators, which may have applications in the treatment of stroke, cancer and diabetes.

References

1. Torrie GM & Valleau JP (1977) Nonphysical sampling distributions in Monte Carlo free-energy estimation: Umbrella sampling. *J. Comput. Phys.* 23:187-199.
2. König PH*, et al.* (2006) Toward theoretical analysis of long-range proton transfer kinetics in biomolecular pumps. *J. Phys. Chem. A* 110:548-563.
3. Kumar S, Bouzida D, Swendsen RH, Kollman PA, & Rosenberg JM (1992) The weighted histogram analysis method for free-energy calculations on biomolecules. I. The method. *J. Comput. Chem.* 13:1011-1021.
4. Roux B & Karplus M (1991) Ion-Transport in a Gramicidin-Like Channel - Dynamics and Mobility. *J. Phys. Chem.* 95(12):4856-4868.
5. Hummer G (2005) Position-dependent diffusion coefficients and free energies from Bayesian analysis of equilibrium and replica molecular dynamics simulations. *New J. Phys.* 7:34.

Appendix

Parameters for GBI

The CHARMM parameters developed for the Hv1 blocker 2-guanidinium-benzimidazole (2-GBI) are presented here. These parameters were developed using the CHARMM General Force Field program, as described by Vanommeslaeghe et al(1, 2). Further details regarding the workflow used for GBI and other sample molecules may be found in the directory /export/local/mwood/cgf on djtraid3.

```
* Toppar stream file generated by
* CHARMM General Force Field (CGenFF) program version 0.9.3 beta
* For use with CGenFF version 2b6
*

read rtf card append
* Topologies generated by
* CHARMM General Force Field (CGenFF) program version 0.9.3 beta
*
36 1

! "penalty" is the highest penalty score of the associated parameters.
! Penalties lower than 10 indicate the analogy is fair; penalties between 10
! and 50 mean some basic validation is recommended; penalties higher than
```

```
! 50 indicate poor analogy and mandate extensive validation/optimization.

RESI gbi1           1.000 ! param penalty= 278.000 ; charge penalty= 184.588
GROUP           ! CHARGE   CH_PENALTY
ATOM N      NG2P1  -0.61 !    2.500
ATOM C      CG2N1   0.69 !   32.749
ATOM N1     NG2P1  -0.63 !    2.500
ATOM H      HGP2    0.35 !    0.000
ATOM H1     HGP2    0.34 !    0.000
ATOM N2     NG2P1  -0.28 !  184.588
ATOM C1     CG2R53  0.69 !  183.239
ATOM N3     NG2R50 -0.85 !   25.611
ATOM C2     CG2RC0  0.44 !    2.500
ATOM C3     CG2R61 -0.36 !    0.000
ATOM C4     CG2R61 -0.23 !    0.000
ATOM C5     CG2R61 -0.19 !    0.000
ATOM C6     CG2R61 -0.32 !    0.000
ATOM C7     CG2RC0  0.17 !   13.577
ATOM N4     NG2R51 -0.34 !   25.969
ATOM H2     HGP1    0.29 !   12.996
ATOM H3     HGP2    0.42 !    0.000
ATOM H4     HGP2    0.34 !    0.000
ATOM H5     HGP2    0.26 !   20.716
ATOM H6     HGR61   0.25 !    0.000
ATOM H7     HGR61   0.19 !    0.000
ATOM H8     HGR61   0.19 !    0.000
ATOM H9     HGR61   0.19 !    0.000

BOND H3   N
BOND N    C
BOND N    H4
BOND H6   C3
BOND H7   C4
BOND C3   C4
BOND C3   C2
BOND C4   C5
BOND N3   C2
BOND N3   C1
BOND C    N2
BOND C    N1
BOND C2   C7
BOND H    N1
BOND C5   H8
BOND C5   C6
BOND C1   N2
BOND C1   N4
```

```
BOND N2   H5
BOND C7   C6
BOND C7   N4
BOND N1   H1
BOND C6   H9
BOND N4   H2
IMPR C      N      N2     N1
IMPR C1     N2     N3     N4

END


read param card flex append
* Parameters generated by analogy by
* CHARMM General Force Field (CGenFF) program version 0.9.3 beta
*

! Penalties lower than 10 indicate the analogy is fair; penalties between 10
! and 50 mean some basic validation is recommended; penalties higher than
! 50 indicate poor analogy and mandate extensive validation/optimization.

BONDS
CG2R53 NG2P1   463.00     1.3650 ! gbi , from CG2N1 NG2P1, penalty= 170

ANGLES
NG2P1  CG2R53 NG2R50   65.00    125.00 ! gbi , from NG2R53 CG2R53 OG2D1,
penalty= 47
NG2P1  CG2R53 NG2R51   70.00    122.00 ! gbi , from NG2R51 CG2R53 OG2D1,
penalty= 28
CG2N1  NG2P1  CG2R53   62.30    120.00 ! gbi , from CG2N1 NG2P1 CG324,
penalty= 74
CG2R53 NG2P1  HGP2     49.00    120.00 ! gbi , from CG2N1 NG2P1 HGP2, penalty=
33

DIHEDRALS


NG2P1  CG2N1  NG2P1  CG2R53     2.2500  2   180.00 ! gbi , from NG2P1 CG2N1
NG2P1 CG324, penalty= 74
NG2R50 CG2R53 NG2P1  CG2N1      1.2000  2   180.00 ! gbi , from CG2R61 CG2R61
NG2S1 CG2O1, penalty= 276
NG2R50 CG2R53 NG2P1  HGP2       2.2500  2   180.00 ! gbi , from NG2P1 CG2N1
NG2P1 HGP2, penalty= 238
!CG2N1    NG2P1   CG2R53   NG2R51     0.00  1    180.0
!CG2N1    NG2P1   CG2R53   NG2R51     0.02  2      0.0
CG2N1    NG2P1   CG2R53   NG2R51     2.69  1    180.0
```

```
CG2N1    NG2P1   CG2R53   NG2R51     1.90  2      0.0
CG2N1    NG2P1   CG2R53   NG2R51     0.34  3    180.0
CG2N1    NG2P1   CG2R53   NG2R51     0.26  4    180.0
CG2N1    NG2P1   CG2R53   NG2R51     0.35  6      0.0
!NG2R51 CG2R53 NG2P1  CG2N1      0.0000  1     0.00 ! gbi , from CG2R61 CG2R61
NG2S1 CG2O1, penalty= 278
NG2R51 CG2R53 NG2P1  HGP2       2.2500  2   180.00 ! gbi , from NG2P1 CG2N1
NG2P1 HGP2, penalty= 236
NG2P1  CG2R53 NG2R50 CG2RC0    13.0000  2   180.00 ! gbi , from CG3C52
CG2R52 NG2R50 CG2RC0, penalty= 65
NG2P1  CG2R53 NG2R51 CG2RC0     2.5000  2   180.00 ! gbi , from OG2D1 CG2R53
NG2R51 CG2RC0, penalty= 28
NG2P1  CG2R53 NG2R51 HGP1       0.8600  2   180.00 ! gbi , from OG2D1 CG2R53
NG2R51 HGP1, penalty= 28

IMPROPERS
CG2R53 NG2P1  NG2R50 NG2R51    40.0000  0     0.00 ! gbi , from CG2R53 CG2DC1
NG2R51 OG2D1, penalty= 143

RING planar 6 C2 C3 C4 C5 C6 C7
RING planar 5 C1 N3 C2 C7 N4
END
```

References

1. Vanommeslaeghe K & MacKerell AD, Jr. (2012) Automation of the CHARMM General Force Field (CGenFF) I: bond perception and atom typing. *J Chem Inf Model* 52(12):3144-3154.
2. Vanommeslaeghe K, Raman EP, & MacKerell AD, Jr. (2012) Automation of the CHARMM General Force Field (CGenFF) II: assignment of bonded parameters and partial atomic charges. *J Chem Inf Model* 52(12):3155-3168.